Journal of Materials Chemistry A

REVIEW

View Article Online
View Journal | View Issue

Cite this: J. Mater. Chem. A, 2024, 12, 24005

Exploring the synergy of magnetism and electrocatalysis: a comprehensive review on mechanisms, recent developments and future perspectives

Mohammed Arkham Belgami,[a] Abhinandan Patra,[a] Sang Mun Jeong *[b] and Chandra Sekhar Rout *[ab]

The development of sustainable techniques for electrocatalysis significantly depends on the creation of more efficient, cost-effective and reliable electrocatalysts that can overcome the sluggish kinetics of the process and thereby accelerate the overall energy conversion. External stimuli such as magnetic field have been known to have an impact on material properties, presenting a promising route to enhance electrocatalytic processes, including the hydrogen evolution reaction (HER), oxygen evolution reaction (OER), oxygen reduction reaction (ORR) and carbon dioxide reduction reaction (CO_2RR). Recent studies have strongly supported the beneficial effects of magnetic field on the fabrication of electrocatalysts and electrocatalytic reactions. However, there is still noticeable lack of interest and enthusiasm among the research community in this interdisciplinary field. Thus, this review aims to emphasize the importance of the combined effect of magnetic field and energy production. Initially, we present a thorough explanation of the fundamental mechanisms of the aforementioned electrocatalytic processes and then vividly elaborate the potential mechanisms underlying magnetic field-enhanced electrocatalysis. Finally, we highlight the recent advancements in this field, followed by the associated comprehensive current challenges and future perspectives.

Received 10th April 2024
Accepted 5th August 2024

DOI: 10.1039/d4ta02468k

rsc.li/materials-a

[a]Centre for Nano and Material Sciences, Jain (Deemed-to-be University), Jain Global Campus, Kanakapura Road, Bangalore 562112, Karnataka, India. E-mail: r.chandrasekhar@jainuniversity.ac.in; csrout@gmail.com

[b]Department of Chemical Engineering, Chungbuk National University, Cheongju, Chungbuk 28644, Republic of Korea. E-mail: smjeong@chungbuk.ac.kr

Mohammed Arkham Belgami

Mohammed Arkham Belgami completed his bachelor's degree from Veerashaiva College, affiliated to Vijayanagara Sri Krishnadevaraya University, Bellary, Karnataka, India (2018). Later, he moved to Mysore University, Karnataka, India, to pursue his master's in Chemistry (2018–20). Currently, he is a doctoral student of Chemistry at the CNMS, Jain University, working under Prof. Chandra Sekhar Rout, with his research focused on the energy and environmental applications of 2D nanomaterials.

Abhinandan Patra

Abhinandan Patra was born and brought up in Puri, the spiritual capital of Odisha, India, where he finished his education upto M.Sc. in Physics. He was awarded with a PhD degree in Physics from CNMS, Jain University, Bangalore, India. During the tenure of his PhD, he was awarded a prestigious fellowship from the Ministry of Foreign Affairs and International Cooperation (MAECI) under the Italian government. Lately, he has been working on the integration of solar cell with supercapacitor for photosupercapacitor application at CHOSE, University of Rome Tor Vergata, Rome, Italy as a post doc fellow.

1. Introduction

Due to overwhelming consumption and depletion of fossil fuel, problems related to environmental pollution and the resulting energy crisis have become significant stumbling blocks in society.[1,2] Despite the temporary decline in carbon dioxide emissions triggered by the COVID-19 pandemic, the global trajectory points towards a temperature increase surpassing 3 °C in this century.[3] CO_2 emissions from various anthropogenic activities have devastating effects, making it beyond the reach to limit global warming to 1.5 °C above pre-industrial levels.[4] Thus, the current situation immensely necessitates the need to develop renewable energy sources. The increasing interest among the researchers for the adoption of sustainable energy in recent times have proven to be an effective strategy towards achieving carbon neutrality and a sustainable future.[5,6] The use of renewable energy sources such as solar, hydroelectric, wind, and geothermal can be alternatives to fossil fuels, which can also contribute to reducing the CO_2 levels in the atmosphere and thereby help mitigate the drawbacks of climate change. Besides the conventional energy sources, other advanced techniques are available for sustainable development, including electrochemistry, not only in energy storage but also in energy conversion technology.[7,8] The current carbon capture technologies employ electrochemistry to capture and utilize CO_2.[9] Similarly, electrochemistry has paved the way for the production of valuable chemicals and materials, providing a sustainable and environmentally friendly alternative to traditional, resource-intensive chemical synthesis methods.[10,11] It also plays a major role in the production of clean energy, such as electrochemical reactions, including the oxygen reduction reaction (ORR), hydrogen evolution reaction (HER), oxygen evolution reaction (OER) and, carbon dioxide reduction reaction (CO_2RR).[12–15] For these processes to progress positively, the development of efficient and cost effective electrocatalysts is crucial to actualize high electrochemical performance in sustainable energy applications. Strategies such as increasing the number of active sites on the surface of electrodes and enhancing their intrinsic activity are vital for optimizing their performance.[16–18] There are many published reports wherein the researchers have extensively modified the external features of materials through morphological modification,[19,20] defect engineering,[21,22] doping,[23,24] phase transitions,[25,26] crystal engineering,[27,28] and composite preparation.[29] However, despite these efforts, enhancing the activity of materials has reached a bottleneck. In this case, the application of an external field such as electric field, strain, ultrasonic field, light field and magnetic field[30–34] offers an alternative avenue for further enhancing the electrocatalytic activities of materials, facilitating charge transfer and reducing the reaction kinetic barriers in a seamless manner (Fig. 1).

For instance, Xu *et al.*[35] synthesized Au–MnO_2 hybrid crystals and used a laser intensity in the range of 100 to 200 mV to enhance their OER activity, resulting in a reduction in the overpotential value from 0.38 to 0.32 V. Wang *et al.*[36] studied the influence of a super gravity field on electrolysis, which was performed using a constant current (galvanostatic) method. Similarly, Wang *et al.*[37] synthesized MoS_2 nanosheet-based electrocatalysts for HER. By tuning the external electric field, they achieved a minimal overpotential of 38 mV at a current density of 100 mA μm^{-2}. On the contrary, the magnetic field has been an underrated phenomenon, which has been proven to be a novel strategy to enhance the activity of materials towards energy applications.[38] Predominantly, a magnetic field works by inducing changes in the spin configurations of magnetic materials, enhancing the mass transfer on the electrode surface and offering a precise control of the orientation and alignment of catalysts. The relationship between a magnetic field and electrocatalytic systems involves various effects such as Kelvin force,[39] magnetic hyperthermia,[40] Maxwell stress, spin selectivity, and magnetohydrodynamic effect.[41,42] This emerging field enhances our understanding of electrochemical principles and offers opportunities for innovative technologies and future advancements. To date,

Sang Mun Jeong

Sang Mun Jeong is Professor in the Department of Chemical Engineering at Chungbuk National University, South Korea, Leader of the Regional Leading Research Center (RLRC) for developing next-generation battery materials funded by National Research Foundation of Korea, and Director of Korea Institute of Chemical Engineers. Moreover, he has been Dean of Research Affairs of Chungbuk National University (2021–2023). His research focuses on energy-related materials and processes based on chemical and electrochemical engineering to develop efficient, clean and renewable future energy.

Chandra Sekhar Rout

Prof. Chandra Sekhar Rout is Full Professor at the CNMS, Jain University. Before joining the CNMS, he was a DST-Ramanujan Fellow at IIT Bhubaneswar, India (2013–2017). He obtained his PhD from JNCASR, Bangalore (2008), followed by postdoctoral research at NUS, Purdue University, and UNIST. His research is focused on applications of 2D layered materials for different devices. He has authored more than 200 research papers and 7 books. His h-index is 59, with total citations of >15 000. The Stanford study ranked him in the top 2% of scientists in 2020–2023.

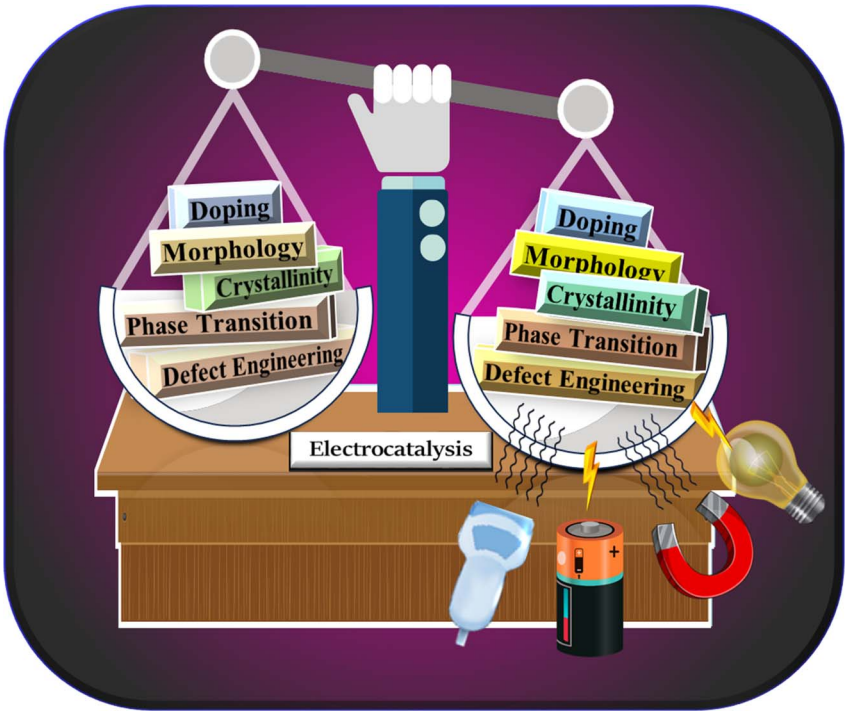

Fig. 1 Schematic depiction of the additional effect of an external template on conventional modifications.

previous reviews have been reported on this topic, which separately focus on the mechanisms of magneto-electrochemistry, theoretical insights into the spin configurations of electrocatalysts, fabrication of electrocatalysts in the presence of a magnetic field, engineering spin configurations using a magnetic field, and effects of various external templates to promote water splitting.[43–49]

Alternatively, this review presents a comprehensive view of the key aspects of electrochemistry. Initially, we present a concise introduction on electrocatalysis, focusing on the fundamentals of magnetoelectrochemistry and providing a foundational understanding of the interplay between a magnetic field and electrochemical processes. Subsequently, we focus on the magnetic field-induced fabrication of electrocatalysts, shedding light on innovative methodologies that leverage a magnetic field in the design of catalysts. In the next section, we thoroughly summarise the recent advances in magnetic field-enhanced electrocatalysis, elucidating the various effects of a magnetic field that contribute to improved electrochemical performances. Finally, this journey is not completed without challenges, as discussed in the last section, where the obstacles and potential roadblocks are addressed together with a glimpse into future perspectives.

2. Overview on electrocatalysis

Electrocatalysis is one of the most important renewable technologies for finding sustainable energy sources. Together with ORR and CO_2RR, the mechanism of the HER and OER is essential for energy conversion applications. Electrochemical water splitting, which is considered a desirable, efficient, and carbon-neutral method, produces hydrogen (H_2) and oxygen (O_2) from water ($2H_2O \rightarrow 2H_2 + O_2$, $\Delta G = -237$ kJ mol^{-1}).[50,51] Remarkably, this method may achieve a conversion efficiency of up to 80%. Subsequently, the resultant hydrogen is transformed into a powerful energy source for high-performance fuel cells, which have an astounding 60% conversion efficiency. Likewise, the CO_2RR, which plays a vital role in the sustainable chemical production of carbon-based products, including methane, ethylene, methanol, and formic acid, and the ORR, a critical reaction in fuel cells, are crucial in the efficient generation of electricity from hydrogen and other fuels in fuel cells and metal–air batteries. Overall, these technologies play a vital role in advancing sustainable energy technologies and reducing the environmental impact.

Additionally, the cooperation of fuel cells, which produce energy from H_2 and O_2, and electrolytic cells, which produce H_2 and O_2, results in an integrated energy cycle, which represents a sustainable water-based energy source. The production of H_2 and O_2 by the electrolytic cell and the consumption of these gases by the fuel cell to produce electricity constitute the perfect water cycle. Fig. 2a and b depict the four half-cell reactions and their respective polarization curves.[52,53]

Electrochemical water splitting has attracted significant attention from researchers in the last few decades. Ir- and Ru-based oxides have attracted interest due to their ability to catalyze the OER, and the valuable Pt-based materials have emerged as the best candidates for the effective electrocatalysis of the HER.[54,55] However, the scarcity and high cost of the latter limit their large-scale and industrial use. Therefore, research is focused on developing advanced, precious metal-free electrocatalysts that are stable and highly active for water splitting.

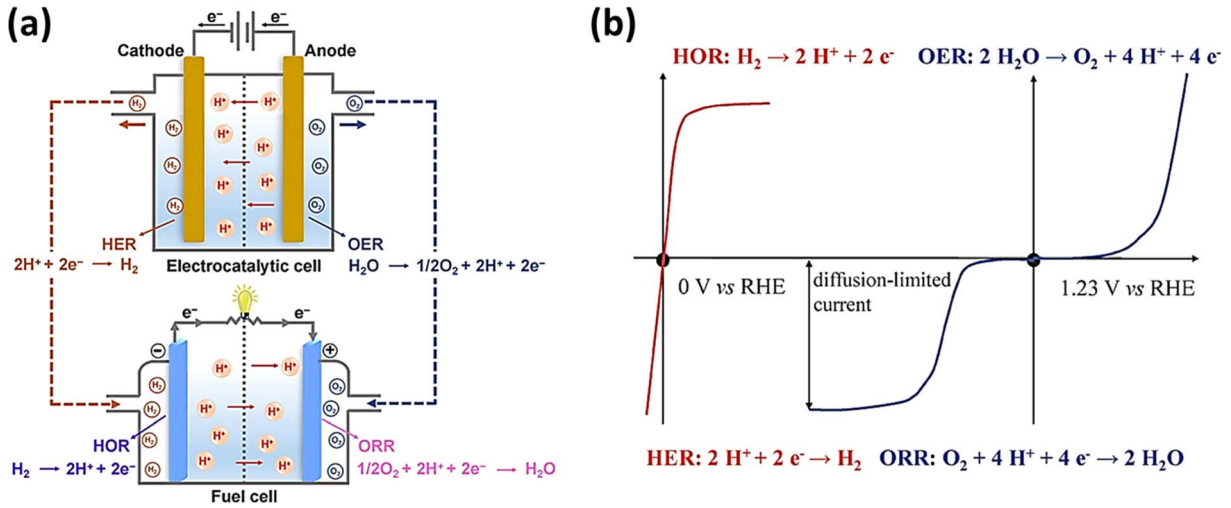

Fig. 2 (a) Depiction of the four half-cell reactions (reprinted with permission,[52] copyright 2022, Elsevier) and (b) polarization curves of the four reactions occurring at electrolytic and fuel cells (reprinted with permission,[53] copyright 2015, the Royal Society of Chemistry).

These developments in high-performing electrocatalysts are encouraging given that they represent significant progress in supporting the expansion of the hydrogen economy.

2.1. General concepts of electrocatalysis

2.1.1. HER. From a mechanistic standpoint, the electrochemical HER reduces protons under acidic conditions or water molecules under alkaline conditions to produce hydrogen molecules (H_2). Fig. 3a illustrates the three basic phases of the HER process. The reaction takes place on the electrode surface with a very low external voltage.[57] Primarily, this process begins with the Volmer reaction (eqn (1) and (2)), which is a proton–electron interaction, resulting in the adsorption of a hydrogen atom (H) on the electrode material (M). The proton sources differ depending on the electrolyte, which include water molecules under alkaline conditions and the hydronium cation (H_3O^+) in acidic media. The Volmer reaction is followed by the Heyrovsky reaction (eqn (3) and (4)), the Tafel reaction (eqn (5)), or their combination, leading to the formation of H_2. In the Heyrovsky step, H_2 is produced by the reaction with a second electron after a second proton diffuses to the adsorbed H. Alternatively, two nearby H entities on the electrode surface merge in the Tafel step to produce H_2.[51,58] This complex sequence of electrochemical reactions highlights the complex path from proton reduction to the production of hydrogen molecules, highlighting the various stages and reactions associated with this vital electrocatalysis process. The overall process can be written as follows:[59]

(1) Volmer step:

$$H_3O^+ + M + e^- \rightleftharpoons M\text{–}H_{ads} \text{ (acidic medium)} \quad (1)$$

$$M + H_2O + e^- \rightleftharpoons M\text{–}H_{ads} + OH^- \text{ (alkaline medium)} \quad (2)$$

(2) Heyrovsky step:

$$M\text{–}H_{ads} + H^+ + e^- \rightleftharpoons M + H_2 \text{ (acidic medium)} \quad (3)$$

$$M\text{–}H_{ads} + H_2O + e^- \rightleftharpoons M + OH^- + H_2 \text{ (alkaline medium)} \quad (4)$$

(3) Tafel step:

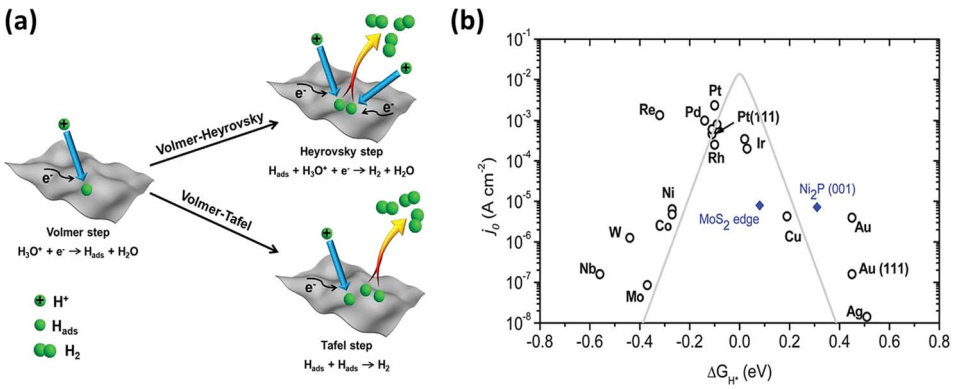

Fig. 3 (a) Pictorial representation of different phases of the HER (reprinted with permission,[56] copyright 2020, Wiley). (b) Volcano curve exhibiting the relationship between current density and free energy (reprinted with permission,[57] copyright 2014, the Royal Society of Chemistry).

$M–H_{ads} + M–H_{ads} \rightleftharpoons 2M + H_2$ (acidic and alkaline medium)(5)

A useful measure of the potential difference needed to increase or decrease the current density by a factor of ten is the Tafel slope (b). This metric sheds light on the underlying mechanism that drives the HER process. Whether b is 0.029, 0.039, or 0.116 V dec^{-1} depends on the type of step in the HER mechanism that determines the pace. The specific value of the Tafel slope depends on whether it includes a chemical desorption step (combination), electrochemical desorption step (Heyrovsky step), or discharge reaction step.[56,60]

The Gibbs free energy of H adsorption (ΔG_H) must be considered in the quest for effective electrocatalysts for the HER. This important parameter, which is usually obtained *via* density functional theory (DFT) simulations, is a major predictor of the reaction barriers and activity enhancements, where $|\Delta G_H| \approx 0$ indicates a notably lower barrier and better catalytic activity.[61,62] The well-known "volcano curve", as shown in Fig. 3b, shows how the exchange current density and ΔG_H are related.[63] The exchange current density decreases on one side of the curve as ΔG_H increases, suggesting that H_2 becomes more unstable on the catalyst surface and complicates the proton transfer, causing H to bind too weakly in this case (right region). Alternatively, with a decrease in ΔG_H, H binds too firmly (left region), and consequently there are less available active sites for H–H coupling on the catalyst surface. According to the Sabatier principle,[64] a good HER electrocatalyst should have a careful binding energy balance. This balance is crucial for both the strong adsorption of H atoms and the facile breakage of M–H_{ads}, leading to the release of H_2 and the exposure of the active sites for subsequent adsorption processes. Essentially, the search for an optimal HER electrocatalyst is based on achieving reasonable equilibrium in the binding between adsorbed H atoms and the active site. In this case, ΔG_H becomes an important criterion given that it affects the overall performance and effectiveness of an electrocatalyst.

2.1.2. OER. Water (H_2O) is oxidized to create oxygen (O_2) in an electrolysis cell during the OER, which is the counter-reaction to the HER. However, the kinetics of this four-proton-coupled electron process are usually slow, requiring a comparatively large overpotential to drive the reaction.[65] Thus, many researchers have devoted their efforts to clarify the possible processes for the oxygen evolution reaction at the anode electrode in both alkaline (eqn (11)–(15)) and acidic (eqn (6)–(10)) environments. Although there are differences and similarities among the suggested pathways, the majority of them have common intermediates, such as MOH and MO. The main difference is the process that produces oxygen. Notably, Fig. 4a depicts two different methods, where the first involves combining 2MO directly to produce $O_{2(g)}$ (eqn (8) and (13)); the second method involves creating the MOOH intermediate (eqn

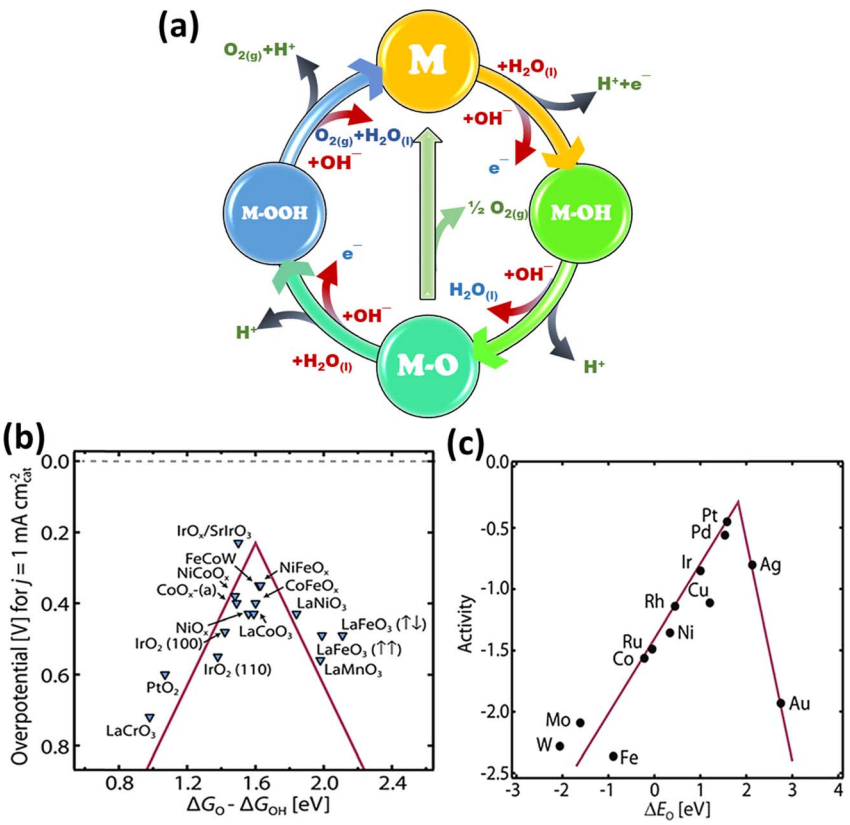

Fig. 4 (a) Schematic of the OER, which depicts the reactions in two different media (black arrow represents acidic and red arrow represents alkaline media), (b) OER volcano plot for various metal oxide catalysts and (c) ORR volcano plot for metal catalysts (reprinted with permission,[63] copyright 2017, *Science*).

(9) and (14)), which then breaks down to release $O_{2(g)}$ (eqn (10) and (15)).[66]

(1) Proposed mechanisms under acidic conditions

$$M + H_2O_{(l)} \rightarrow MOH + H^+ + e^- \quad (6)$$

$$MOH + OH^- \rightarrow MO + H_2O_{(l)} + e^- \quad (7)$$

$$2MO \rightarrow 2M + O_{2(g)} \quad (8)$$

$$MO + H_2O_{(l)} \rightarrow MOOH + H^+ + e^- \quad (9)$$

$$MOOH + H_2O_{(l)} \rightarrow M + O_2 + H^+ + e^- \quad (10)$$

(2) Proposed mechanisms under alkaline conditions

$$M + OH^- \rightarrow MOH \quad (11)$$

$$MOH + OH^- \rightarrow MO + H_2O_{(l)} \quad (12)$$

$$2MO \rightarrow 2M + O_{2(g)} \quad (13)$$

$$MO + OH^- \rightarrow MOOH + e^- \quad (14)$$

$$MOOH + OH^- \rightarrow M + O_{2(g)} + H_2O_{(l)} \quad (15)$$

Despite these differences, it is generally agreed that OER electrocatalysis is diverse. Here, the bonding interactions (M–O) amongst the intermediates (MOH, MO, and MOOH) are found to be important determinants of the overall electrocatalytic efficiency of the reaction.[66] According to earlier theoretical research, understanding the connections among the binding energies of M–O, M–OH, and M–OOH intermediates can be very helpful in understanding the OER process.[67] Plotting the OER catalytic activity of the generally used metal oxides *versus* the Gibbs free energy difference between M–O and M–OH yields a useful visualization that is similar to the volcano-like connection seen in the hydrogen evolution reaction (HER) process (Fig. 4b). This association, which modifies the binding energy of the intermediates, highlights the possibility for modification in catalytic activity.[67] A poisoning effect may arise from too strong binding of intermediates on the catalysts surface, which limits the exposure of the active sites, whereas further activation is impeded by too weak binding of the same. For instance, both theoretical and practical research revealed that the extraordinary OER activity of Ru-based compounds is due to their optimal location near the peak of the volcano. Consequently, the volcano plot functions as a prediction tool that directs the creation of certain electrocatalysts with higher OER activity by adjusting the bond strengths between reaction intermediates and altering surface characteristics.

RuO_2 and IrO_2 are particularly good OER electrocatalysts; however, they are unstable in the electrolyte at a high anodic potential, which causes them to change into oxides with greater oxidation states.[68–70] Also, the constraints of IrO_2 and RuO_2, such as their high cost and scarce reserves, have forced a shift in attention towards non-noble metal electrocatalysts as OER research advances. These materials include perovskites, layered compounds (layered double hydroxides and metal hydroxides), and spinel oxides.[71–74] These non-noble metal electrocatalysts exhibit stability under both highly acidic and alkaline conditions, in addition to being inexpensive and environmentally friendly. Numerous investigations on these substitutes have opened the door for new developments in this field by shedding light on their inherent activity and underlying processes for the OER.

2.1.3. ORR. The oxygen reduction reaction (ORR) is a crucial mechanism that occurs at the cathode and is involved in living phenomena including biological respiration and energy conversion systems such as metal–air batteries and fuel cells.[75,76] The two primary routes by which the ORR proceeds in aqueous solutions are the two-electron transfer pathway from O_2 to hydrogen peroxide (H_2O_2) or HO_2^- (eqn (17) and (20)) depending on whether the electrolyte is acidic or alkaline, and the direct four-electron transfer pathway from O_2 to H_2O or hydroxyl ion (eqn (16) and (19)), respectively. Subsequently, H_2O_2 and HO_2^- is converted to H_2O or a hydroxyl ion (eqn (18) and (21)), respectively. Another one-electron transfer route from O_2 to superoxide (O_2^-) is also possible in nonaqueous aprotic solvents (eqn (22) and (23)). The intricate pathways of ORR are important in many biological and technological settings, impacting how well energy conversion and storage systems work.

(1) Aqueous acidic medium:

$$O_2 + 4H^+ + 4e^- \rightarrow H_2O \quad (16)$$

$$O_2 + 2H^+ + 2e^- \rightarrow H_2O_2 \quad (17)$$

$$H_2O_2 + 2H^+ + 2e^- \rightarrow 2H_2O \quad (18)$$

(2) Aqueous alkaline medium:

$$O_2 + H_2O + 4e^- \rightarrow 4OH^- \quad (19)$$

$$O_2 + H_2O + 2e^- \rightarrow HO_2^- + OH^- \quad (20)$$

$$HO_2^- + H_2O + 2e^- \rightarrow 3OH^- \quad (21)$$

(3) Non-aqueous alkaline medium:

$$O_2 + e^- \rightarrow O_2^- \quad (22)$$

$$O_2^- + e^- \rightarrow O_2^{2-} \quad (23)$$

The electron transport phases in the oxygen reduction reaction are individually significant and vital to many applications. Fuel cells, which are dependent on the 4-electron transfer, can achieve effective energy conversion.[77] However, the intermediate species formed during the process, and also the two-electron and one-electron transfer reactions result in sluggish reaction kinetics in fuel cells, making it imperative to use a cathode ORR electrocatalyst to accelerate the ORR kinetics. Among the metal catalysts, platinum stands out as the best option due to its exceptional ORR efficiency. Pt is positioned at the top of the volcano plot, as shown in Fig. 4c, which highlights its highest efficiency by linking theoretical ORR activity with the

free energy of the intermediate reactions on a densely packed metal surface.[64] However, although platinum is an excellent catalyst for oxygen reduction, its high cost and limited durability hinder its use in large-scale metal–air batteries. This has prompted the investigation of substitute ORR electrocatalysts. A wide range of materials has attracted interest, including metal oxides, noble metal alloys, chalcogenides, carbon compounds, transition metal carbides (TMC), phosphides, and nitrides.[78–81] By providing viable solutions to the cost and durability issues of platinum catalysts, these substitutes can improve the efficiency of the ORR and are suitable for use in a range of energy storage and conversion systems.

2.1.4. CO_2 RR. The increasing atmospheric concentration of CO_2 has sparked significant interest in CO_2 reduction technology. The CO_2 molecule is completely oxidized and thermodynamically stable, with a C=O bond energy of 805 kJ mol^{-1}.[82] This stability creates a substantial energy barrier, and to generate the intermediate $CO_2^{\bullet-}$ radical ion in CO_2RR, a high negative potential of −1.90 V *vs.* the standard hydrogen electrode is needed.[83] The first stage in CO_2RR is the stabilization of the $CO_2^{\bullet-}$ radical ion or other intermediates on the surface of electrocatalysts. The obtained product is determined by the desorption properties of the intermediates on the surface of different electrocatalysts. For example, according to the Bronsted–Evans–Polanyi (BEP) relation, weaker CO adsorption on the electrocatalyst surface is crucial for lowering the C–C coupling barrier to form multi-carbon products such as ethylene and ethanol. However, according to the adsorption scaling relation, protonation to form key intermediates such as COOH, CHO, and OCCOH is challenging on weakly reactive catalysts, and excessively weak CO binding energy may favour the desorption of CO rather than the formation of multi-carbon products.[84] Therefore, to achieve CO_2 reduction at lower potentials with excellent selectivity towards the intended product, choosing the right electrocatalyst is crucial. Depending on how many electrons are engaged in the route, different CO_2 reduction products are formed. Formic acid and carbon monoxide, formaldehyde, methanol, methane, and ethylene/alcohols are the byproducts of the two-, four-, six-, eight-, and twelve-electron pathways, respectively. Table 1 displays the half-reactions and associated E^0 values obtained from thermodynamic studies.

Table 1 Standard electrode potentials for CO_2 conversion in aqueous solutions

Half-cell reactions of CO_2 reduction	Electrode potential, E^0 (V *vs.* SHE @ pH 7)
$2CO_2 + 12H^+ + 12e^- \rightarrow C_2H_5OH + 2H_2O$	−0.33
$2CO_2 + 12H^+ + 12e^- \rightarrow C_2H_4 + 4H_2O$	−0.35
$2CO_2 + 6H^+ + 6e^- \rightarrow CH_3OH + H_2O$	−0.38
$2H^+ + 2e^- \rightarrow H_2$	−0.42
$CO_2 + 4H^+ + 4e^- \rightarrow HCHO + H_2O$	−0.51
$CO_2 + 2H^+ + 2e^- \rightarrow CO + H_2O$	−0.53
$CO_2 + 2H^+ + 2e^- \rightarrow HCOOH$	−0.61
$CO_2 + e^- \rightarrow CO_2^{\bullet-}$	−1.90

Notably, the equilibrium electrode potential for HER is also listed in the above-mentioned table, highlighting its close proximity to that of the CO_2RR pathways. This leads to unavoidable competition between HER and CO_2RR in aqueous systems, resulting in the formation of undesirable side products, such as H_2. Accordingly, suppressing HER by using metals such as Cu, Ag, and Au or alloying suitable metals such as Cu–Zn and Cu–In as electrocatalyst materials, together with the appropriate surface modification of catalysts and other techniques can help mitigate this issue.[85–87] Given the coexistence of multiple proton-coupled electron transfer pathways can lead to various products, the selectivity of the desired product is measured by the faradaic efficiency (FE). The FE is calculated using eqn (24), where F is the Faraday constant, n is the number of electrons transferred per mole of product, N is the number of moles of product obtained, and Q is the total charge consumed by the electrolysis. Although a suitable catalyst reduces the activation energy barrier and increases the selectivity for the desired product, other factors such as mass transfer and counter anodic reactions can significantly influence the kinetics of CO_2RR. Another technique to overcome these barriers and enhance the reaction kinetics is the use of an external magnetic field, which is discussed further in the text.

$$\mathrm{FE} = \frac{nFN}{Q} \times 100\% \tag{24}$$

3. Fundamentals of magnetoelectrochemistry

Various aspects related to a magnetic field have been observed to significantly impact energy conversion applications, as shown in Fig. 5. These effects, whether considered individually or collectively, exert substantial influence on the electrochemical parameters such as current density, overpotential, Tafel slope, charge transfer resistance, onset potential, turnover frequency, and stability. The magnetic parameters can have an influence on the charged species or magnetic matter in the electrolyte, thereby impeding their diffusion, for instance, the magnetothermal effect. Also, Kelvin force, which results from the interplay between electric and magnetic fields, can enhance the velocity of paramagnetic materials. Additionally, Maxwell stress may alter the formation of an ionic cloud at the electrode–electrolyte interface. Forces such as Lorentz force can aid in the easy release of gas bubbles from the electrode surface. Moreover, certain effects may facilitate the manipulation of the spin configurations in magnetic materials. These magnetic field-related effects are extensively discussed in the subsequent sections.

3.1. Mechanisms involved in magnetic field-enhanced electrocatalysis

3.1.1. Magnetohydrodynamic effect. The problem of gas bubbles sticking to the catalyst surface frequently encountered in electrocatalytic gas evolution processes, which hinders the

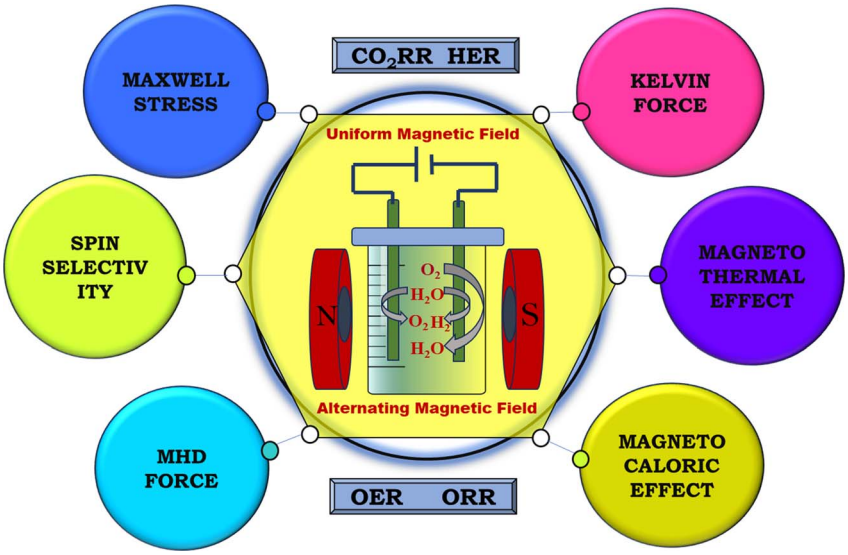

Fig. 5 Schematic of the various magnetic field effects during the fabrication of electrodes and electrolysis.

flow of the reaction intermediates to the active sites.[88] This obstacle creates a second barrier to charge transmission at the interface of the electrolyte and the catalyst.[89,90] Although these effects can be substantially mitigated by morphology/structure engineering,[91] an alternative approach is to employ the Lorentz force produced by an external magnetic field inside the reaction system. The magnetic field effect in a complete electrocatalytic system modifies the velocity of fluid and bubbles by causing Lorentz force to be generated by the interaction of a magnetic field with the local current density. Eqn (25),[92] where B is the magnetic induction vector and J is the voltage field, describes the correction between the Lorentz force (F_L) and magnetic field strength.

$$F_L = J \times B \tag{25}$$

It is important to note that B, j, and F_L are vectors, meaning they have both magnitude (or module) and direction. The direction of F_L is perpendicular to the plane formed by B and J and it follows Fleming's left-hand rule, as illustrated in Fig. 6a (perpendicular to both the current and magnetic field). The magnitude of F_L is determined by the magnitudes of B and J and the angle θ between them; F_L reaches its maximum value when B and J are orthogonal.

Another key aspect is the convective current driven by the Lorentz force, which is known as the magnetohydrodynamic (MHD) effect. The MHD effect induces convection in the electrolyte on both macroscopic and microscopic scales. In 2004, Willner *et al.* developed a theoretical hydrodynamic model describing the impact of the Lorentz force on planar semi-infinite electrode surfaces.[93] They discovered that applying a magnetic field reduces the thickness of the diffusion boundary layer, which enhances the supply of active species and increases the mass-transfer-limited current. The MHD effect also improves the electrocatalytic reaction by decreasing the ohmic polarization, activation potential, and concentration polarization.[94] Ions subjected to a continuous Lorentz force perpendicular to their motion migrate in a circular path, acting as micro stirrers that enhance the convection of reactants and products. This reduces the polarization resistance and accelerates the detachment of gas bubbles from the surface, exposing more active sites to the reaction intermediates, and thereby accelerating catalysis.

The inhomogeneous current at the edges of the electrode causes the electric field lines to bend and intersect with the magnetic field, sometimes leading to perturbations and microscopic MHD effects due to the Lorentz force (Fig. 6b and c).[95,96] This micromagnetic fluid effect can accelerate the diffusion of dissolved gases.

3.1.2. Magnetothermal effect or magnetic hyperthermia. The magnetothermal (MT) effect is an external factor that adds a new dimension to electrocatalysis. According to this phenomenon, high frequency magnetic nanoparticles produce localized magnetic heat.[40,97] This effect is seen in various materials exposed to a changing magnetic field, particularly when subjected to high-frequency rotating or alternating magnetic fields (RMF or AMF). When AMF or RMF is applied to ferromagnetic, ferrimagnetic, and antiferromagnetic materials, the magnetothermal effect is especially notable because of its predominant behaviour of localized heating or hyperthermia.[98] The increase in temperature amplitude is closely related to the alternating frequency of the magnetic field rather than being entirely dependent on the magnetic states. The Arrhenius equation,[99] as shown in eqn (26),

$$k = Ae^{-E_a/RT} \tag{26}$$

describes the relationship between temperature (T) and the rate constant (k), where T is the absolute temperature, A is the pre-exponential factor, also known as the frequency factor, E_a is the activation energy for the reaction, and R is the universal gas constant. According to a rough estimate, the rate of the reaction

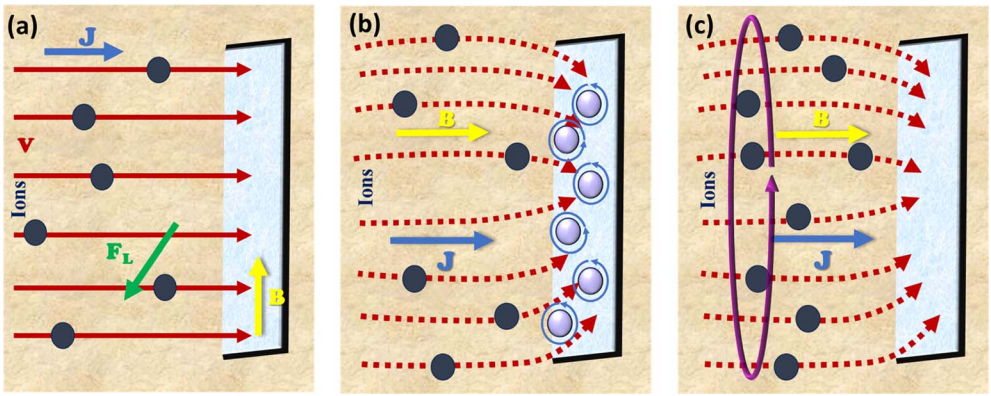

Fig. 6 Illustration of the magnetic field effects in an electrocatalytic system, showing the relationship between current density, J, magnetic field, B and Lorentz force, F_L: (a) J is normal to the electrode surface and B is parallel, (b) both J and B are normal to the surface with MHD flow appearing at the corners and (c) micro MHD action developed in the system.

increases by more than a factor of two with every 10 °C increase in temperature.[100] In the case of magnetic electrocatalysts/electrodes, continuous local heating under an AMF may be achieved, as seen in Fig. 7a, leading to enhanced thermodynamics and a notable reduction in the overpotential, whereas continuous heating using traditional heating techniques will erode the material.[101] Experimental systems have confirmed that the kinetics and mass transfer of ions and gaseous species in electrocatalytic processes are positively influenced by an increase in the temperature of the electrolyte. Also, the critical metrics including Tafel slope, charge transfer resistance, overpotential, and electrochemical double-layer capacitance display vary with temperature under suitable conditions.[102,103]

A study on the efficiency of high-frequency magnetic heating of nanoparticles presents the idea of specific loss power (SLP), which is the amount of heat lost per unit mass through a magnetic particle.[104,105] Eqn (27) defines the SLP.

$$\mathrm{SLP} = \frac{\mu_0 \pi \chi''(f) H^2 f}{\rho \Phi} \tag{27}$$

The important parameters including the imaginary portion of susceptibility (χ''), the density (ρ) and volume percentage (Φ) of nanoparticles, and the magnetic field frequency (f) all play significant roles. This suggests that the strength and frequency of the magnetic field have a significant impact on the heating

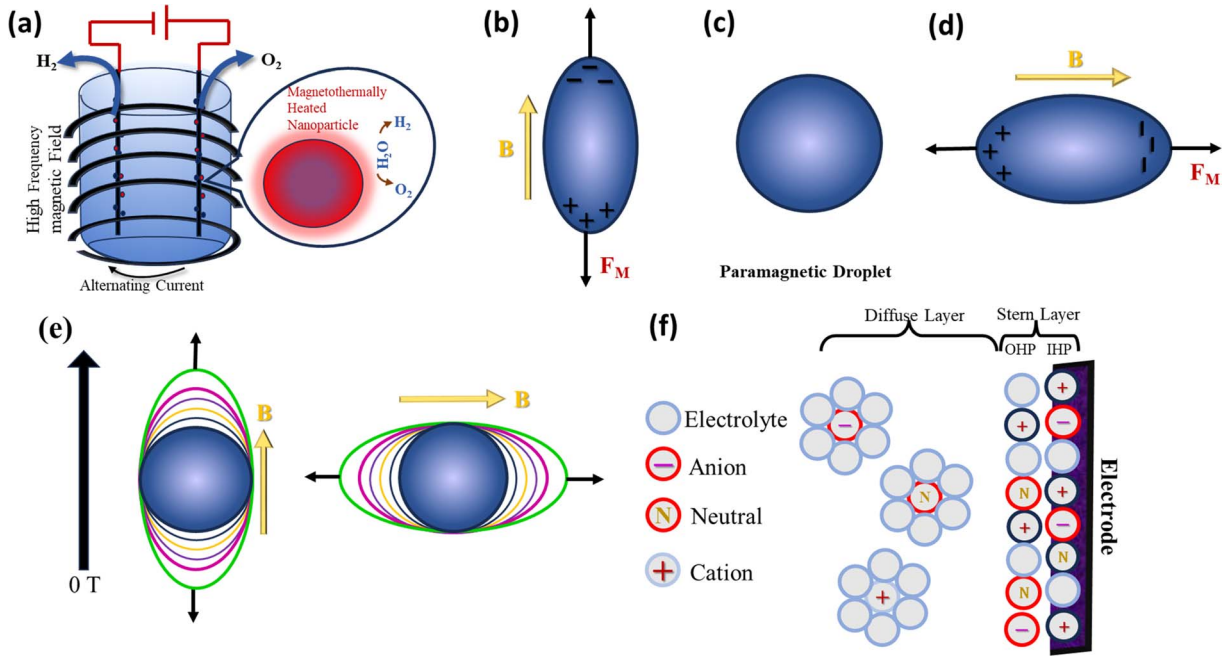

Fig. 7 (a) Localized heating of the magnetic nanoparticles on an electrode by an alternating magnetic field, leading to enhanced activity, (b–e) directional elongation of a paramagnetic droplet depending on the direction of the external magnetic field and (f) electrode/electrolyte interface, which is comprised a Stern and diffuse layer, where the former is sub-divided into the inner and outer Helmholtz planes.

efficiency.[106] Furthermore, the nanomagnetic characteristics of nanoparticles, such as saturation magnetization and magnetic anisotropy, also have a major impact on the SLP value.[107] The magnetic losses related to the thermogenic behaviour of magnetic nanoparticles is attributed to Néel and Brown relaxation.[108] The spinning of magnetic nanoparticles in solution causes friction with the surrounding fluid and the production of heat, which is because of Brown relaxation.[109] Conversely, the internal thermal rotation of nanoparticles inside their crystal structure causes Néel relaxation.[110] Néel relaxation is dominant for smaller particle sizes, whereas Brown relaxation has a more pronounced effect on bigger sizes. Thus, manipulating the size, content, and shape of magnetic nanoparticles can optimize the effectiveness of magnetic heating and provide a technique to improve their thermogenic characteristics for a range of applications.

3.1.3. Maxwell stress effect. A magnetized body/paramagnetic element inside a uniform field experiences magnetic stress when an external magnetic field interacts with its dipole moment (eqn (28)).[111] Essentially, this magnetic stress has a demagnetizing effect on a paramagnetic droplet. A demagnetizing field is created as a result of the build-up of positive and negative surface charges at the end faces of the droplets. To lessen this impact, as illustrated in Fig. 7b–e, the paramagnetic droplet is extended either longitudinally or transversely, depending on whether the stress is developed vertically or horizontally.[41,112] This enables a more practical depiction of the total energy minimization under volume conservation in the presence of an external magnetic field.

$$F_m = MB \tag{28}$$

It is important to note that the amount and direction of paramagnetic droplet stretching are determined by the strength and direction of the applied magnetic field. The interfacial tension, adhesion, wettability, and contact angle on solid surfaces are all impacted by this stretching.[112] Accordingly, the form of the ion cloud dispersed at the electrode/electrolyte interface may be changed by applying a magnetic field.[113] The structure of the interface, which consists of a Stern layer and diffusion layer and includes outer and inner Helmholtz planes in the Stern layer, which is important in controlling the kinetics of the electrode responses, as depicted in Fig. 7f. Specifically, the paramagnetic radicals in the solution close to the electrodes are susceptible to the effects of Maxwell stress, which can change the outer Helmholtz plane and affect the electrochemical bilayer capacitance.[114,115] Given that the bilayer capacitance and electrochemically active region are correlated in electrocatalytic reactions, there is a possibility that the Maxwell stress effect will increase the electrocatalytic activity.

Although previous research emphasizes how Maxwell stress affects the electrochemical double layer, and consequently the double layer capacitance, there is no tangible proof that it has a beneficial effect on the electrocatalytic activity of catalysts. The recognition that Maxwell stress may impact the electrochemical double-layer capacitance (EDLC, C_{dl}) underscores the need for further exploration. Gaining an understanding of its possible impact in electrocatalytic processes is essential for gaining fresh perspectives and maximizing the efficiency of catalysts. This feature offers opportunities for targeted studies to determine how Maxwell stress affects electrocatalytic systems.

3.1.4. Spin selectivity effect. The spin selectivity effect originates from the chiral-induced spin selectivity (CISS) effect.[116] This phenomenon involves the spin-specific transmission of electrons through a chiral molecular film, meaning that a chiral molecule only allows electrons with a specific spin to pass through.[117] It was first observed in a groundbreaking study where chiral molecules were shown to transfer electrons with a preferred spin orientation. Because of this spin filtering characteristic, chiral molecules can be employed as ferromagnetic electrodes in giant magnetoresistance.[118] Chiral catalysts have been found to exhibit an exceptional ORR performance, improved electron transmission for O_2 evolution, and inhibition of H_2O_2 generation.[119,120] Fig. 8a illustrates how CISS catalysts manage the intermediates on the catalyst surface to organize in a spin parallel way ($OH\uparrow \times \uparrow OH$). The observed effect can be clarified by considering the enhanced energy pathway for electron transfer during polarization. Specifically, when OH^- radicals undergo reactions to form O_2, their electronic spins become aligned accordingly. This alignment leads to interactions on a triplet potential, resulting in the production of triplet oxygen. Remarkably, in this scenario, the formation of peroxide is forbidden due to symmetry constraints.[123] The synchronization of electronic spins plays a pivotal role, influencing the reaction outcome and favouring the creation of triplet oxygen over peroxide formation.

Similarly, it has been demonstrated that the spin selectivity in electrocatalytic processes is significantly influenced by a magnetic field. In these processes, the spin states of oxygen species are either antiparallel (singlet ($\uparrow\downarrow$)) or parallel (triplet ($\uparrow\uparrow$)). During oxygen evolution, the ground state involves parallel alignment, while the excited state involves antiparallel alignment. As illustrated in Fig. 8b, the energy profile of the OER changes with and without spin alignment of the electrocatalyst. According to density functional theory simulations, the excited state is more than 1 eV energetic than the ground state, making the spin-aligned approach thermodynamically preferable.[124] When an external magnetic field is applied, it encourages the formation of parallel configurations in the active sites of the catalyst by enhancing the ferromagnetic regions and suppressing antiferromagnetic regions. This is because antiferromagnetic regions favour the singlet state configuration of oxygen species ($\uparrow O\cdots O\downarrow$ and $\uparrow O\text{–}O\downarrow$), while ferromagnetic regions favour the triplet state ($\uparrow O\cdots O\uparrow$ and $\uparrow O\text{–}O\uparrow$). Essentially, a magnetic field helps stabilize the more energy-efficient triplet state, facilitating a smoother and more effective oxygen evolution process.

By facilitating the transition from singlet to triplet spin states, the presence of an external magnetic field not only enhances the overall activity of the OER but also improves the efficiency of electrocatalytic processes. There are two ways to understand how an applied magnetic field affects electrocatalysis. Firstly, it can induce the interconversion of two spin states, which controls the outcome. Secondly, a magnetic field

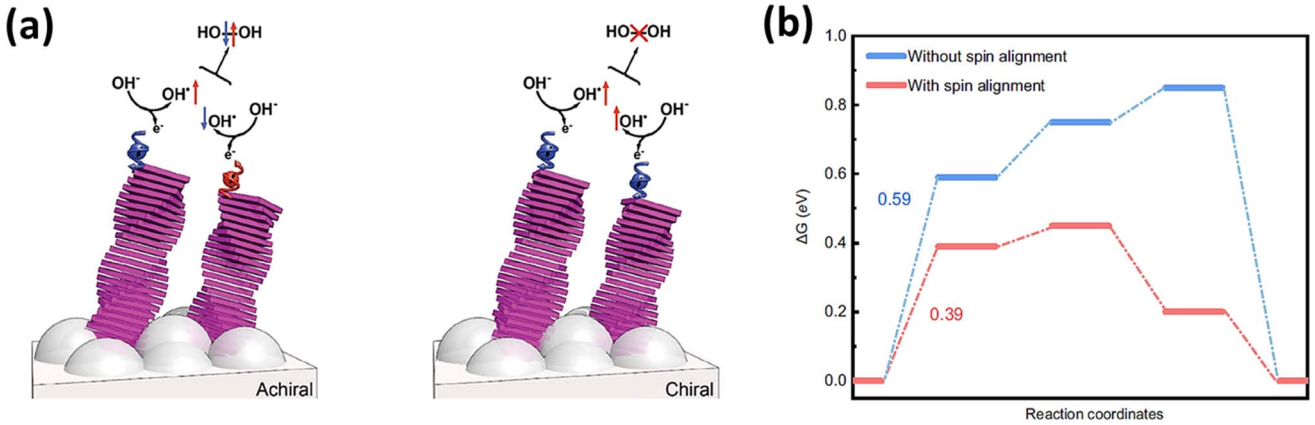

Fig. 8 (a) Organizing the spin polarity of the intermediates by CISS catalysts to inhibit H_2O_2 formation (reprinted with permission,[121] copyright 2018, Wiley) and (b) free energy diagram of the OER with and without spin alignment on the surface of the electrocatalyst (reprinted with permission,[122] copyright 2021, *Nature Comm.*).

can cause the intermediates adsorbed on the catalyst surface to flip in orientation, thereby optimizing the reaction route and increasing the reaction efficiency.[121] In the form of a restricted or unconstrained spin state, magnetic field-induced spin selectivity (FISS) will be the best possible course to increase the electrochemical reaction efficiency.

3.1.5. Kelvin force effect. When a magnetic field is nonuniform, it exerts distinct forces on paramagnetic and antimagnetic species, influencing their movement within the solution. Paramagnetic species are drawn toward regions of higher magnetic field strength, while antimagnetic species are pushed in the direction of weaker magnetic fields.[125,126] This phenomenon is described by the Kelvin force density formula (eqn (29)), as follows:

$$F_K = \frac{1}{2}\mu_0 c \chi_m \nabla B^2 \quad (29)$$

where μ_0 represents the permeability of free space, ∇B is the gradient of the magnetic induction, and χ_m and c denote the molar magnetic susceptibility and the concentration of electroactive species in the bulk, respectively. Unlike Lorentz force, $F_L = J \times B$, which has limitations due to the maximum current that can safely pass through the electrolyte, the Kelvin force can be substantially increased by patterning ferromagnetic elements on the microscale.[126] This creates a rapidly varying magnetic stray field in the electrolyte, leading to a Kelvin force that can reach as high as 106 or 107 Nm^{-3}, although these forces are localized around the ferromagnetic elements. A stronger Kelvin force induces a more potent magnetic field and a greater magnetic field gradient. Consequently, this enhances the paramagnetic susceptibility, accelerating material transfer, promoting convection, and reducing the diffusion layer thickness, thereby enhancing the electrocatalytic effect.[96,127]

Unlike the Lorentz force, which drives magnetohydrodynamic (MHD) convection through an electric current, Kelvin force is not conservative when there is a nonuniform distribution of paramagnetic species. This leads to convection near the electrode with a paramagnetic concentration gradient.[128] The Kelvin force can influence electrochemical processes in two ways. Firstly, it accelerates the mass transfer rate of paramagnetic materials, increasing the reaction rate near the electrode.[129] For instance, O_2 is often produced at the electrode surface during the oxygen evolution reaction and its products can block the electrochemically active sites. This prevents the subsequent adsorption of O_2, reducing the electrochemical efficiency and causing concentration polarization.[130] Secondly, the increased convection can thin the diffusion layer and increase the limiting current when the field gradient is perpendicular to the concentration gradient.[128] This aligns with the theoretical hydrodynamic model of a magnetic field acting on a flat, semi-infinite electrode surface. The Kelvin force can help address challenges in using air as a raw material in cathode reactions by attracting paramagnetic oxygen, enriching the gas, and increasing the air flow velocity at the interface. This improves the performance of electrocatalysts by promoting the oxygen flow in the reaction zone.

4. Magnetic field-enhanced catalyst fabrication: theoretical aspects and recent advances

The catalyst is the core element of electrocatalysis. The basic idea of fabricating electrocatalysts by using different techniques is to manipulate the structure and morphology of the catalyst material, which play a significant role in improving the performance of electrocatalysts towards electrochemical reactions.[123] The use of external aids for the construction of better electrocatalysts is attracting increased attention from researchers.[131–133] Herein, we focus on the use of a magnetic field as an external aid for the preparation of electrocatalysts, specifically, the magnetic field-assisted fabrication of electrodes to achieve a thorough performance in electrocatalysis. Generally, the properties of catalyst materials such as their band gap, structure and morphology can be changed accordingly using a magnetic field for catalysts fabrication.[94] During the

preparation of an electrocatalyst, when the precursor materials are exposed to a magnetic field, they become aligned in a particular direction as a result of getting magnetized as tiny magnetic dipoles, and eventually this alignment can be exploited to regulate the properties of catalysts such as increasing the electrochemically active surface area, kinetics of electrochemical reactions, and transport of ions.[134] Furthermore, the use of a magnetic field for the fabrication of electrodes is regarded as pollution free and non-toxic because of the lack of external template by-products during their synthesis. Moreover, the complex additional and tedious preparation procedures generally used to regulate the morphology, crystallinity, *etc.* can be avoided by using a magnetic field as an external agent. The fabrication of electrocatalysts for electrocatalytic reactions and the major aspects involved such as shape regulation and surface structure modulation have been discussed much more comprehensively and specifically explained in the review by Kun Wang *et al.*[48] Herein, in the subsequent sections, we broadly discuss some aspects related to magnetic fields and the impact of magnetically fabricated electrocatalysts in the overall electrocatalytic performance in reactions.

4.1. Magnetocaloric effect/magnetic induction heating

Lord Kelvin, also known as William Thomson, reported the theoretical prediction of the magnetocaloric effect (MCE) in 1860, based on thermodynamic principles. According to his argument, iron would experience cooling upon removal from a magnetic field and warming when introduced into one.[135] The magnetocaloric effect is defined as the alteration in temperature or entropy of magnetic materials due to changes in a magnetic field.[136] The total magnetic entropy (S_T) of these materials under a constant pressure is given by eqn (30), as follows:

$$S_T(H,T) = S_M(H,T) + S_r(T) + S_e(T) \quad (30)$$

where S_T represents the total entropy, S_M is the magnetic entropy, S_r accounts for the lattice entropy caused by crystal lattice vibrations, and S_e is the electronic entropy associated with the free electrons in the material.[137] During the isothermal magnetization process, both the lattice entropy and electronic entropy remain unaffected by an applied magnetic field. When these materials undergo magnetization, their magnetic moments align with the applied magnetic field, leading to a decrease in both the magnetic and total entropy. Under adiabatic conditions, where no heat exchange occurs, the total entropy remains constant. Thus, if the reduction in magnetic entropy is balanced by an increase in lattice entropy, the temperature of the material increases because of the magnetization process.[138]

The synthesis of electrocatalysts *via* conventional hydrothermal methods requires a temperature of 150 °C or above, which is a major drawback given that it requires more time to heat, and then to cool back to room temperature, wherein the whole system together with the target material gets heated, as shown in Fig. 9a.[143] Alternatively, in the case of induction heating by an alternating magnetic field, conductive paramagnetic or ferromagnetic materials get heated by an eddy current based on Faraday's law of electromagnetic induction,[144] keeping the surrounding temperature constant, which is more suitable for constructing nanomaterials. Xiong *et al.*[139] used the magnetic field-driven induction heating method to fabricate an Ni–MoO_2-based electrocatalyst on nickel foam as a substrate. Fig. 9b and c depict a schematic of using water and closed gas systems for the anchoring process, respectively. Notably, in the closed gas system, the anchoring of the material was achieved in just 2 min. This group achieved enhanced overpotential values with electrocatalysts prepared using the induction heating method compared to the traditional heating procedure. They also observed the defects created on the surface of the catalysts, which can be attributed to the non-equilibrium state induced in the crystal due to the rapid heating and cooling process, as depicted in Fig. 9d. Lu *et al.*[140] utilized the ultrafast magnetic induction heating/rapid quenching (MIHRQ) method to swiftly synthesize carbon-supported NiFe spinel composites with enhanced electrocatalytic performances towards OER, emphasizing the potential of MIHRQ in the fabrication of nanocomposites. Fig. 9e visually depicts the heating of the catalyst material in a current solenoid. This group achieved an overpotential value of 260 mV to reach a current density of 100 mA cm^{-2}, and the theoretical and experimental studies provided proof that the rapid heating and quenching process favoured Ni and Fe phase segregation, leading to a Cl-enriched surface, favouring an enhancement in the electrocatalytic process. Usually metal-carbon nanocomposites are prepared *via* tedious pyrolysis methods, but Liu *et al.*[141] employed an effective technique to fabricate Co/C nanocomposites utilizing magnetically induced heating. They varied the induction current between 100 A and 600 A to produce a magnetic field. The magnetic field generated with a current of 400 A exhibited a superior OER performance, surpassing even the commercial RuO_2 electrocatalyst at a high current density of 200 mA s^{-1}. The TEM image in Fig. 9f depicts that the Co nanoparticles were encapsulated within N-doped carbon shells. Similarly, Liu *et al.*[145] utilized this technique to create amorphous $Mo_3S_7Cl_y$-like structures, employing a 200 A induction current in the coil. The resulting electrocatalyst exhibited a notable HER performance. However, an increase in the induction current led to a decrease in HER activity due to the formation of dimeric Mo_6S_{14} moieties in the amorphous MoS_x, which was facilitated by the loss of Cl residues during electrochemical reactions. Likewise, the induction heating method was employed by Liu *et al.* to produce Ru nanoparticles supported on carbon paper to study the HER activity of the Cl-enriched surface of the obtained electrocatalyst.[142] The most effective sample was heated for 6 s with a 300 A induction current. Using $RuCl_3$ salt as the precursor and shorter heating durations resulted in incomplete decomposition, leaving Cl residues on Ru. Theoretical DFT studies validated the significant influence of Cl on the electronic structure of metallic Ru and the adsorption energetics of H. The XPS analysis, as shown in Fig. 9g, corroborated the incomplete decomposition of $RuCl_3$ and revealed that an increase in the induction current reduced the content of $RuCl_x/RuO_y$ species, which can be interpreted by the

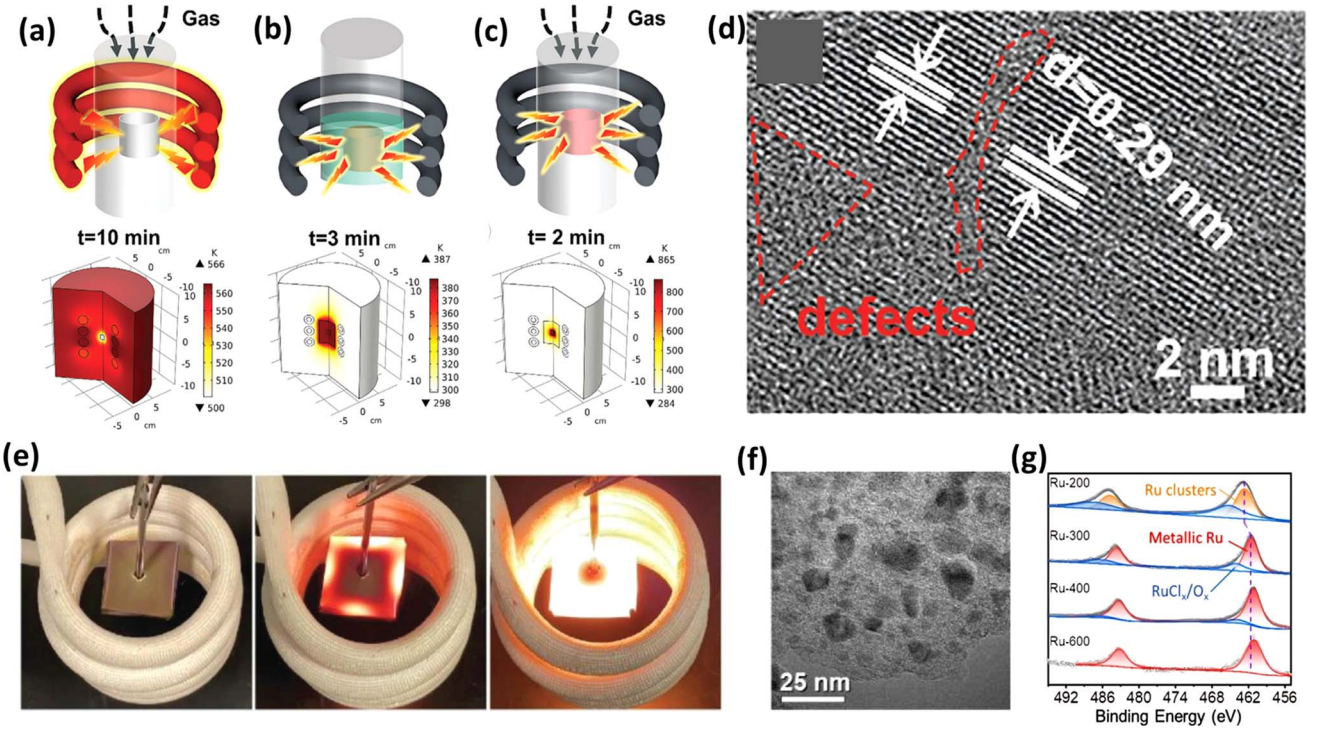

Fig. 9 (a) Illustration of the drawback of the conventional continuous heating method causing the heating of the whole material, (b and c) depiction of induction heating under water and gas environments, respectively, (d) SEM image of the as-prepared electrocatalyst (reprinted with permission,[139] copyright 2021, Wiley), (e) real-time images of induction heating using a solenoid (reprinted with permission,[140] copyright 2022, Research), (f) TEM image of Co-NC (reprinted with permission,[141] copyright 2023, Elsevier) and (g) XPS spectra of Ru (reprinted with permission,[142] copyright 2022, Wiley).

decrease in peak area at around 465 eV, representing the oxides and chlorides.

4.2. Electrodeposition in the presence of a magnetic field

The method of depositing a powdered catalyst onto a conductive substrate with a binder has been extensively studied and is widely used in electrocatalysis.[146–148] However, this approach has limitations such as the formation of thick catalyst layers, leading to high ohmic resistance, incomplete utilization of the catalyst due to buried active sites, and imperfect adhesion at the catalyst/substrate interface.[149,150] Accordingly, the electrodeposition of catalysts has emerged as an alternative to address these challenges. Additionally, the use of an external template during the electrodeposition process offers further opportunities to control the properties of catalysts. The template can help homogenize the thickness of the catalyst layers, modify the morphology of the deposited layers, facilitate the growth of catalysts in nanowire-like structures, and prevent the agglomeration of nanoparticles.[151–154] One external template, although less explored, is an external magnetic field.

Nickel, a transition element in the d-block, has been extensively studied for various electrochemical applications in the form of alloys and composites, which also exhibit promising activity for HER and OER.[155,156] Chen *et al.* investigated the effects of the magnetic field-controlled bubble template-assisted electrodeposition of porous CuNi films on Si/Ti/Au chips as the substrate.[157] They studied alterations in surface morphology, crystallographic structure, and composition. Related to the motion of gas products, this group studied the combined effect of Lorentz and buoyancy forces, which when aligned in the same direction may cause the accelerated motion of the gas-phase products. Fig. 10a explains that when the direction of the magnetic field is reversed, it causes a decrease in the frequency of bubble detachment. During the synthesis of catalysts, it is necessary to maintain the proper orientation and current density, which can afford control of the pore size of electrocatalysts, as shown in Fig. 10b. This group synthesized four different electrocatalysts by varying the current density during electrodeposition in the range of -0.7 to -3.5 A cm^{-2}. In alkaline media, the CuNi film prepared at -1.5 A cm^{-2} exhibited the lowest overpotential of -38 mV at a current density of 10 mA cm^{-2} and a Tafel slope of 60.8 mV dec^{-1}, as evident in Fig. 10c. Similarly, Elsharkawy *et al.* pursued an alternative method to fabricate Ni films on a Cu substrate.[158] Firstly, they optimized the pH, deposition potential, and electrolyte conditions for electrodeposition. Their study focused on understanding how the electrocatalytic activity of deposited Ni correlates with its wettability. Ultimately, they achieved the optimal performance with the electrodeposited Ni film for HER under alkaline conditions, using citrate as the electrolyte during deposition. This group achieved an overpotential of 231 mV at a current density of 10 mA cm^{-2}.

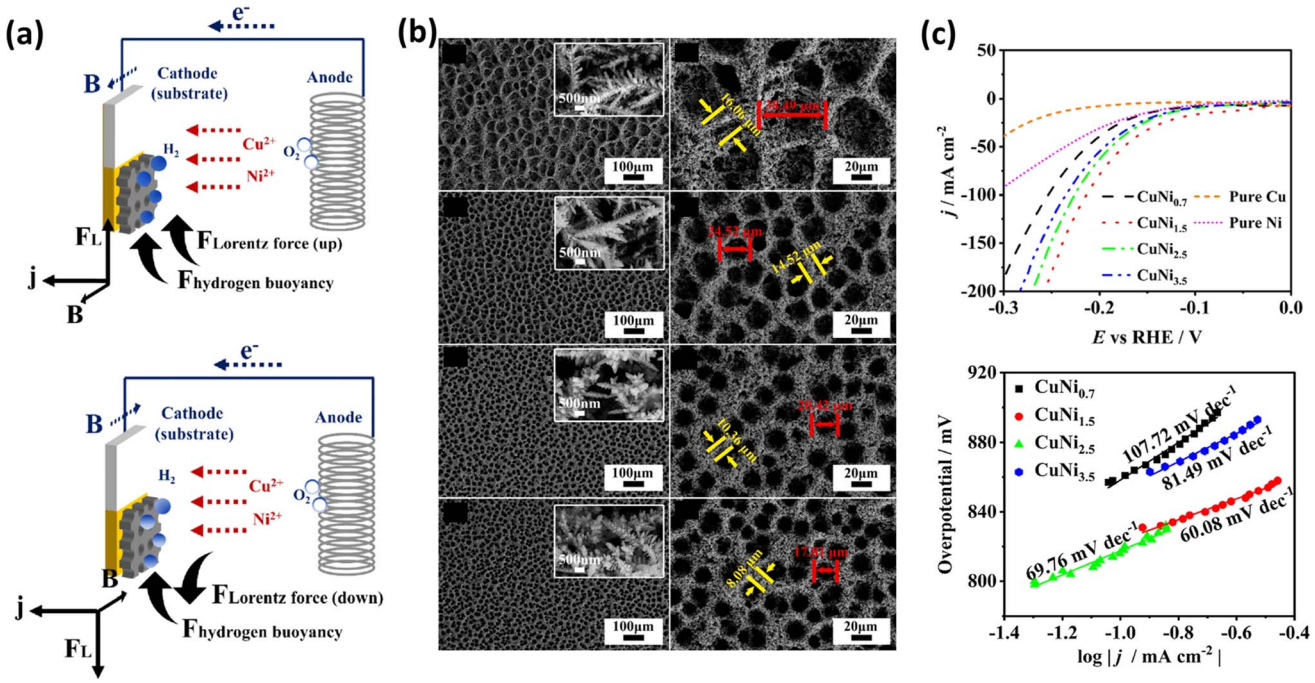

Fig. 10 (a) Schematic of magnetic field-controlled electrodeposition with upward and downward Lorentz force. (b) Low- and high-magnification images of CuNi films deposited with upward Lorentz force at different current densities. (c) LSV curves and Tafel plots of the electrocatalyst (reprinted with permission,[157] copyright 2024, Elsevier).

In an alternative approach, Wang *et al.*[159] utilized a 600 mT magnetic field for the electrodeposition of NiCoP on a carbon paper substrate, and the resulting NiCoP-600 structure exhibited a unique appearance, resembling a dense braided rope, as depicted in Fig. 11a and b, respectively. COMSOL simulations, as shown in Fig. 11c, provided insight into this distinctive structure, demonstrating that in the absence of a magnetic field, the catalyst particles tended to deposit on raised surfaces, forming other nanosheet-like structures. Conversely, the presence of a magnetic field altered the direction of the particle motions due to the Lorentz force, allowing the particles to settle evenly across the surface, forming the structure. This electrocatalyst demonstrated a good performance in both acidic (0.5 M H_2SO_4) and alkaline (1 M KOH) conditions, qualifying it as a bifunctional electrocatalyst. The HER measurements revealed an overpotential of 48 mV at a current density of 10 mA cm^{-2}, with a Tafel slope value of 54 mV dec^{-1}, as evident in Fig. 11d. The same electrocatalyst was also tested for its OER performance under alkaline conditions, in which the performance of NiCoP-600 increased by 13% compared to NiCoP. Jiang *et al.*[160] utilized scanning electrodeposition to fabricate NiCoP–Fe_3O_4, whereby nano-sized Fe_3O_4 particles were deposited onto NiCoP by controlling the magnetic field. The electrocatalyst exhibited a good OER performance with an overpotential of 256 mV at a current density of 10 mA cm^{-2} and a Tafel slope of only 55 mV dec^{-1}. In a different approach to enhance the OER activity of Ni, Zhu *et al.* fabricated an Ni and Ta-based composite using a graphite sheet substrate using magnetic field-assisted electrodeposition.[161] The resulting catalyst exhibited an overpotential of 256 mV cm^{-2} and a Tafel slope of 89 mV dec^{-1} under alkaline conditions (1 M KOH). The combined effect of Ni and Ta enhanced the intrinsic catalytic activity of the electrode. DFT calculations provided insight into this synergistic effect, as depicted in Fig. 12a, indicating a significantly higher total intensity of DOS near the Fermi level for Ni–Ni/Ta compared to bare Ni. This suggests that the incorporation of Ni/Ta in the electrodes could appreciably improve their electrical conductivity, and thereby improve their electrochemical performance. Achieving a consistent coating of metallic elements on surfaces is a significant challenge; however, Sheelam *et al.* showcased a method for uniformly and precisely coating Pd onto the surface of MoS_{2-x}.[163] Initially, MoS_{2-x} was exfoliated from bulk MoS_2 and desulfurized to introduce surface defects. The uniform dispersion of the metal was facilitated by magnetic field-assisted electrodeposition. The resulting electrocatalyst, prepared under the influence of a magnetic field, demonstrated a 1.6-fold increase in HER mass-activity.

In a separate experiment, Li *et al.*[162] employed co-electrodeposition to synthesize Ni–S–$CoFe_2O_4$ supported on Ni foam. Initially, they electrodeposited Ni–S onto the nickel foam, followed by the preparation of $CoFe_2O_4$ using the coprecipitation method. Subsequently, both materials were co-electrodeposited onto the nickel foam to form the complete ternary composite. This resulted in the formation of a flower-like morphology, with crystalline $CoFe_2O_4$ and an amorphous Ni–S layer at the edges, as illustrated in Fig. 12b–d. The composite electrocatalyst demonstrated an overpotential of 228 mV at a current density of 10 mA cm^{-2} when evaluated for its OER activity under alkaline conditions. Another aspect closely related to electrodeposition is the jet-electrodeposition

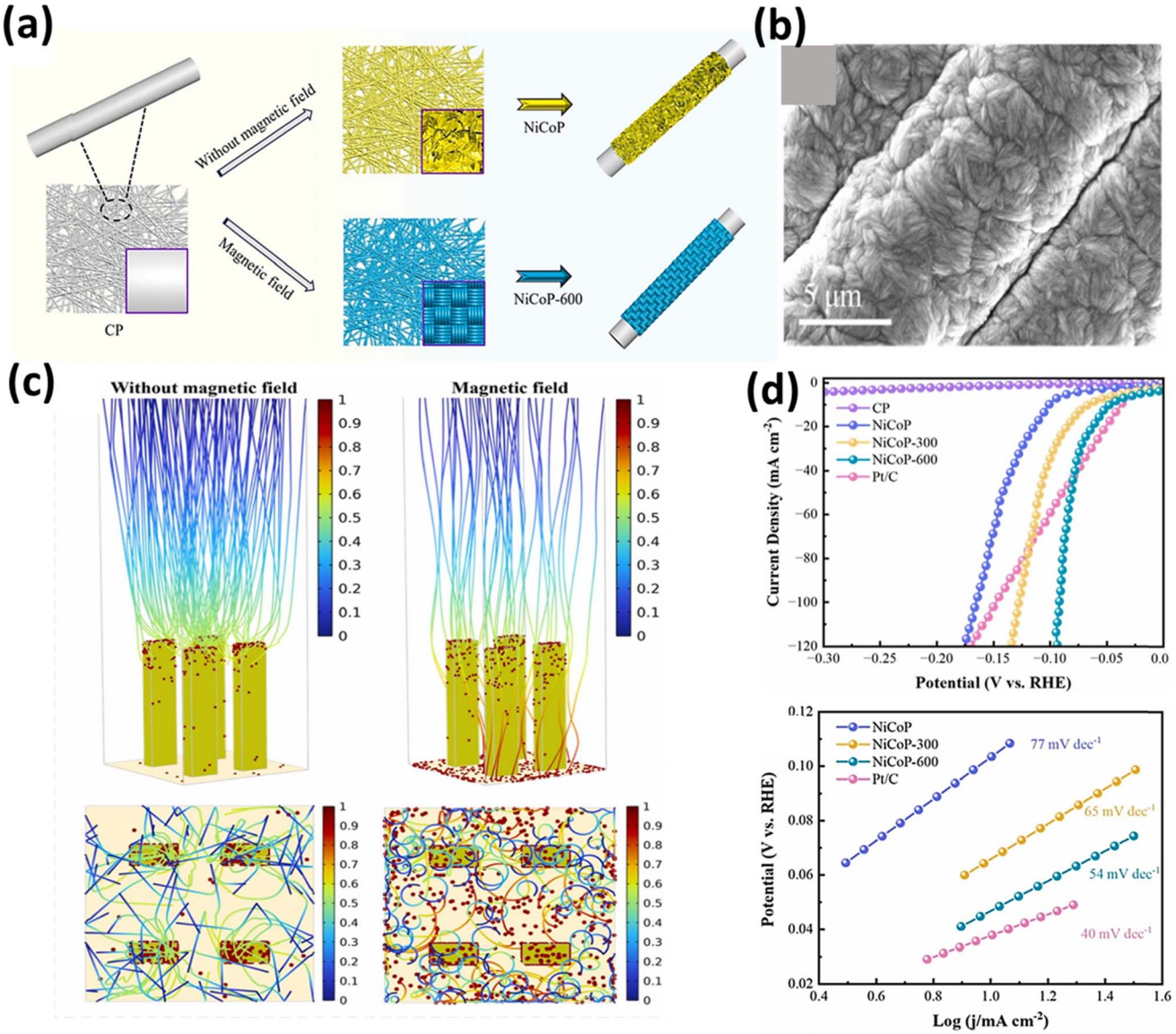

Fig. 11 (a) Schematic of the preparation of NiCoP and NiCoP-600 on carbon, (b) SEM images of NiCoP-600, (c) COMSOL simulation of trajectory distribution of charged particles with and without magnetic field and (d) polarization curves of electrocatalysts (reprinted with permission,[159] copyright 2023, Elsevier).

method. In this method the electrolyte material is sprayed with great force onto the surface of the cathode, which completely relies on the pressure capacity of the pump. This high velocity of electrolyte improves the mass transfer rate of ions on the cathode. The jet electrodeposition technique is much more reliable than the ordinary technique with respect to managing the uniformity, thickness, selective deposition area, and a few more aspects related to electrocatalysis.[164] The use of an external magnetic field in the jet electrodeposition technique is interesting, which has rarely been explored.[165,166] Jiang *et al.*[165] and Jiang *et al.*[166] prepared Ni–Co–MoS_2 and Ni–Co–CeO_2/Ni to study their OER performance as electrocatalysts, respectively. Table 2 summarizes the different techniques employed by researchers for the fabrication of catalysts and the resulting outcomes from their electrochemical analysis.

5. Magnetic field-enhanced electrocatalysis

5.1. Magnetic field-enhanced HER

Water splitting is the leading approach for hydrogen production with minimal environmental impact.[167,168] However, the sluggish kinetics of the HER at the cathode makes it necessary to enhance the efficiency of water splitting.[169] Extensive research has focused on developing or modifying electrocatalysts, particularly non-noble metal-based catalysts such as phosphides, oxides, fluorides, sulfides, selenides, and nitrides due to their improved performance in this process.[19,21,23–25,170] However, despite the advancements, they still fall short of the performance level achieved by noble metal-based electrocatalysts. Notably, the use of external templates has resulted in a lower

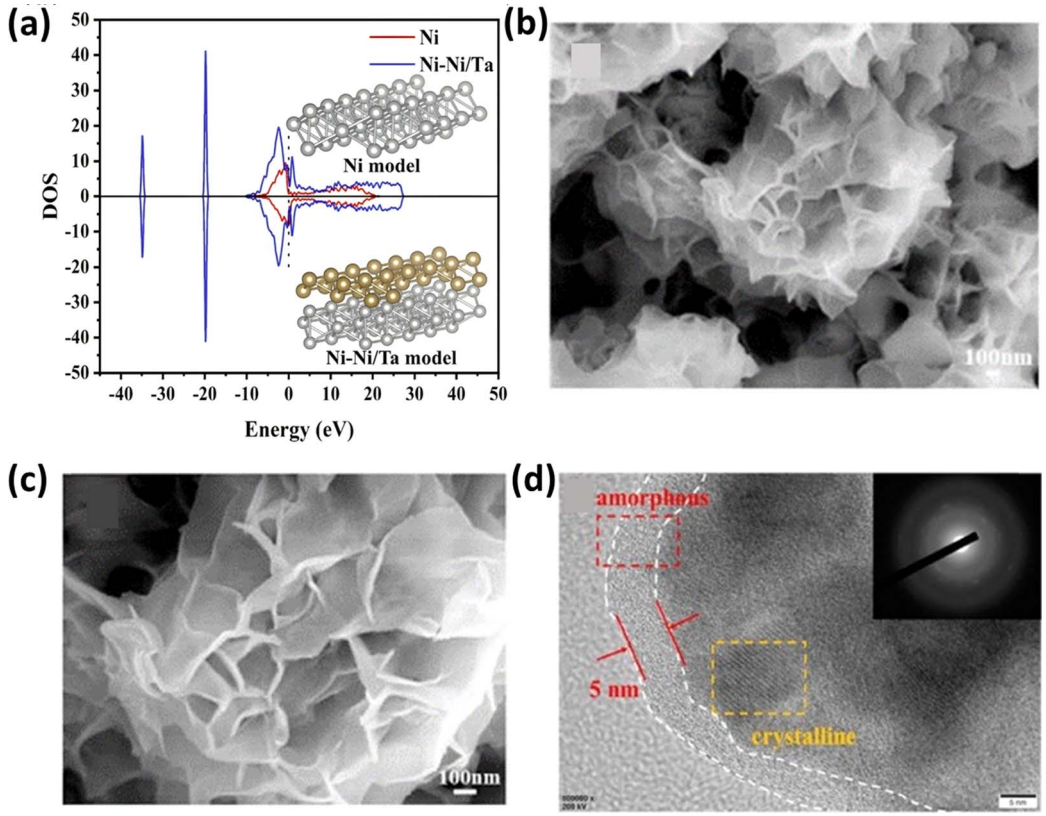

Fig. 12 (a) DOS spectra of Ni–Ni/Ta and Ni models (reprinted with permission,[161] copyright 2023, Elsevier), (b) and (c) SEM images of Ni–S–$CoFe_2O_4$ and (d) HETEM image of magnetized Ni–S–$CoFe_2O_4$ depicting the amorphous and crystalline forms of the electrocatalyst (reprinted with permission,[162] copyright 2020, Elsevier).

overpotential for the HER activity of the catalysts to a certain extent.[171] For instance, a magnetic field has been shown to play a promising role as an external template.

5.1.1. Uniform magnetic field. To investigate the prolonged durability of electrocatalysts, Hou *et al.* synthesized three distinct phosphides based on NiCo as hydrogen catalysts to assess the impact of a magnetic field on the HER.[172] They employed the simple hydrothermal and solvothermal methods for the synthesis of the catalyst, as depicted in Fig. 13a. Notably, the second catalyst, featuring an additional coating of NiCoFe, exhibited a superior performance and stability compared to the first catalyst lacking this coating, which was attributed to the protection effect of the magnetic NiCoFe alloy.[172] It achieved an overpotential of 111 mV at a current density of 10 mA cm^{-2} and

Table 2 Summary of the different techniques employed for the fabrication of catalysts and their electrocatalytic performances

Electrochemical process	Electrocatalyst material	Electrode fabrication procedure in MF	Overpotential@10 mA cm^{-2} (mV)	Ref.
HER	MoO_2	MIH	39	139
OER	NiFe LDH	MIH	246	139
OER	NiFe	MIHRQ	260 (@100 mA cm^{-2})	140
OER	Co/C	MIH	308	141
HER	$Mo_3S_7Cl_y$	MIH	184	145
HER	Ru	MIH	23 (acidic) 12 (alkaline medium)	142
HER	CuNi	Electrodeposition	38	157
HER	Ni	Electrodeposition	231	158
HER	NiCoP	Electrodeposition	48 (alkaline) 34 (acidic medium)	159
OER	NiCoP–Fe_3O_4	Electrodeposition	256	160
OER	Ni–Ni/Ta	Electrodeposition	256	161
HER	MoS_{2-x}–Pd	Electrodeposition	—	163
OER	Ni–S–$CoFe_2O_4$	Electrodeposition	228	162
OER	MoS_2/Ni	Jet electrodeposition	227	165
OER	$NiCoCeO_2$/Ni	Jet electrodeposition	301	166

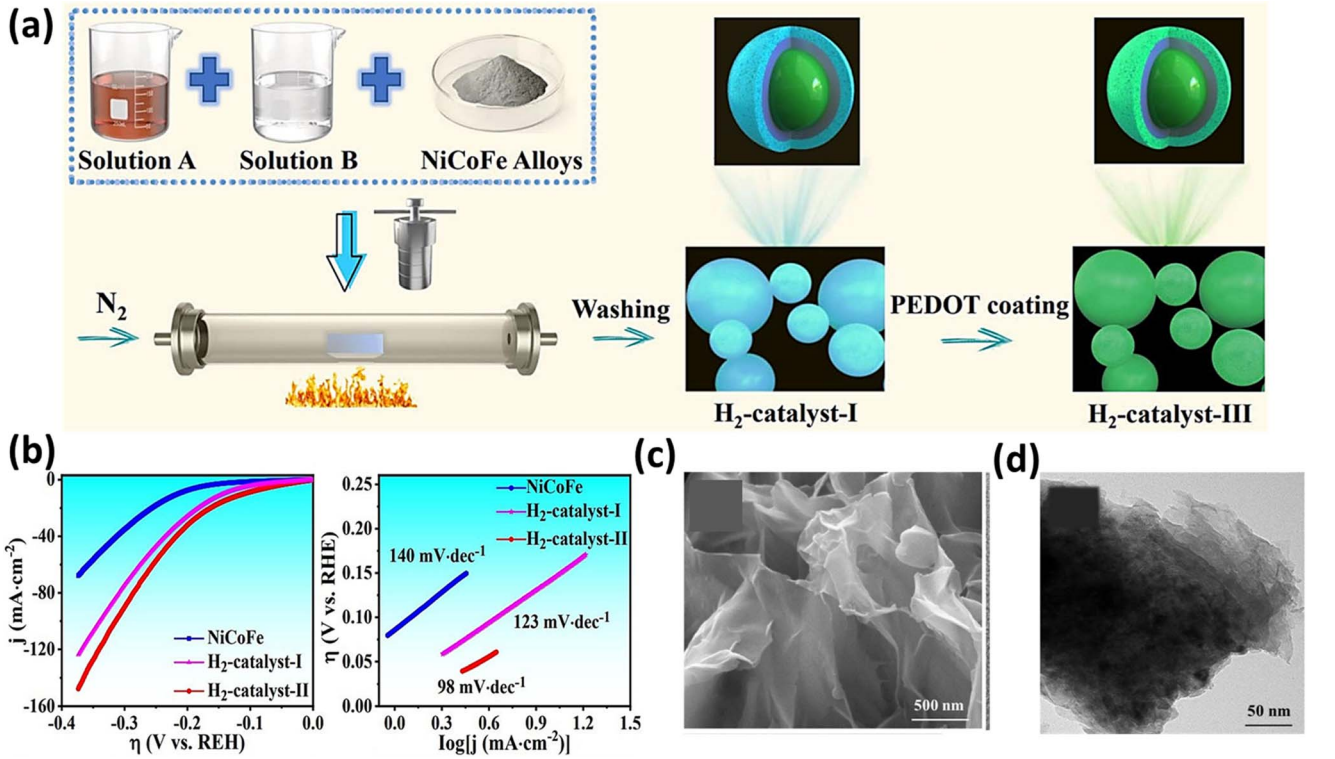

Fig. 13 (a) Schematic of the synthesis of NiCoFe electrocatalysts and (b) LSV and Tafel slope of the NiCoFe electrocatalysts (reprinted with permission,[172] copyright 2023, Elsevier). (c) and (d) SEM and HRTEM images of $NiCo_2S_4$ (reprinted with permission,[173] copyright 2023, Elsevier).

a Tafel slope of 98 mV dec^{-1}, as illustrated in Fig. 13b. Intriguingly, the third catalyst, externally coated with PEDOT polymer, demonstrated functionality for a duration of 11 days. In a comparable method aimed at investigating the HER performance of $NiCo_2S_4$ hybrids featuring a two-dimensional nanosheet morphology (as depicted in Fig. 13c and d) derived from Ni-MOF, Xu *et al.* achieved an overpotential of 104 mV at a current density of 10 mA cm^{-2}.[173] Additionally, they obtained a low Tafel slope value of 54 mV dec^{-1}. This group explained that the appreciable decrease in the overpotential in the presence of a magnetic field is because of the Lorentz force developed in the system, which sped up the charge transport and reduced the thickness of the diffusion layer, which agrees with the lower R_{ct} values obtained in EIS.

Achieving an appropriate structure conducive to electron movement between electrodes is a compelling objective. In this case, Zhou *et al.*[174] utilized chemical vapor deposition to fabricate flakes with a bowl-like morphology of MoS_2, as illustrated in Fig. 14a. To induce this structure, the SiO_2/Si substrate was tilted during the deposition process, and the resulting structure was confirmed by calculating the height difference using AFM images, revealing the variations between the central and ring regions. Further investigations revealed the unsaturation of the edge Mo atoms, endowing the material with magnetic properties. Additionally, the ferromagnetic bowl-like structure of the MoS_2 flakes was found to facilitate interlayer electron transfer from the glassy carbon electrode to the active sites of the catalyst in the presence of an external vertical magnetic field, as depicted in Fig. 14b. Further, this magnetic behaviour subsequently enhanced the HER activity of the electrocatalyst, as evidenced in Fig. 14c and d. In another endeavour to fabricate a Heusler alloy containing metals such as Ni, Mn, and In, Chen *et al.*[175] employed the pulsed laser deposition technique, as illustrated in Fig. 14e. These researchers effectively synthesized flakes of $Ni_{43}Mn_{32}In_{25}$, utilizing them as an electrocatalyst coated on Ni foam. Remarkably, they observed a 4.9% and 2.4% decrease in overpotential value at 10 mA cm^{-2} current density when the external magnetic field was applied in the perpendicular and parallel directions to the electrode surface, respectively. Employing another method, Li *et al.*[176] created single-crystal multi-metal catalysts such as ferromagnetic Co_2VGa, Co_2MnGa, and ferrimagnetic Mn_2CoGa to investigate their performance in the HER both with and without an external magnetic field. Another previous approach to synthesize an Ni–W alloy and the effect of a magnetic field on its HER activity and the possible magnetic field effect were studied by Elias *et al.*[177] They inferred that the Lorentz force generated due to a magnetic field could be the possible cause for the observed enhancement in HER activity.

5.1.2. Alternating magnetic field. The utilization of an alternating magnetic field (AMF) presents an alternative avenue for exerting greater control of the properties of electrocatalytic materials, such as improved mixing, externally regulated heating, and modulation of surface reactions. Overall, an AMF holds promise for heightened control, efficacy, and specificity compared to a uniform magnetic field.

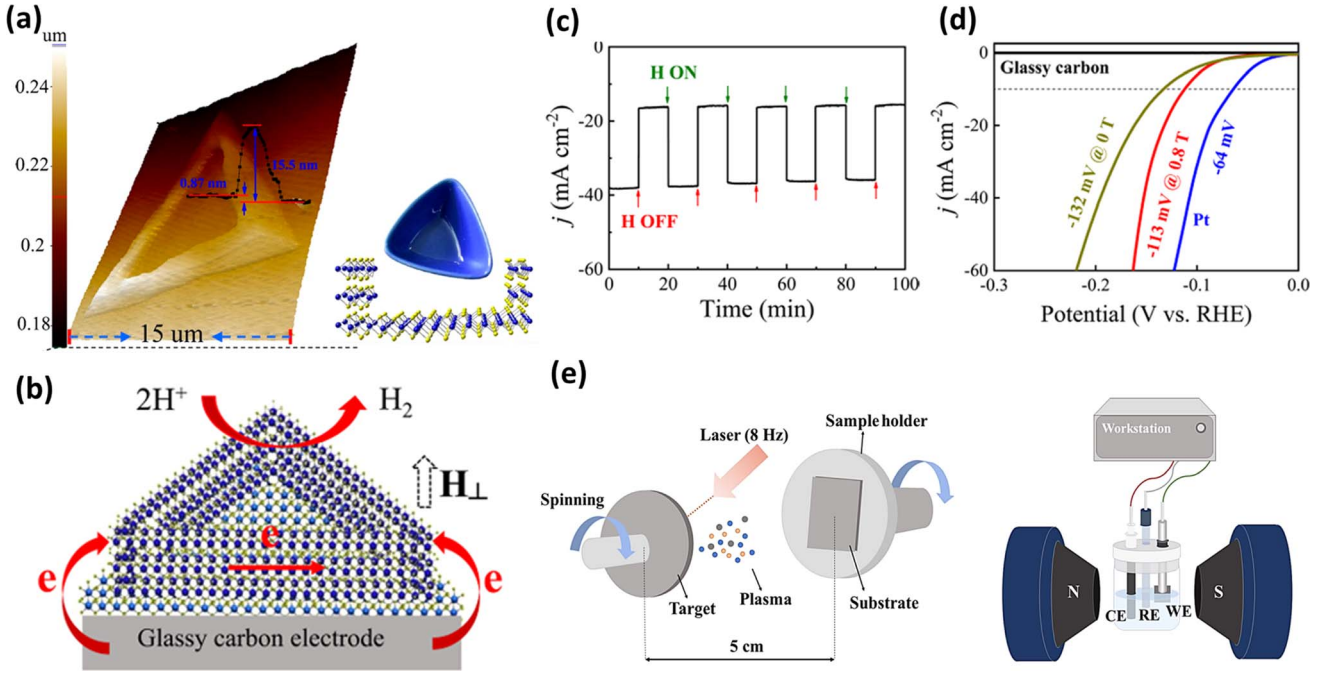

Fig. 14 (a) 3D AFM image representing the height and schematic of the bowl-like structure of MoS_2, (b) schematic of the electron transfer in the MoS_2 flakes, (c) chronoamperometric response to the pulse on and off of a magnetic field, (d) polarization curve for HER with MoS_2 flakes in the presence and absence of a magnetic field (reprinted with permission,[174] copyright 2020, the American Chemical Society) and (e) schematic of pulsed laser electrodeposition technique and the device setup for electrochemical analysis (reprinted with permission,[175] copyright 2021, Elsevier).

It is notable that transition metal dichalcogenides (TMDCs) have been extensively investigated as support materials for dispersing single atoms in the preparation of single-atom catalysts, owing to their ability to provide high specific surface areas.[178,179] Following a similar approach, Zeng *et al.*[180] synthesized Gd single-atom catalysts supported on MoS_2 using laser beam epitaxy, as illustrated in Fig. 15a, to evaluate their HER activity. This group employed theoretical calculations to analyse the total density of states (TDOS) of Gd@MoS_2, as shown in Fig. 15b, revealing an asymmetry between the spin up and spin down states near the Fermi level. This was attributed to the strong hybridization between the three elements, where the catalytic activity of the material would increase as the Fermi level of the material is closer to the valence band, suggesting rapid electron transfer during catalysis.[180] Of particular interest is the utilization of AMF to thermally activate the single atoms, subsequently serving as active catalytic sites, as depicted in Fig. 15c. This approach substantially enhanced the HER activity, reducing the overpotential from 160 mV cm^{-2} to 57 mV cm^{-2} in the absence and presence of an AMF, respectively. The layered configurations inherent in 3D architectures, where the successive stacking of 2D layers occurs, theoretically augment their surface area. However, a drawback arises from the interlayer potential barrier, hindering electron mobility to the active sites.[182] Thus, to overcome this challenge, Su *et al.*[181] devised a novel screw pyramid structure for MoS_2, distinct from the conventional step pyramid structure. Remarkably, when evaluated for its HER performance, the screw pyramid exhibited a notable difference in activity with and without the application of an AMF. This disparity can be attributed to the generation of micro eddy currents induced by the AMF, which traversed between the layers, facilitating the electron mobility, and consequently enhancing the catalytic efficiency (Fig. 15d and e). The theoretical studies explained that the micro eddy current developed in the screw model is over one order of magnitude higher than that developed in the step model. This group also investigated the magnetic field effect for a single-layer MoS_2 catalyst and found that the enhancement is much less given that the developed micro eddy currents are very low in magnitude.

Another factor to consider with ultra-small magnetic nanoparticles under an AMF is Néel relaxation, which describes the phenomenon wherein magnetic domains within nanoparticles realign or undergo spin flipping to align with the external magnetic field.[185] In a related investigation, Huang *et al.*[183] fabricated electrocatalysts incorporating $NiSe_2$ and $NiSe_{2-x}$ nanoparticles. When subjected to an AMF, these nanoparticles experienced magnetic heating due to Néel relaxation, and this localized heating under an AMF improved the intrinsic catalytic activity of $NiSe_{2-x}$, thereby resulting in an enhanced HER performance, as illustrated in Fig. 16a and b. In a separate investigation, Cai *et al.*[184] evaluated the efficacy of an Fe–Co–Ni–P–B magnetic catalyst for the HER. This team identified Lorentz force as a factor contributing to the increased HER activity under an AMF. They proposed that the alternating Lorentz force induced by the AMF can lead to a reduction in charge transfer

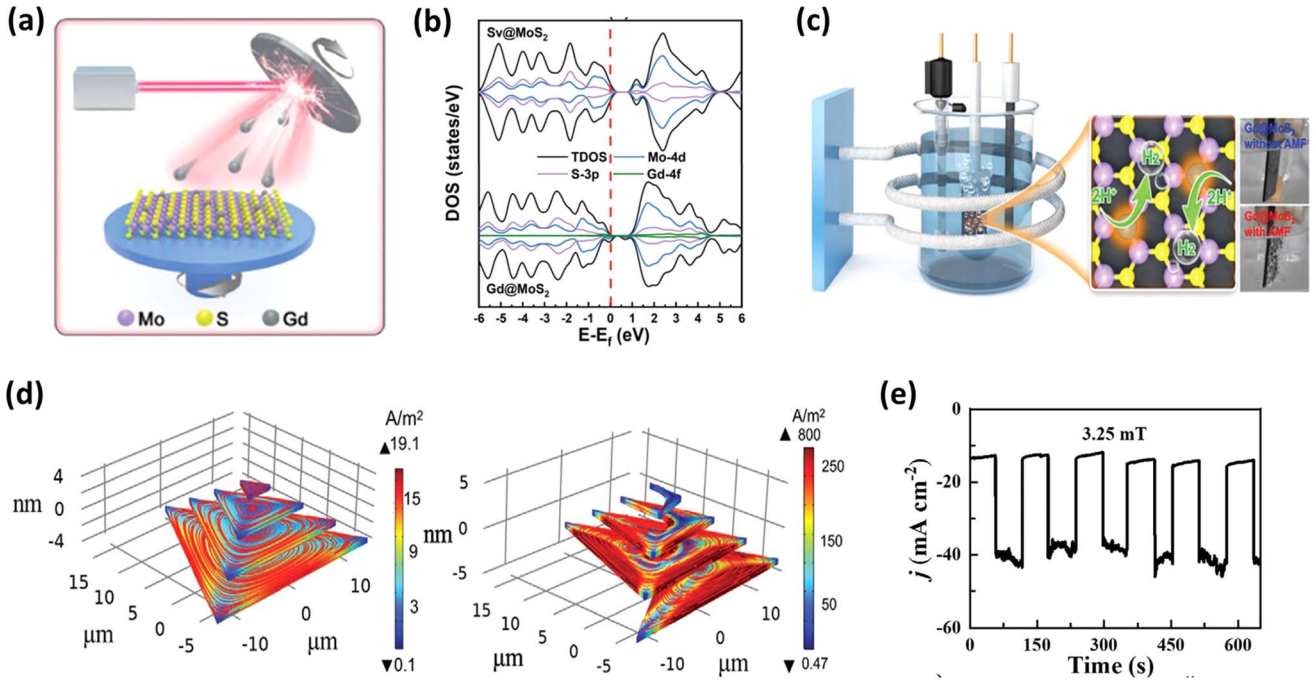

Fig. 15 (a) Schematic of laser molecular beam epitaxy to prepare Gd@MoS_2, (b) DOS spectra of Gd@MoS_2 and Sv@MoS_2, and (c) schematic of AMF-assisted electrochemical setup for HER analysis (reprinted with permission,[180] copyright 2022, Wiley). (d) Simulated Eddy current density of step and screw pyramid MoS_2 and (e) response of screw pyramid to AMF stimulation in HER (reprinted with permission,[181] copyright 2022, Wiley).

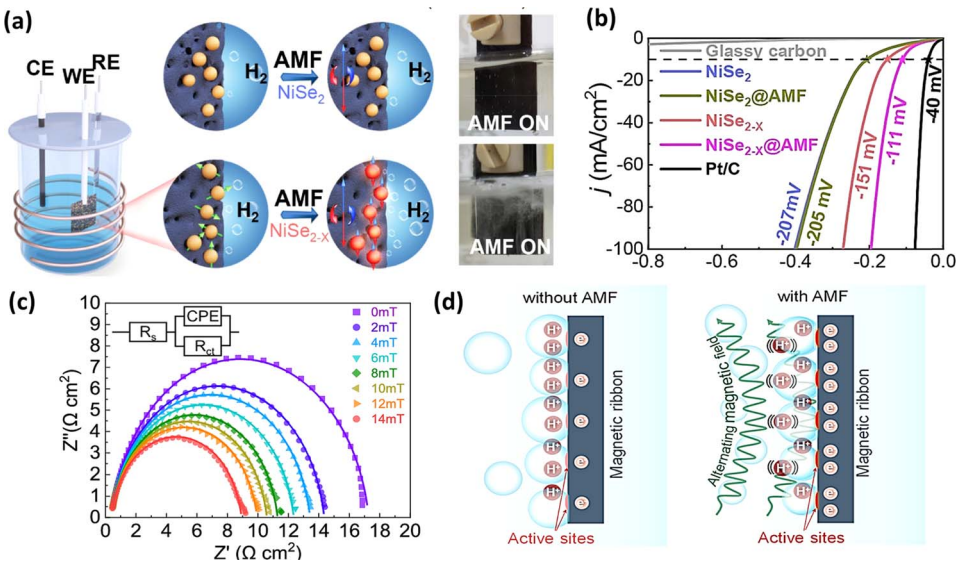

Fig. 16 (a) Schematic and real-time pictures of $NiSe_2$ and $NiSe_{2-x}$ nanoparticles under AMF stimulation and (b) LSV curves of above-mentioned electrocatalysts in the presence and absence of an AMF (reprinted with permission,[183] copyright 2022, Elsevier). (c) EIS Nyquist curves under different AMF strengths of Fe–Co–Ni–P–B electrocatalyst and (d) schematic illustration of the role of AMF in facilitating bubble desorption (reprinted with permission,[184] copyright 2022, the American Chemical Society).

resistance, as shown in Fig. 16c, and also influence the formation of a dense layer on the active sites of the electrode, facilitating easier hydrogen evolution from the electrode surface, as depicted in Fig. 16d. In another attempt to increase the HER activity of nickel-coated iron carbide electrocatalysts, Niether *et al.*[186] decreased the overpotential for the HER by 100 mV at a current density of 20 mA cm^{-2}. Table 3 summarizes the different electrocatalyst materials used under different magnetic field strengths and their corresponding electrocatalytic parameters in the presence and absence of a magnetic field.

Table 3 Summary of the different HER electrocatalysts used under a magnetic field of varying strengths

Nanomaterial	Employed MF	HER parameter without MF	HER parameter with MF	Ref.
NiCoFe based material	Uniform MF	—	η_{10} = 106 mV Durability = 11 days	172
$NiCo_2S_4$	100 mT	η_{10} = 161 mV	η_{10} = 104 mV	173
MoS_2	0.8 T	η_{10} = 132 mV b = 79 mV dec^{-1}	η_{10} = 113 mV b = 59 mV dec^{-1}	174
$Ni_{43}Mn_{32}In_{25}$	0.8 T	η_{10} = 189.4 mV	η_{10} = 181.4 mV J increased by 10% at constant overpotential	175
Ni–W	0 to 0.4 T	—	—	177
Gd@MoS_2	3.9 mT	η_{10} = 160 mV b = 95 mV dec^{-1}	η_{10} = 57 mV b = 50 mV dec^{-1}	180
MoS_2 (screw shape)	3.25 mT	η_{10} = 177 mV b = 74 mV dec^{-1}	η_{10} = 105 mV b = 45 mV dec^{-1}	181
$NiSe_{2-x}$	AMF	η_{10} = 151 mV b = 97.74 mV dec^{-1}	η_{10} = 111 mV b = 70.92 mv dec^{-1}	183
Fe–Co–Ni–P–B	20 mT	η_{10} = 388.89 mV b = 87.5 mV dec^{-1}	η_{10} = 350 mV b = 82.8 mV dec^{-1}	184
FeC–Ni	—	—	η_{20} = decreases by 100 mV	186

5.2. Magnetic field-enhanced OER

Electrolyzing water involves the liberation of oxygen at the anode, a process known as the OER. Theoretically, a potential difference of 1.23 V across the electrodes is required to initiate this reaction.[187] However, practical applications demand a significantly higher voltage due to the overpotential. The OER is particularly intricate, involving the transfer of four electrons through a multistep process, as outlined in previous discussions.[188] Besides its complexity, challenges such as short lifespan, suboptimal energy conversion, slow kinetics, and limited stability have spurred researchers to explore alternative and efficient approaches.[189–191] Among them, the utilization of an external magnetic field as a template to enhance the efficiency is elaborated in the subsequent sections.

5.2.1. Uniform magnetic field. One of the primary effects of an external magnetic field during electrocatalysis is the Lorentz interaction and localized magnetic heating, which have been investigated and validated as contributors to enhancing the OER performance of electrocatalysts.[184] Following a similar approach, Deng *et al.*[192] investigated the performance of $Cr_2Ge_2Te_6$ in both its bulk and exfoliated nanosheet forms, with the latter studied under the influence of an external magnetic field. Fig. 17a and b illustrate images of the bulk material and nanosheets, respectively. Interestingly, this group observed a significant reduction in the electrocatalytic parameters, with the lowest values recorded when the $Cr_2Ge_2Te_6$ nanosheets were evaluated under a magnetic field, as depicted in Fig. 17c and d. According to the thorough evaluation of the EIS spectra and ECSA of the nanosheets, it is evident that the Lorentz force and local magnetic heating are the two mechanisms responsible for the enhancement in activity. In an alternative approach aimed at harnessing the Lorentz force and exploiting the reversible valence state transitions of cobalt atoms in the presence of an external magnetic field, Wang *et al.*[193] utilized the sol–gel method to synthesize $LaCoO_3$ (perovskite) products. Subsequently, they were reduced with EDA under an inert atmosphere, lasting 1 to 6 days, and the samples were denoted as LCO-X (X = 1 to 6). The alkyl amine processing method generated lattice oxygen vacancies, prompting the transition of the Co ions from the Co^{3+} to Co^{2+} state, enhancing the adsorption of the oxygen intermediate, as shown in Fig. 17e. Interestingly, the OER overpotential initially decreased, and then increased, as shown in the volcano plot (Fig. 17f). Notably, the LCO-5 electrocatalyst, exhibiting a superior performance, was evaluated under an external magnetic field. The OER catalytic performance of perovskite oxides strongly depends on the electron configuration (e_g) of the transition metal. The optimal electron configuration of $e_g \sim 1.2$ promoted the effective adsorption of oxygen-containing groups. The external magnetic field enhanced this by inducing electron transitions in the cobalt ions from the low spin to high spin states, resulting in more unpaired electrons in the 3d orbit of Co and increasing the spin polarization, thereby resulting in a 20 mV decrease in overpotential. In another study on perovskites, Sharma *et al.*[194] utilized a co-precipitation method to synthesize $YMnO_3$ and $YMn_{1-x}Cr_xO_3$. The characterization confirmed the successful doping of Cr, as evident in the SEM images and Raman spectra, showing an increase in the number of particles and orthorhombic B_{2g} modes together with pristine hexagonal modes, respectively, which were attributed to the Jahn–Teller symmetry of the in-phase O_2 stretching mode[194] (Fig. 17g and h), respectively. The evaluation of the Cr-doped materials for their OER performance revealed that $YMn_{1-x}Cr_xO_3$ (x = 0.1) exhibited the optimal parameters in the presence of a magnetic field, which was attributed to the enhanced ferromagnetic exchange interaction post Cr-doping.

Sun *et al.*[195] investigated NiFe-LDH catalysts, finding that their modulation by incorporating Cu^{2+} can alter the Fe^{III} spin states, as illustrated in Fig. 18a. Specifically, the introduction of Cu^{2+} induced repulsion between the electrons in Ni^{2+}/Cu^{2+} and O^{2-}, while enhancing the O–Fe–O pi-donation, facilitating electron transfer. The incorporation of Cu in the lattice also caused the transformation of NiFe-LDHs from ferrimagnets to

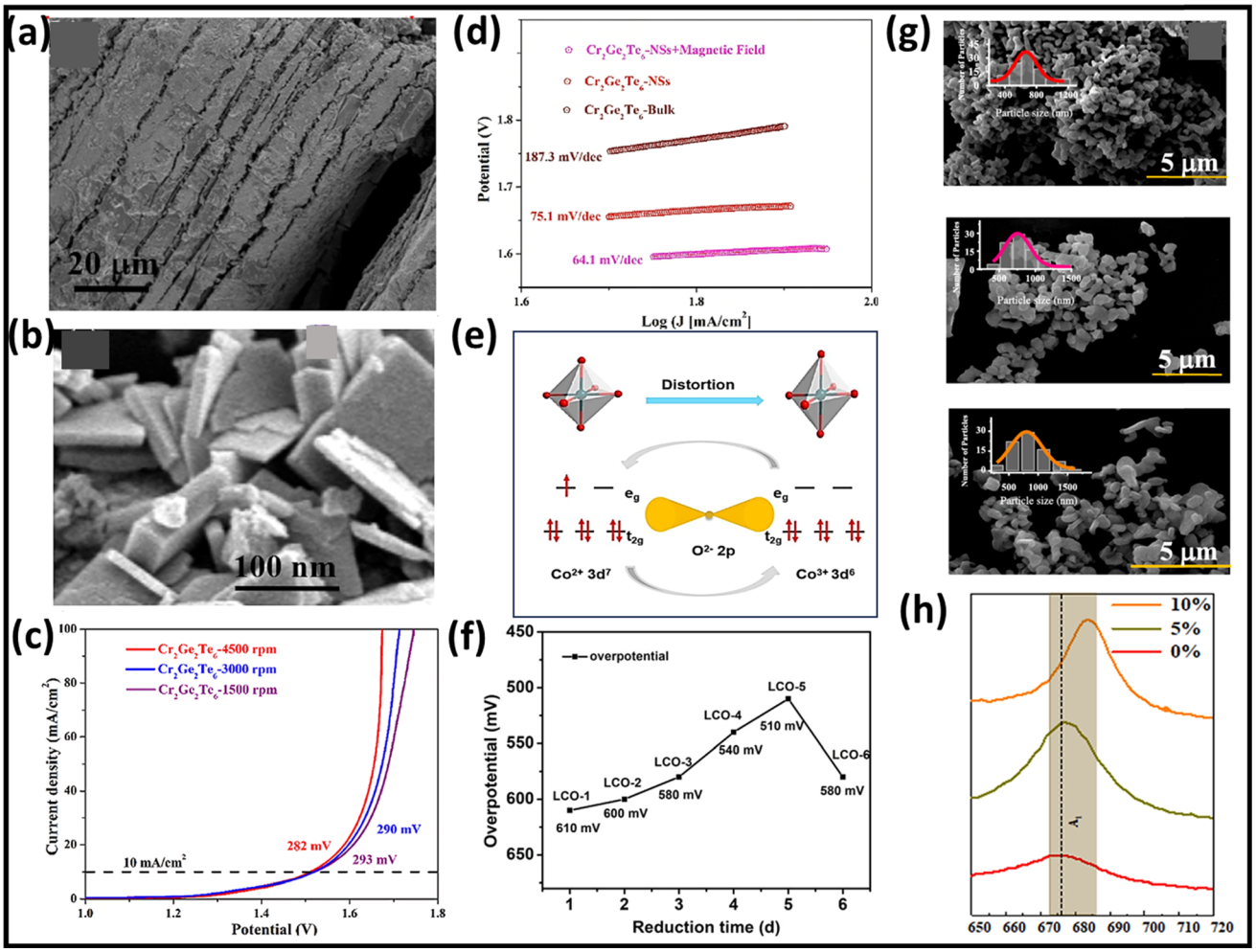

Fig. 17 (a) and (b) SEM images of bulk and nanosheets of $Cr_2Ge_2Te_6$, respectively, and (c) and (d) LSV and Tafel slopes of $Cr_2Ge_2Te_6$ nanosheets at different centrifugal rates (reprinted with permission,[192] copyright 2023, Elsevier). (e) Schematic of the structure distortion and valence transition of Co ions induced by O_2 vacancies and (f) overpotentials of LCO-*X* samples (reprinted with permission,[193] copyright 2022, Chemistry Europe). (g) SEM images of $YMn_{1-x}Cr_xO_3$ ($x = 0$, $x = 0.05$ and $x = 0.1$) and (h) magnified Raman shift of $YMn_{1-x}Cr_xO_3$ (reprinted with permission,[194] copyright 2023, the American Chemical Society).

ferromagnets and enhanced the OER activity of Cu–NiFe–LDH compared with that of NiFe–LDH, offering a low overpotential of about 180 mV at 10 mA cm^{-2}. Lyu *et al.*[196] demonstrated the manipulation of the ion geometrical sites within symmetry sites. Their study examined $NiFe_2O_4$ (NFO) catalysts, initially with Ni^{2+} located in the O_h sites, which under a strong magnetic field, shifted to the more active T_d sites, as shown in Fig. 18b, and the Fe cations shifted from the T_d sites to the O_h sites. Consequently, the enhanced quantity of Ni^{2+} in the T_d sites favoured an increase in OER activity. The analysis of the activity of the structurally reconstructed catalyst showed a twofold increase in current density. This group suggested that together with spin polarization, the structural reconstruction of the electrocatalyst under a magnetic field favoured the enhancement in activity. As discussed in the previous sections, the magnetic moments of electrocatalytic materials, if present, align with the external magnetic field, the enhancing their catalytic performance. Additionally, an external field offers other benefits during electrocatalysis, such as the magnetohydrodynamic effect, improved charge transfer at the electrode–electrolyte interface and spin polarization effect. Similarly, Qin *et al.*[198] synthesized layered double hydroxides based on NiFe to investigate the potential enhancements in electrocatalyst performance under an external magnetic field. Their study revealed that the optimal overpotential for OER occurred at a magnetic field strength of 200 mT. They proposed that mechanisms such as the magnetohydrodynamic effect, charge transfer, and magnetic moment alignment contribute to this improved efficiency, which are in good agreement with in the increase in C_{dl} values (1.5 times higher than that in the absence of a magnetic field) and decrease in the R_{ct} values. To investigate the impact of transition metal oxides on OER, Li *et al.*[197] coated Co_3O_4 on Ni foam and observed significant outcomes. The urchin-like structure of Co_3O_4 notably boosted the surface area (Fig. 18c and d). Additionally, the authors proposed that the presence of a magnetic field induced a reciprocal

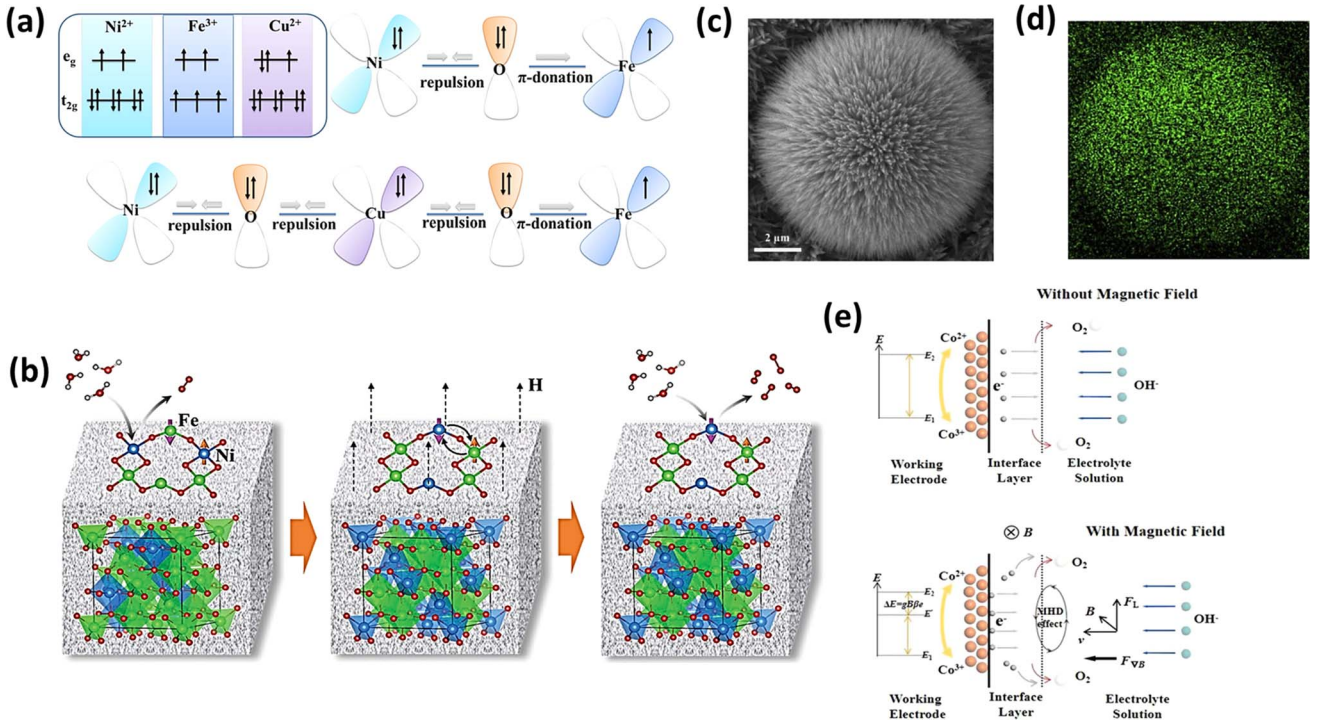

Fig. 18 (a) Schematic of the electronic interaction in the d_{xy} orbitals of NiFe-LDH and Cu–NiFe–LDH (reprinted with permission,[195] copyright 2022, the American Chemical Society). (b) Schematic showing the increase in concentration of Ni^{3+} at the T_d sites (reprinted with permission,[196] copyright 2022, Wiley). (c) and (d) SEM image and elemental mapping of Co_3O_4, respectively, and (e) mechanistic illustration of magnetic field-enhanced OER activity of Co_3O_4 (reprinted with permission,[197] copyright 2019, Elsevier).

transformational effect between Co^{2+} and Co^{3+}. The magnetic field causes energy level splitting, as illustrated in Fig. 18e, enhancing the spin states of $Co^{2+/3+}$, and thereby reducing the activation energy required for charge transitions.[197] The authors also emphasized the crucial role of magnetohydrodynamic effects, which enhanced the OER parameters, resulting in a minimum overpotential of 252 mV and a Tafel slope of 26.7 mV dec^{-1} under a magnetic field strength of 125 mT.

Enhancing the OER activity by improving the spin-related kinetics, typically induced by ferromagnetic spin ordering of nanoparticles, is a crucial and beneficial technique in electrocatalysis. For example, Chen *et al.*[199] employed pulsed laser deposition to uniformly deposit the 1T phase of ferromagnetic VSe_2 nanoparticles onto an amorphous carbon matrix, as illustrated in Fig. 19a. Upon testing the material for its OER activity, a notable enhancement was observed, which was primarily attributed to the improvement in the spin-related kinetics. To theoretically confirm the enhancement in OER performance, the researchers conducted DFT calculations, revealing that in the presence of a magnetic field, the energy band of VSe_2 tends to shift closer to the Fermi level, as seen in Fig. 19b, indicating improved electron transfer activity. This was also supported by the observed reduction in the R_{ct} value (Fig. 19c). Ultimately, this group achieved a low overpotential value of 228 mV at a current density of 10 mA cm^{-2} with a magnetic strength of 800 mT. Ren *et al.*[122] achieved control of the spin-polarized electrons in a ferromagnetic electrocatalyst using a magnetic field, promoting the generation of triatomic O_2 molecules and effectively enhancing its OER efficiency. They elucidated the spin-polarized kinetics, suggesting that the reduction in the Tafel slope value indicates a change in the underlying reaction mechanism. In their approach, the decrease in the Tafel slope value from 109 mV dec^{-1} to 87.8 mV dec^{-1} suggested a reduction in the electron transfer in the rate-determining step to 0.5, followed by subsequent steps. Fig. 19d indicates that as the reaction temperature increased, the Tafel slope value tended to decrease both in the presence and absence of a magnetic field. However, it is noteworthy that beyond a certain increase in temperature, the magnetic moments of the ferromagnetic catalyst became thermally disturbed, leading to demagnetization, and consequently an increase in the Tafel slope value. Zhang *et al.*[200] investigated the OER capabilities of nickel-based electrocatalysts, namely $Ni(OH)_2$, NiO, and pure nickel (Ni), as depicted in Fig. 19e. The researchers performed OER assessments under an *in situ* magnetic field, adjusting the magnetic intensity from 0 to 1.4 T using a vibrating sample magnetometer. Their findings indicated a 20 mV decrease in overpotential for nickel when exposed to a magnetic field strength of 1.4 T. Liu *et al.*[201] used the technique of arc melting, followed by annealing to obtain FeCo alloys with different compositions. After the analysis of the electrocatalysts for their OER activity, this group identified a 12 mV decrease in overpotential value at a current density of 20 mA cm^{-2} under the influence of an external magnetic field.

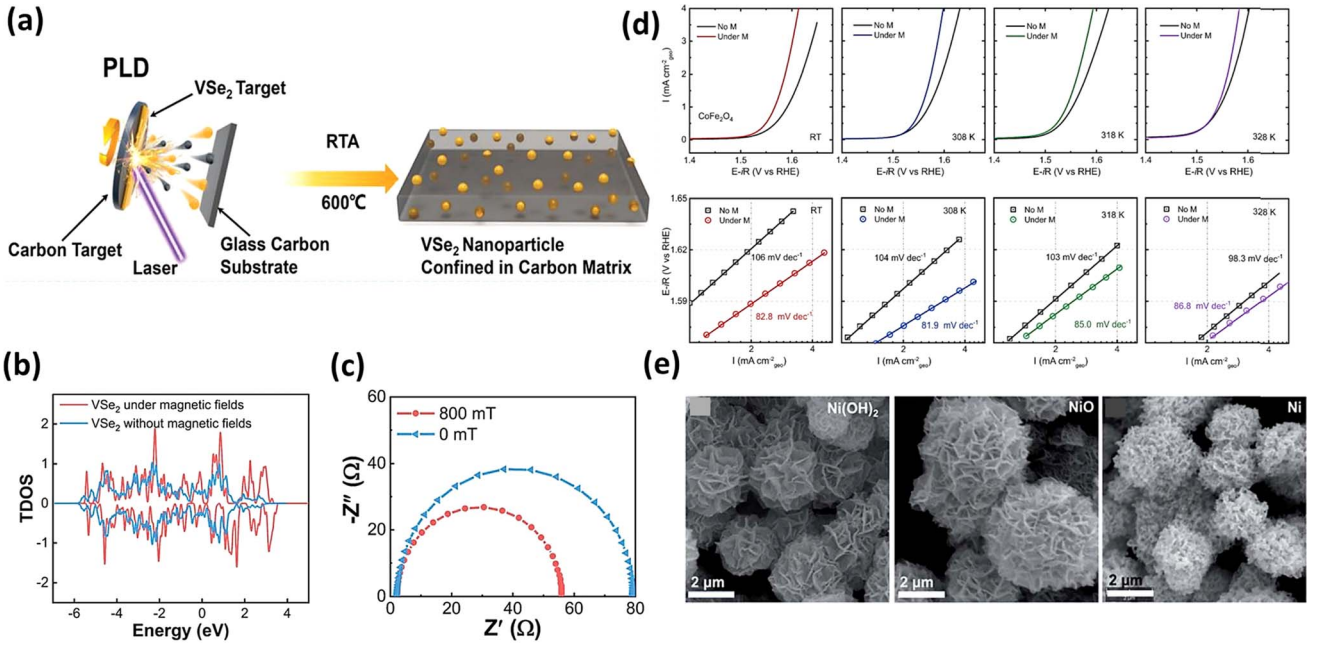

Fig. 19 (a) Schematic illustration of the synthesis of VSe_2 through pulsed laser deposition, (b) TDOS spectra of VSe_2 and (c) Nyquist plots of VSe_2 under a magnetic field of 0 and 800 mT (reprinted with permission,[199] copyright 2023, Wiley). (d) LSV curves and Tafel plots of $CoFe_2O_4$ at different temperatures (reprinted with permission,[122] copyrights 2021, *Nature Communications*) and (e) SEM images of $Ni(OH)_2$, NiO and Ni (reprinted with permission,[200] copyright 2022, the Royal Society of Chemistry).

5.2.2. Alternating magnetic field & alternating current magnetic field. As discussed previously, although an AMF offers advantages such as precise control and efficacy, there are challenges associated with its use, including the need for sophisticated equipment design and user-friendly operation. However, despite the advantages and disadvantages of various methods, researchers have gained valuable experience in employing these techniques to advance their expertise. For example, Peng *et al.*[202] utilized pulsed laser deposition, followed by rapid thermal annealing to synthesize NiFe nanoparticles embedded within a carbon matrix. Subsequently, electrochemical reconstruction was employed to produce NiFe catalysts encapsulated in an NiFeOOH core–shell structure at the nanoparticle level, as illustrated in Fig. 20a. When these reconstructed nanoparticles were used as electrocatalysts for the OER under an AMF of 3.90 mT, they successfully reduced the overpotential from 342.2 mV (obtained in the absence of an AMF) to 209.2 mV for a current density of 10 mA cm^{-2}, as shown in Fig. 20b and c. This group attributed the improvement to the Néel relaxation, which involves heating caused by magnetic flip alignment with the external AMF direction. In a similar procedure, Ding *et al.*[203] employed the PLD technique, followed by RTA to create a confined structure comprised of $CoSe_2$ embedded in a carbon matrix. They observed the magnetic heating effect with Néel relaxation in the superparamagnetic $CoSe_2$ electrocatalyst, which promoted the rapid evolution of gas from the electrode surface, as illustrated in Fig. 20d and e. The team noted a reduction in overpotential in the presence of an AMF (4.1 mT) from 296 mV (without AMF) to 239 mV at a current density of 10 mA cm^{-2}.

Chen *et al.*[204] synthesized a bimetallic metal–organic framework ($Co_{0.4}Ni_{0.6}$MOF-74) using a simple solvothermal method to investigate the interaction of Ni with another metal and MOF. The resulting material displayed an intricate flower-like structure, as illustrated in Fig. 21a, boasting an increased surface area of 905 m^2 g^{-1} according to the BET measurements. Notably, when assessing the OER activity of the catalyst under the influence of an alternating current magnetic field (ACMF), as depicted in Fig. 21b, they noted a significant 36% decrease in the overpotential value compared to the tests conducted without ACMF. One of the reasons attributed to the enhancement is the uneven surface of the electrode, which may possibly lead to the distortion of the electric field, thereby resulting in local convection near the surface of electrode. Generally, this is generally the micro-MHD effect, which effectively accelerates the flow of gaseous products to reduce the contact resistance, ultimately improving the utilization of the catalytic active sites. In a related investigation involving a trimetallic MOF (NiCoFe–MOF-74), Zheng *et al.*[205] synthesized various samples by adjusting the molar ratios of metallic precursors through a straightforward procedure, as illustrated in Fig. 21c. Intriguing patterns emerged in the performance of this catalyst towards the OER (measured with the catalyst exhibiting the best performance in the absence of AMF). The overpotential values remained steady at a lower potential range with an increase in the ACMF strength, then either gradually decreased (at low current densities) or increased (at high current densities) as the potential range expanded, as depicted in Fig. 21d and e. This anomalous trend is ascribed to the generation of vortex electric currents within the system, in accordance with Faraday's law of

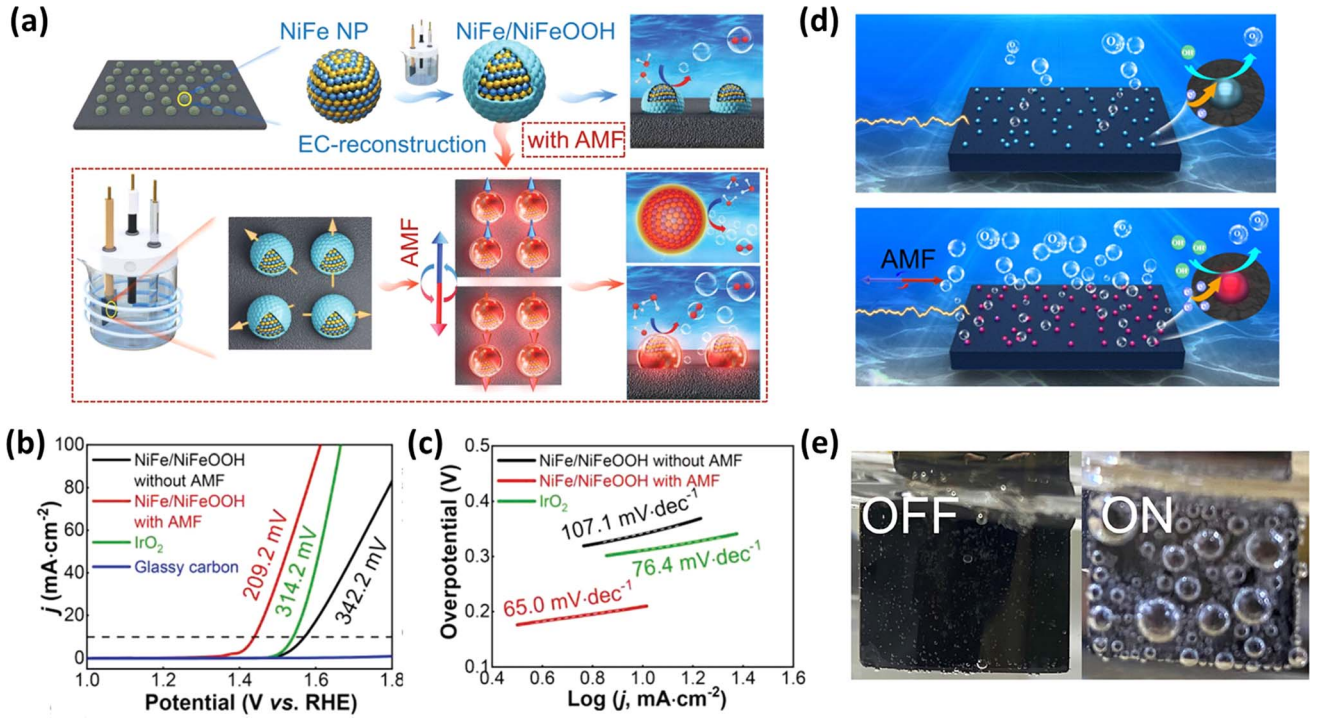

Fig. 20 (a) Schematic representation of EC-reconstructed NiFe and AMF-based magnetic heating and (b) and (c) LSV and Tafel plots of NiFe/NiFeOOH in the presence and absence of AMF (reprinted with permission,[202] copyright 2023, Wiley). (d) Schematic of OER performance of $CoSe_2$ before and during the application of an AMF and (e) real-time pictures of electrode before and during AMF application (reprinted with permission,[203] copyright 2022, *Applied Physics Letters*).

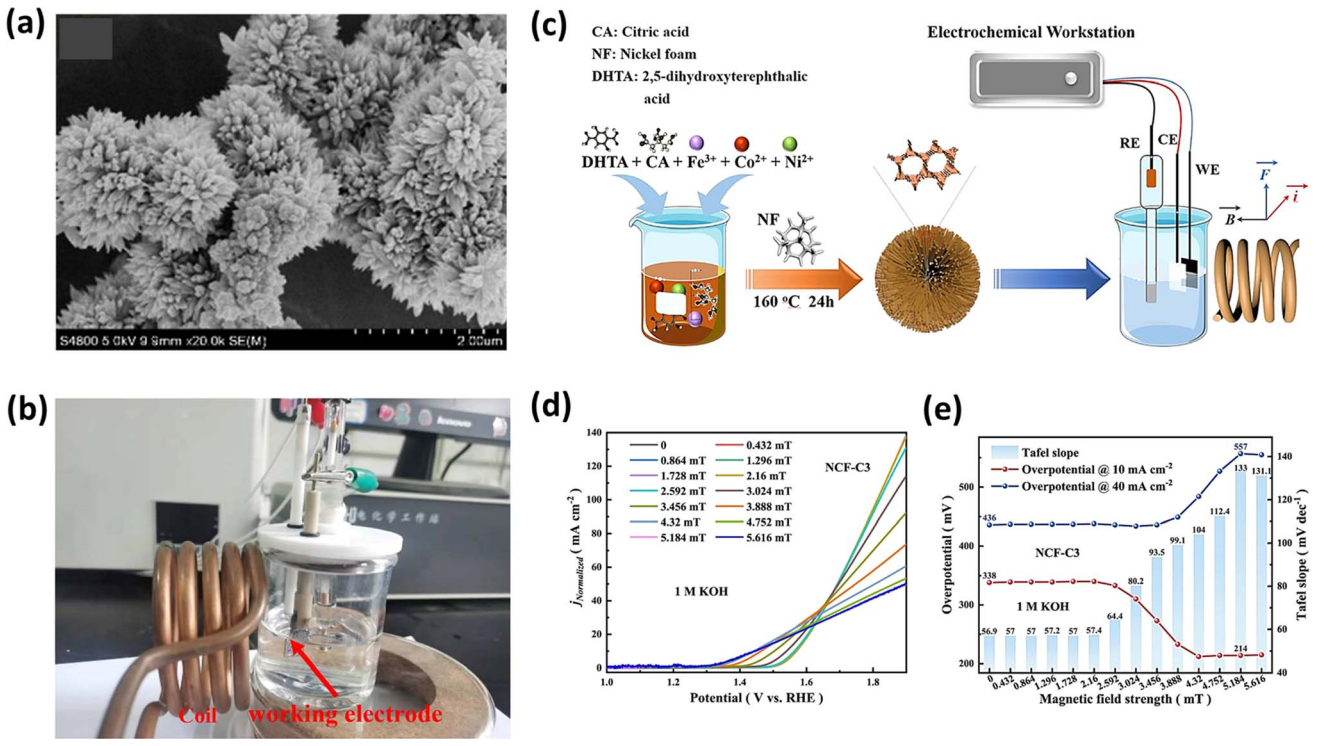

Fig. 21 (a) SEM image of $Co_{0.4}Ni_{0.6}$MOF-74, (b) real-time image of electrochemical measurement under an AMF (reprinted with permission,[204] copyright 2022, Elsevier). (c) Schematic of the synthesis of NiCoFe-MOF74 and its electrochemical measurements, (d) LSV curves of the sample at various magnetic field intensities and (e) summary of overpotential and histogram plots of the electrocatalysts under different magnetic field intensities (reprinted with permission,[205] copyright 2021, Elsevier).

Table 4 Summary of the different OER electrocatalysts used under a magnetic field of varying strengths

Nanomaterial	Employed MF	OER parameter without MF	OER parameter with MF	Ref.
$Cr_2Ge_2Te_6$	Uniform MF	$\eta_{10} = 282$ mV $b = 75.1$ mV dec^{-1}	$\eta_{10} = 231$ mV $b = 64.1$ mV dec^{-1}	192
$LaCoO_3$	Uniform MF	$\eta_{10} = 510$ mV $b = 151.98$ mV dec^{-1}	$\eta_{10} = 490$ mV $b = 72.13$ mV dec^{-1}	193
$YMn_{1-0.1}Cr_{0.1}O_3$	400 mT	$b = 208.1$ mV dec^{-1} $R_{ct} = 12$ Ω	$b = 185.8$ mV dec^{-1} $R_{ct} = 5$ Ω	194
Cu_1–Ni_6Fe_2–LDH	800 mT	$\eta_{10} = 210$ mV	$\eta_{10} = 180$ mV	195
$NiFe_2O_4$	1 T	$b = 135.4$ mV dec^{-1}	$b = 45.28$ mV dec^{-1}	196
NiFe-LDH	200 mT	$\eta_{10} = 249$ mV $b = 60$ mV dec^{-1}	$\eta_{10} = 207$ mV $b = 41.7$ mV dec^{-1}	198
Co_3O_4/NF	125 mT	$\eta_{20} = 308$ mV $b = 82.1$ mV dec^{-1}	$\eta_{20} = 252$ mV $b = 26.7$ mV dec^{-1}	197
1T-VSe_2	800 mT	$\eta_{10} = 307$ mV $b = 100.2$ mV dec^{-1}	$\eta_{10} = 228$ mV $b = 83.5$ mV dec^{-1}	199
$CoFe_2O_4$	1 T	$b = 109$ mV dec^{-1}	$b = 87.8$ mV dec^{-1}	122
Ni(OH), NiO, Ni	1.4 T	η_{10} = —	η_{10} = decreased by 12, 11, and 20 mV respectively	200
$Fe_{35}Co_{65}$	700 mT	η_{20} = —	η_{20} = decreased by 12 mV	201
NiFe/NiFeOOH	3.9 mT	$\eta_{10} = 342.2$ mV $b = 107.1$ mV dec^{-1}	$\eta_{10} = 209.2$ mV $b = 65$ mV dec^{-1}	202
$CoSe_2$	4.1 mT	$\eta_{10} = 296$ mV $b = 69.9$ mV dec^{-1}	$\eta_{10} = 239$ mV $b = 55.46$ mV dec^{-1}	203
$Co_{0.4}Ni_{0.6}$MOF-74	5.5 mT	$\eta_{10} = 314$ mV	$\eta_{10} = 201$ mV	204
NiCoFe/MOF-74	5.184 mT	$\eta_{10} = 273$ mV	$\eta_{10} = 214$ mV	205
Co@MoS_2	0.2 T	$\eta_{10} = 317$ mV $b = 97$ mV dec^{-1}	$\eta_{10} = 250$ mV $b = 62$ mV dec^{-1}	206

electromagnetic induction. In an alternative method, Gong *et al.*[206] employed laser molecular beam epitaxy to proficiently bind single Co atoms, possessing magnetic properties, onto the upper Mo sites of the MoS_2 framework. This induced the magnetic reorientation of the Co atoms within the matrix and localized heating of the active sites, resulting in a significant decrease by 67 mV in the overpotential value of the electrocatalyst when assessed under an AMF. Table 4 summarizes the different electrocatalysts used to study the magnetic effect on their OER activity.

5.3. Magnetic field-enhanced ORR

There is a particular category of reactions involving the transfer of both a proton and an electron from one atom to another.[207] These reactions, termed proton-coupled electron transfer (PCET) processes, are notably prevalent in ORR. PCET reactions are ubiquitous in nature, occurring during various metabolic processes such as glucose oxidation, aerobic respiration, and hydrogen oxidation in fuel cells. These processes are facilitated by catalysts or metalloenzymes containing transition metal ions at their active sites.[208,209] Although the ORR, which involves a four-electron transfer, is typically kinetically sluggish and necessitates electrocatalysts to surmount these barriers, platinum exhibits a superior performance, occupying the apex of the activity volcano plot, as shown in Fig. 5c. Consequently, extensive research has been dedicated to developing catalysts based on first-row transition metals to lower the required potential. In most biological systems, iron-containing enzymes are prevalent among oxygen-activating enzymes due to the capability of iron to adopt multiple redox states and its availability in various oxidation states, offering numerous open-shell spin states. Notably, high-spin iron(II) is crucial for dioxygen molecule binding and activation.[209,210] Multielectron processes such as the ORR pose challenges for single metal sites, leading to the involvement of bi-metallic sites.[211] Although the ORR typically involves triplet O_2 in its ground state, the spin conservation rule necessitates a spin flip for the transformation to singlet O_2, which is considered to be more reactive than the former to interact with singlet $OH^-/H_2O_2/H_2O$ intermediates, introducing an additional free-energy barrier.[212] Additionally, amidst these endeavours, the application of an external magnetic field to enhance the catalysis of the ORR remains a relatively unexplored avenue. Subsequent paragraphs will delve into the methodologies and underlying mechanisms associated with this approach.

To investigate the impact of bimetallic electrocatalysts on ORR under an external magnetic field favouring ORR activity, Kiciński *et al.*[213] synthesized a nitrogen-containing porous polymeric material (carbon) doped with iron, and further co-doped with one of several metals (chromium, manganese, cobalt, copper, or zinc), maintaining a 3 : 1 molar ratio of iron to the other metal. They varied the angle between the magnetic field direction and electrode surface area from 0° to 90°. Remarkably, the material co-doped with cobalt and pyrolyzed up to 700 °C (Fe/Co-N_x/C) exhibited a superior performance compared to the other metal co-doped samples. This group suggested that the external field enhanced the performance of the catalyst by increasing the transport efficiency of paramagnetic O_2 and enhancing its inherent activity. Placing a magnet near the electrode doubled the activity of the copper

co-doped electrocatalyst, whereas the activity of the cobalt co-doped electrocatalyst increased five-fold, as depicted in Fig. 22a and b, respectively. The possible explanation for this is the presence of copper and cobalt sites in two oxidation states and the optimal distance between them, facilitating electron relay to neighbouring sites, as supported by the literature.[215] In another aspect, the same ORR was performed with a rotating ring-disk electrode, which proved that Fe/Mn–N_x/C and Fe/Zn–N_x/C were the better electrocatalysts under these conditions in the presence of a magnetic field, as shown in Fig. 22c. Similarly, to explore the ORR activity of bimetallic electrocatalysts, Tufa *et al.*[214] synthesized a precisely controlled 3D structure consisting of Fe_3O_4 nano shells encapsulated with silver, termed a magnetoplasmonic (MagPlas) composite, as depicted in Fig. 22d. Notably, the ORR activity of the MagPlas composite increased by 1.13-fold in the presence of an external magnetic field. Computational simulations corroborated these findings, suggesting that the Lorentz force facilitates the rapid transport of the reacting species toward the working electrode. In a prior investigation, Kiciński *et al.*[216] examined the impact of a magnetic field on ORR using sulphur-doped Fe–N–C samples. They conducted experiments using both the original sulphur-doped samples and by reducing the Fe nano seeds through two successive reductive treatments involving pyrolysis or H_2 annealing.

In a unique approach to create electrocatalysts, Yan *et al.*[217] utilized the electrospinning technique, as seen in Fig. 23a, with various precursors to generate nanofibers. Subsequently, these nanofibers were doped with nitrogen, fluorine, and boron, while cobalt acetate was reduced to Co nanodots to serve as the magnetic component of the electrocatalyst. The resulting electrocatalyst appeared as highly porous fibres, as depicted in Fig. 23b. The linear sweep voltammetry (LSV) results obtained from the rotating disk electrode (RDE) and rotating ring disk electrode (RRDE) experiments indicated that the half-wave potential could be increased by 20 mV under a magnetic field. In a similar investigation, Zheng *et al.*[218] employed the electrospinning technique to produce well-oriented nitrogen-doped electrospun carbon nanofibers (ECNFs). Subsequently, they utilized the electrodeposition method under a consistent low current to uniformly apply Co_3O_4, forming a film on the substrate, as illustrated in Fig. 23c. Notably, Helmholtz coils were employed to induce an external magnetic field for investigating the enhancement in ORR activity, as shown in Fig. 23d. Their findings demonstrated that the magnetic field induced polarization of the unpaired electron spins in Co_3O_4, facilitating the four-electron ORR process, while inhibiting the two-electron process that leads to the formation of the byproduct H_2O_2. In a recent investigation, Yang *et al.*[219] employed an external magnetic field to analyse the diffusion rates of oxygen toward the electrode. They attributed the enhancement in ORR activity to the magnetohydrodynamic flows induced by the Lorentz force, as illustrated in Fig. 23e. Additionally, this team explored the impact of the residual magnetization effect in electrocatalysts containing magnetic materials such as CoPt alloys and Pt/FeCo heterostructures. Table 5 summarizes the different electrocatalysts used to study the magnetic field effect on their ORR activity.

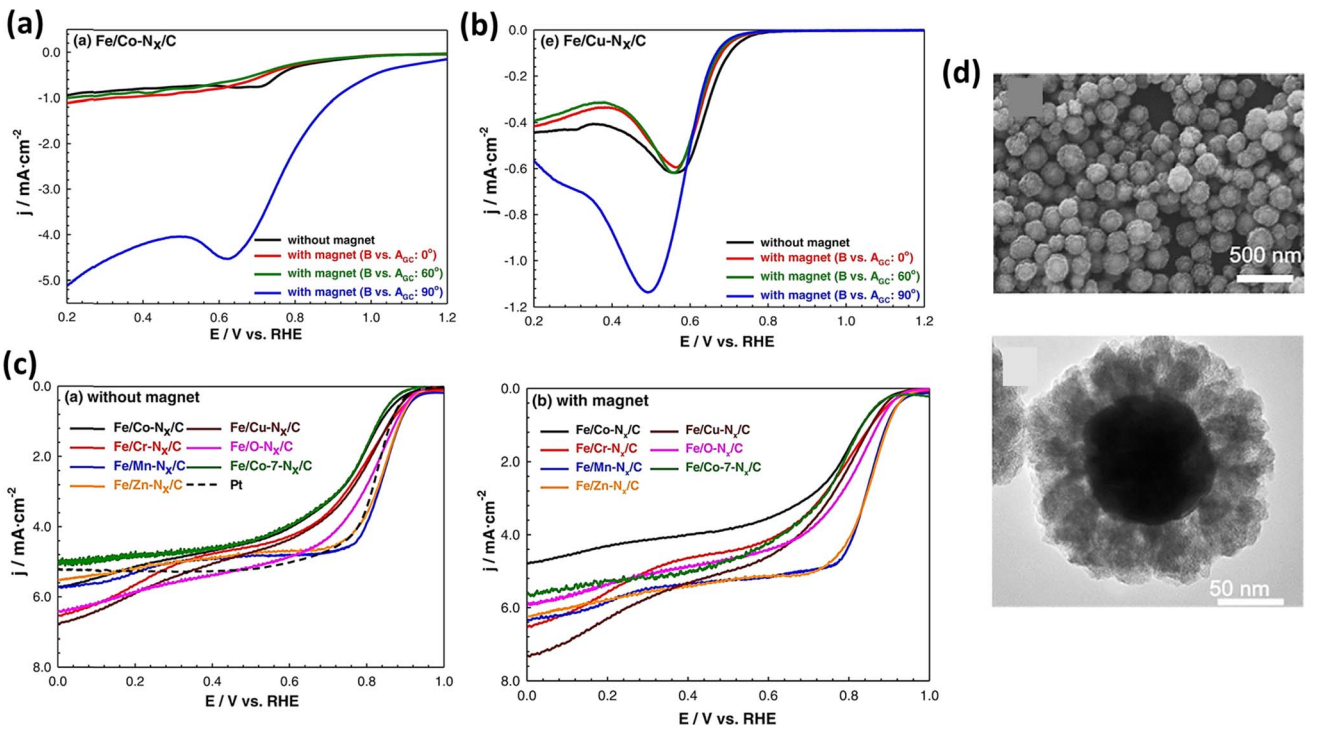

Fig. 22 (a) and (b) ORR polarization plots of Fe/Co–N_x/C and Fe/Cu–N_x/C, respectively, and (c) RRDE curves plotted in the presence and absence of a magnetic field for the above-mentioned electrocatalysts (reprinted with permission,[213] copyright 2022, Elsevier). (d) SEM and TEM images of Fe_3O_4-encapsulated Ag shells (reprinted with permission,[214] copyright 2020, the American Chemical Society).

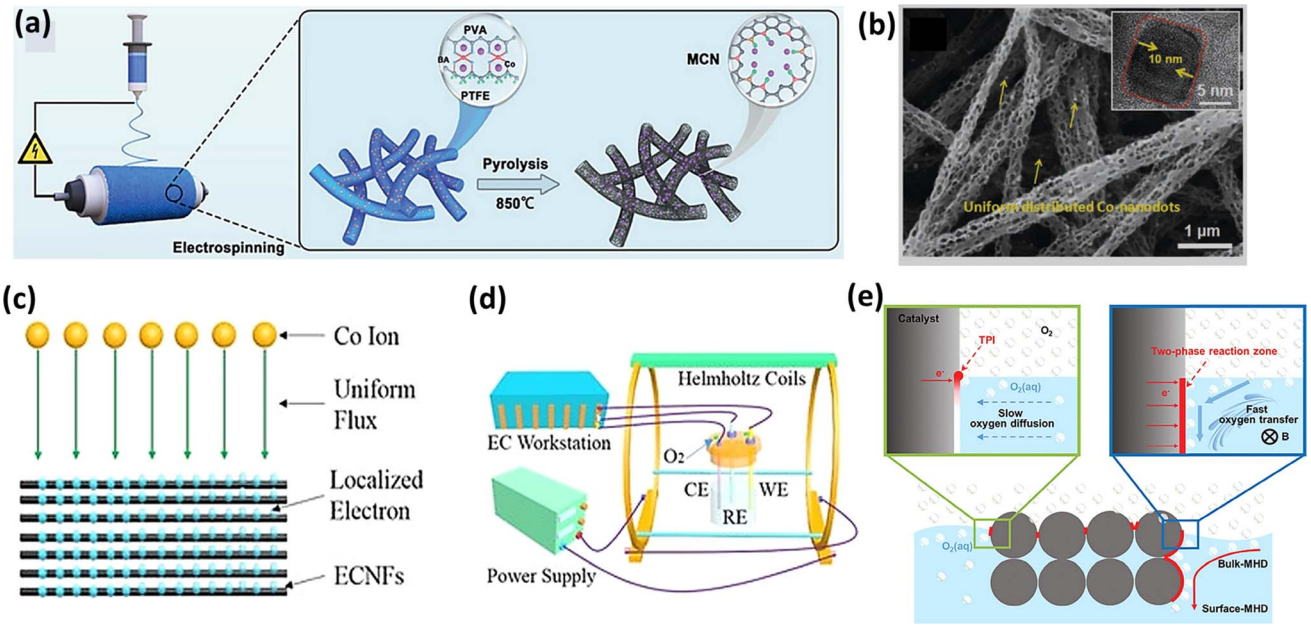

Fig. 23 (a) Schematic of using sol–gel electrospinning and pyrolysis. (b) Surface image of magnetic nanocages with the inset showing a single Co nanodot (reprinted with permission,[217] copyright 2020, Wiley). (c) Schematic of the uniform deposition of Co^{2+} and (d) schematic depiction of generating a magnetic field with Helmholtz coils and analysis of ORR (reprinted with permission,[218] copyright Wiley).

Table 5 Summary of the different electrocatalysts used to study the magnetic field effects on their ORR activity

Nanomaterial	Employed MF	ORR parameter without MF	ORR parameter with MF	Ref.
TM–N–C (TM = Co)	Uniform MF	b = 449 mV dec^{-1}	b = 66 mV dec^{-1}	213
Ag@Fe_3O_4	380 mT	Activity = —	Activity = increase by 1.13-fold	215
Fe–N–C/S–H_2	Uniform MF	b = 60 mV dec^{-1} (alkaline media) b = 43 mV dec^{-1} (acidic media)	b = 39 mV dec^{-1} (alkaline media) b = 29 mV dec^{-1} (acidic media)	216
N–F–B/C–Co	350 mT	$E_{\frac{1}{2}}$ = —	$E_{\frac{1}{2}}$ = increase by 20 mV	217
Co_3O_4–C	1.32 mT	n (number of e$^-$ transfer) = 2.28	n = 2.35	218
Pt based materials	435 mT	J = —	J = improved by 60%	219

5.4. Magnetic field-enhanced CO_2RR

With the recent acceleration in globalization, the amount of pollutants such as CO_2 that contain carbon has been constantly rising. Therefore, changing CO_2 into useful or less hazardous compounds can be one of the best alternatives to address this issue. CO_2RR, or the electrochemical reduction of CO_2, is one way to achieve this. However, the energy efficiency, reaction selectivity, and total conversion rates are still major obstacles in electrocatalytic CO_2RR. Nevertheless, techniques are available to enhance the selectivity for the intended products despite these obstacles. For instance, in producing formic acid, the singlet radical pair configuration ($[CO_2^{-\bullet}\uparrow\cdots H^{\bullet}\downarrow]$) plays a crucial role, rather than the triplet radical pair ($[CO_2^{-\bullet}\uparrow\cdots H^{\bullet}\uparrow]$).[220,221] Thus, applying a magnetic field can facilitate the transition of spin-related radicals from the triplet state to the singlet state, which is advantageous for CO_2RR. This spin evolution enhances the efficiency and selectivity of the electrochemical reduction process, contributing to more effective CO_2 conversion.[222]

Pan *et al.* managed to double the yield of formic acid from CO_2 by utilizing an electrode of Sn nanoparticles and applying a 0.9 T external magnetic field.[223] Fig. 24a depicts the probable spin-dependent reaction pathway of the radical intermediates during CO_2 reduction. Fig. 24b highlights the enhancement in the CO_2RR magneto-electrochemical performance when the concentration of the supporting electrolyte was increased, while maintaining the same magnetic field. The magnetic field facilitated the conversion of spin-forbidden triplet radical pairs into spin-favourable singlet radical pairs, which explains the increase in yield. The amount of end-product depends on the ratio of triplet to singlet radical pairs. In the absence of an external magnetic field, the triplet and singlet states of the intermediate radical pair maintain a dynamic equilibrium. The presence of a magnetic field disrupts this equilibrium, reducing the triplet-to-singlet ratio and increasing the singlet radicals. Therefore, by converting triplet to singlet radical pairs, the magnetic field helps increase the product yield. In another attempt to study the effect of an external magnetic field on the activity and selectivity in CO_2RR, Wang *et al.* examined Cu_2O as

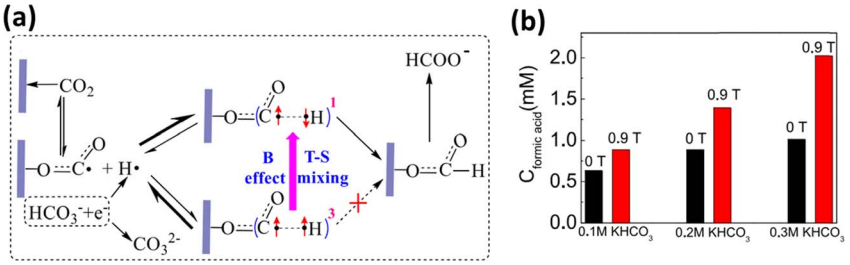

Fig. 24 (a) Proposed spin-dependent mechanism for the CO_2 reduction reaction and (b) increase in yield of formic acid under the influence of a magnetic field (reprinted with permission,[223] copyright 2020, the American Chemical Society).

an electrocatalyst in the presence of an *in situ* magnetic field.[224] This group observed a 25.3% and 54.7% increase in current density when the magnetic field strength was 1 T and 3 T, respectively, and even the onset potential was decreased by 114 mV (Fig. 25a). The effect of an intermittent magnetic field was also studied, as shown in Fig. 25b, where it evident that the effect of a magnetic field is straightforward and reversible in nature. This group also observed relatively less faradaic efficiency towards C_{2+} products as the magnetic field favoured the formation of C_1 products. This was further confirmed by DFT calculations, where the results obviously showed that compared with the unspin polarized surface, the spin polarized surface lowers the energy barrier for the HCOOH reaction path and increases the reaction path of CO intermediates. Fig. 25c represents the free energy diagram of the HCOOH and CO intermediates.

5.5. Other magnetic field-enhanced electrochemical reactions

The above-mentioned electrochemical applications have been explored to an appreciable extent; nonetheless, other electrochemical reactions have been explored to study the magnetic field enhancement in electrocatalytic activity. For instance, alcohol oxidation reactions, where Zhu *et al.* enhanced the

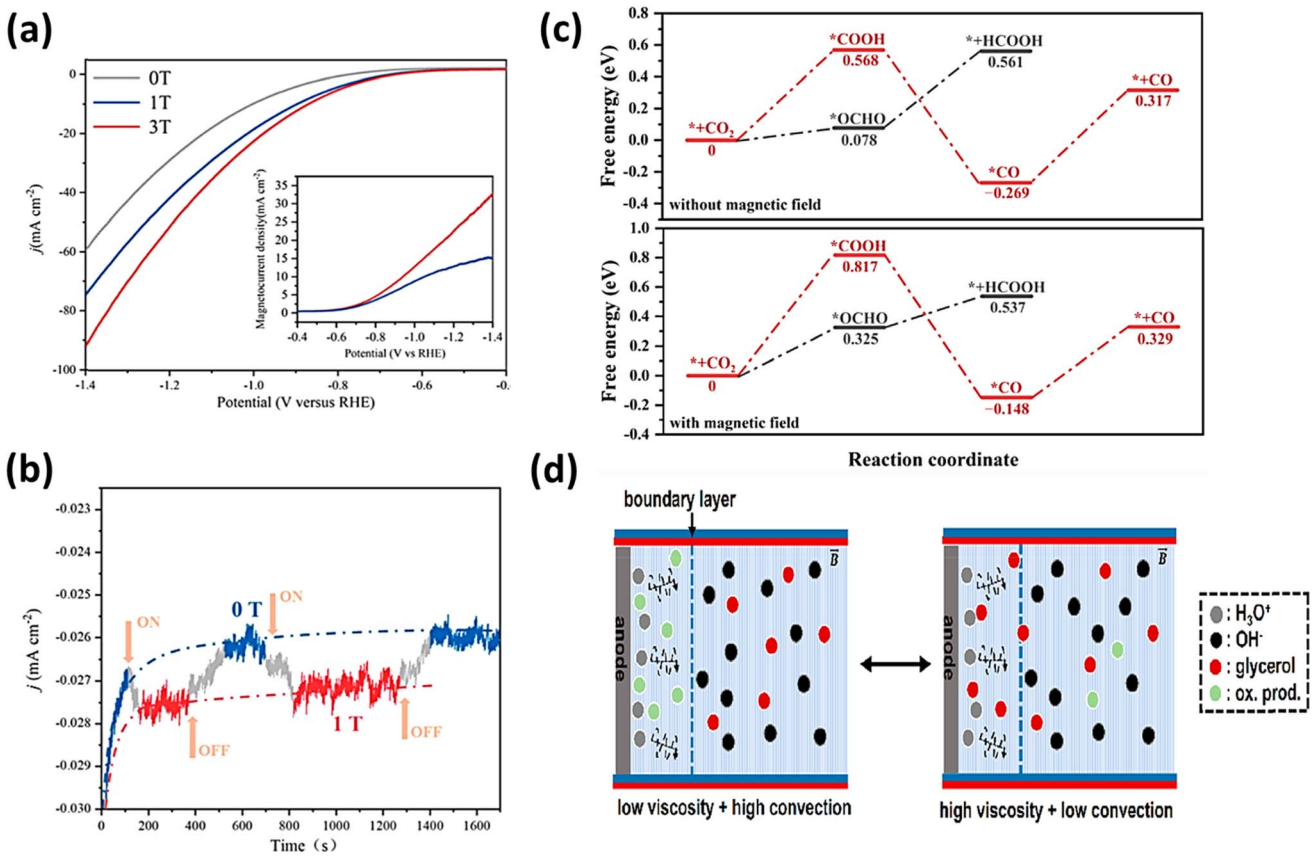

Fig. 25 (a) LSV curves of CO_2 reduction in the presence and absence of a magnetic field, (b) *j vs. t* graph showing the effect of an intermittent magnetic field and the corresponding reversible response in current density, and (c) free energy diagram for CO_2RR to produce HCOOH and CO on spin polarized and unpolarized catalyst (reprinted with permission,[224] copyright 2023, MDPI). (d) Schematic depiction of the use of a magnetic field to cause electrochemical oscillations by Lorentz force (reprinted with permission,[225] copyright 2022, the American Chemical Society).

methanol oxidation reaction (MOR) performance of $Co_{42}Pt_{58}$ truncated octahedral nanoparticles (TONPs) as ferromagnetic catalysts by applying a magnetic field.[226] When the magnetic field strength reached 3000 Oe, the reaction rate of $Co_{42}Pt_{58}$ TONPs for MOR increased by 14.1%. The DFT calculations and current peak analysis demonstrated that the external magnetic field reduces the activation barrier for methanol and water through strong quantum spin-exchange interactions. This facilitates the production of CO_{ad} on the Pt sites and OH_{ad} on the Co sites. Subsequently, CO_{ad} is oxidized to CO_2 by OH_{ad}, mitigating the CO poisoning of Pt. In another work, Gao *et al.* utilized the Lorentz force potential to increase the mass transport of glycerol and glyceraldehyde in an electrochemical reaction of glycerol oxidation (EOG).[225] There are two major steps noted in this process, where the first is glycerol oxidation near the anode rapidly decreases the viscosity of the electrolyte near its vicinity, and secondly, taking advantage of this low viscosity, the magnetic field increases the mass transfer of glycerol and glyceraldehyde near the anode, which in turn increases the viscosity (Fig. 25d). This is regarded as the time-delayed negative feedback, which generates chemical oscillations in the system. These chemical oscillations have an impact on the effective potential of the electrode and concentration of the active species near its vicinity, consequently enhancing the selectivity for glyceric acid in EOG. This group successfully demonstrated the enhancement in selectivity by the application of an external magnetic field.

6. Summary

Electrocatalytic reactions have been proven to play a very impactful role in sustainable energy conversion and storage technologies, for which advanced electrocatalysts are needed to speed up their slow reaction kinetics. Alternatively, the use of a magnetic field to enhance the performance of the electrocatalysts has gained interest from researchers. The use of an external magnetic field has been shown to be important in both electrode fabrication techniques and electrocatalytic reactions.

Table 6 Summary of the different mechanisms of enhancement proposed in the literature

Electrochemical reaction	Electrocatalyst material	Proposed mechanism of enhancement	Ref.
HER	NiCoFe based	Lorentz force	172
HER	$NiCo_2S_4$	Lorentz force	173
HER	MoS_2	Spin selectivity	174
HER	$Ni_{43}Mn_{32}In_{25}$	Spin selectivity	175
HER	Heusler alloys	—	176
HER	Ni–W	Lorentz force	177
HER	Gd–MoS_2	Spin selectivity; magnetothermal effect	180
HER	MoS_2	MHD	181
HER	NiSe based	Magnetothermal	183
HER	Fe–Co–Ni–P–B	Lorentz force	184
HER	Ni–FeC	Magnetothermal	186
OER	$Cr_2Ge_2Te_6$	Lorentz force; magnetic hyperthermia	192
OER	$LaCoO_3$	MHD	193
OER	$YMn_{1-x}Cr_xO_3$	—	194
OER	Cu–NiFe–LDH	Spin selectivity	195
OER	$NiFe_2O_4$	Spin selectivity	196
OER	NiFe based	MHD	198
OER	Co_3O_4	MHD	197
OER	VSe_2	Spin polarization	199
OER	$CoFe_2O_4$	Spin polarization	122
OER	Ni based	Spin selectivity; MHD	200
OER	FeCo based	Spin selectivity	201
OER	NiFe/C	Magnetic hyperthermia	202
OER	$CoSe_2$/C	Magnetic hyperthermia	203
OER	$Co_{0.4}Ni_{0.6}$MOF-74	Spin polarization; MHD; improved active point temperature	204
OER	NiCoFe–MOF-74	MHD	205
OER	Co–MoS_2	Magnetic hyperthermia	206
ORR	Fe/Co–N_x/C based	Spin polarization	213
ORR	Fe_3O_4/Ag	MHD	214
ORR	Fe–N–C/S	—	216
ORR	Magnetic nanocages of Co; N; F; B	Spin polarization	217
ORR	Co_3O_4	Spin polarization	218
ORR	CoPt and Pt/FeCo	MHD	219
CO_2RR	Sn nanoparticles	Spin polarization	223
CO_2RR	Cu_2O	Spin polarization	224
MOR	$Co_{42}Pt_{58}$	Spin selectivity	226
EOR	Pt based	Lorentz force	225

Electrode fabrication techniques can exploit a magnetic field for the specific reconstruction of electrocatalysts by magnetic induction, structural modification of the electrocatalyst by specific alignment of the material to increase its active surface area, and even modify the band gap and other intrinsic properties of the material. Moreover, this technique of electrode fabrication is regarded as pollution free and non-toxic. The integration of a magnetic field with electrocatalytic reactions such as HER, OER, ORR, CO_2RR and others has proven to significantly enhance the performance of electrocatalysts in terms of efficiency, selectivity and overall performance. Thus, this innovative technique provides a sustainable and environmentally friendly approach for energy applications, and also expands the scope of catalytic conversions.

This review thoroughly explored the fundamentals of various electrocatalytic reactions and magnetic enhancement mechanisms and further provided an introductory and comprehensive explanation of magnetic field-assisted electrodeposition techniques for crafting highly efficient electrodes for electrocatalytic reactions. Furthermore, we presented an extensive discussion on recent reports concerning electrochemical reactions. Lastly, we addressed the challenges and prospects of leveraging external magnetic fields to enhance and broaden the scope of magnetoelectrochemistry. Table 6 list the reported electrochemical reactions enhanced by a magnetic field and highlights the underlying mechanism for the enhancement.

7. Challenges and future perspectives

To address the exponentially increasing demand for modern energy needs and renewable energy sources, we require more effective energy conversion solutions for electrochemical reactions. Utilizing a magnetic field to enhance the electrochemical performance of catalysts represents a novel approach in electrochemistry. An external magnetic field can influence the rate of electrochemical reactions, accelerate the mass transfer, alter the electrode environment, impact magnetoresistance, and even direct ion movement within an electrochemical cell. However, to fully grasp how a magnetic field enhances electrochemical reactions, we must consider some uncertainties surrounding this method. The mechanisms by which a magnetic field affects electrochemical reactions are complex and not entirely understood, necessitating detailed studies to elucidate their impact on the electron spin states, reaction intermediates, and overall reaction kinetics. Theoretical modelling and computational simulations are crucial in understanding the intricate interactions between magnetism and electrochemistry. Many nanomaterials that exhibit excellent electrocatalytic activity also display significant magnetic properties. The recently discovered two-dimensional materials have shown exceptional electrocatalytic performances but face challenges such as aggregation, restacking, and defect control. It is evident that applying a magnetic field can greatly mitigate these issues by aligning the magnetic nanoparticles and other components within 2D materials, maintaining a higher surface area and active site availability, and the magnetic field can facilitate the uniform distribution of defects; however, although beneficial, these aspects remain less explored. A comprehensive understanding of the magnetic behaviors of these materials under the influence of a magnetic field and their impact on electrocatalytic performance requires deeper investigation. Magnetic field-enhanced reactions have specificity towards the nature of reactants and reactions. Magnetic electrocatalysts show positive effects in the presence of a magnetic field, but challenges arise when the reactant is diamagnetic. For instance, N_2 and NO_x compounds are diamagnetic and repelled by the magnetic elements of the electrode in nitrogen reduction reactions. Thus, alternative approaches and tactics should be employed to enhance the catalytic activity, such as designing composite catalysts with both magnetic and non-magnetic components. The magnetic component can facilitate mass transfer, while the non-magnetic component aids in the adsorption of diamagnetic reactants.

A thorough understanding of the conversion extent from triplet to singlet forms in CO_2RR, or from singlet to triplet forms in ORR, remains incomplete. *In situ* electron paramagnetic resonance spectroscopy can detect and quantify radicals, offering insights into their spin states and interactions with a magnetic field. This technique can help establish a clear relationship between reaction efficiency and the triplet-to-singlet ratio. The alignment of the magnetic field relative to the current density in the reaction system, as well as the proper orientation of the electrode surface concerning the magnetic field, significantly enhances the activity of catalysts. Advanced devices with adjustable magnetic field strengths can ensure the correct orientation of the electrode and allow monitoring of electrochemical evaluation parameters such as changes in current density, ionic/electronic pathways, and magnetoresistance. The potential of magnetic field-enhanced electrochemical performance in porous carbon-based hybrid materials needs exploration, given that carbon-based materials such as carbon nanotubes, graphene, and carbon dots offer increased intrinsic surface area for magnetic materials. Also, although the activity enhancement of magnetic materials is well-documented, varying the concentration of magnetic components can provide a deeper understanding of the specific enhancement effects. The magnetothermal effect on electrocatalytic performance is less explored, despite reports on an increase in electrocatalytic activity with temperature. Traditional heating methods pose significant drawbacks, whereas using a magnetic solenoid with an alternating current can create localized heating of catalyst nanoparticles, thereby boosting their electrocatalytic activity.

Novel materials in the ferromagnetic, ferrimagnetic, and paramagnetic categories can be developed in hybrid forms with varying compositions of magnetic and non-magnetic components. Exploring the magnetic field activity in these materials in different electrolyte systems, such as ionic liquids, can broaden the scope of this field. Adding paramagnetic species to electrolyte systems to control the magnetic field concentration gradient can enhance the electrocatalytic performance. Fabricating electrodes in the presence of an external magnetic field can promote uniform deposition on the surface, enhance the mass loading of the material and align the material to create

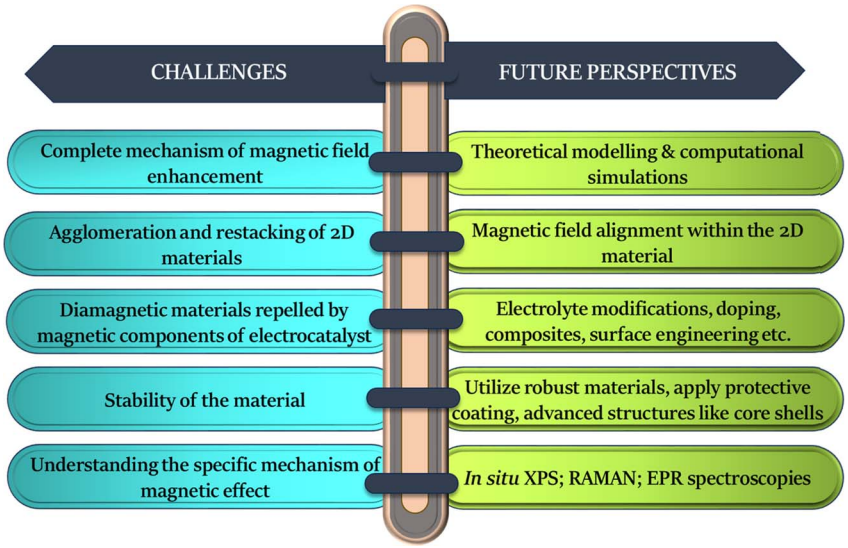

Fig. 26 Schematic representation of challenges and future perspectives of combining a magnetic field and electrocatalysis.

more active sites, enabling the large-scale production of magnetically active electrodes. However, implementing magnetic field enhancement in industrial-scale processes presents practical challenges. Designing reactors and electrochemical cells to uniformly apply a magnetic field to large volumes of reactants is essential. The long-term stability and durability of electrocatalysts under magnetic field conditions also need assessment. Strategies such as using robust materials such as transition metal alloys and certain metal oxides, applying protective coatings, and developing advanced catalyst structures such as core-shells and composites can significantly improve the stability of electrocatalysts under an external magnetic field. These strategies can also be applied in energy storage applications, such as exploring the impact of magnetic fields on Zn–air batteries, presenting a promising area for future research. Zn–air batteries rely on the oxygen reduction reaction (ORR) during discharge and the oxygen evolution reaction (OER) during charge. Thus, by applying a magnetic field, it may be possible to enhance the catalytic efficiency of these reactions, thereby improving the overall performance and stability of Zn–air batteries. Investigating how magnetic fields influence the catalytic behaviour of materials used in Zn–air batteries, particularly for ORR and OER, will be crucial in developing advanced energy storage solutions that leverage magnetic field enhancements.

Developing advanced observation techniques during synthesis and electrocatalytic processes under an external magnetic field is crucial. Specific magnetic materials may transform into different forms, such as altering spin configurations, modifying active sites, or undergoing structural reconstruction due to the influence of an external magnetic field. Monitoring these changes requires *in situ* techniques, where the mechanisms are examined concurrently with external manipulations. For instance, *in situ* X-ray photoelectron spectroscopy (XPS) or Raman spectroscopic techniques can aid in both fabrication and mechanistic understanding. Fig. 26 schematically represents the challenges and prospects of magnetic field-enhanced electrocatalysis.

Considering the benefits and challenges of magnetic field-enhanced electrocatalysis, developing and mastering appropriate techniques can significantly advance green energy initiatives. Transitioning from laboratory-scale to industrial-scale applications can make technology-assisted electrochemistry a key solution in climate change mitigation efforts. Finally, recognising the importance of evaluating the energy cost of generating a magnetic field relative to the efficiency gains in electrocatalytic processes, future research should focus on detailed energy balance studies and cost-benefit analyses to determine the overall viability of magnetic field-enhanced electrocatalysis.

Data availability

No primary research results, software or code has been included and no new data were generated or analysed as part of this review.

Conflicts of interest

The authors declare no conflict of interest.

Acknowledgements

The authors extend their appreciation for the financial assistance provided by the SERB Core Research Grant (Grant No. CRG/2022/000897) and the Department of Science and Technology (DST/NM/NT/2019/205(G)). They also express gratitude for the support received through the Minor Research Project Grant from Jain University (JU/MRP/CNMS/29/2023). CSR acknowledges backing from the National Research Foundation of Korea under the Brain Pool program, funded by the Ministry of Science and ICT, South Korea (Grant No. RS-2023-00222186).

The work is further supported by the National Research Foundation of Korea (NRF) and the Commercialization Promotion Agency for R&D Outcomes (COMPA), funded by the Ministry of Science and ICT (Grant No. RS-2023-00217581, RS-2023-00304768).

References

1 M. Farghali, A. I. Osman, I. M. A. Mohamed, Z. Chen, L. Chen, I. Ihara, P.-S. Yap and D. W. Rooney, *Environ. Chem. Lett.*, 2023, **21**, 2003–2039.
2 A. J. Gabric, *Atmosphere*, 2023, **14**, 1081.
3 U. N. Environment, Emissions Gap Report 2020, **http://www.unep.org/emissions-gap-report-2020**, accessed November 29, 2023.
4 Chapter 2 — Global Warming of 1.5 °C, **https://www.ipcc.ch/sr15/chapter/chapter-2/**, accessed November 29, 2023.
5 A. Jahanger, I. Ozturk, J. Chukwuma Onwe, T. E. Joseph and M. Razib Hossain, *Sustain. Energy Technol. Assessments*, 2023, **56**, 103084.
6 T. N. Nchofoung, H. K. Fotio and C. W. Miamo, *Renew. Energy Focus*, 2023, **44**, 334–343.
7 M. Pathak, S. M. Jeong and C. S. Rout, *J. Energy Storage*, 2023, **73**, 108881.
8 S. Radhakrishnan, A. Patra, G. Manasa, M. A. Belgami, S. Mun Jeong and C. S. Rout, *Adv. Sci.*, 2024, **11**, 2305325.
9 M. Rahimi, A. Khurram, T. Alan Hatton and B. Gallant, *Chem. Soc. Rev.*, 2022, **51**, 8676–8695.
10 S. Cembellín and B. Batanero, *Chem. Rec.*, 2021, **21**, 2453–2471.
11 J. Xian, S. Li, H. Su, P. Liao, S. Wang, R. Xiang, Y. Zhang, Q. Liu and G. Li, *Angew. Chem.*, 2023, **135**, e202306726.
12 D. Dolui, S. Ghorai and A. Dutta, *Coord. Chem. Rev.*, 2020, **416**, 213335.
13 Y. Zhang, S. Lee, S. Jeong, E. Son, J. M. Baik, Y.-K. Han and H. Park, *Adv. Funct. Mater.*, 2024, **34**, 2309250.
14 B. Cui, Z. Hu, C. Liu, S. Liu, F. Chen, S. Hu, J. Zhang, W. Zhou, Y. Deng, Z. Qin, Z. Wu, Y. Chen, L. Cui and W. Hu, *Nano Res.*, 2021, **14**, 1149–1155.
15 P. Cui, L. Zhao, Y. Long, L. Dai and C. Hu, *Angew. Chem.*, 2023, **135**, e202218269.
16 J. Wang, R. Gao, D. Zhou, Z. Chen, Z. Wu, G. Schumacher, Z. Hu and X. Liu, *ACS Catal.*, 2017, **7**, 6533–6541.
17 X. Li, D. Wang, S. Zha, Y. Chu, L. Pan, M. Wu, C. Liu, W. Wang, N. Mitsuzaki and Z. Chen, *Int. J. Hydrogen Energy*, 2024, **51**, 1110–1127.
18 Y.-R. Ji, Y.-F. Guo, X. Liu, P.-F. Wang and T.-F. Yi, *Chem. Eng. J.*, 2023, **471**, 144743.
19 N. Han, K. R. Yang, Z. Lu, Y. Li, W. Xu, T. Gao, Z. Cai, Y. Zhang, V. S. Batista, W. Liu and X. Sun, *Nat. Commun.*, 2018, **9**, 924.
20 A. Dymerska, W. Kukułka, M. Biegun and E. Mijowska, *Materials*, 2020, **13**, 3918.
21 F. Yan, L. Yan, X. Wei, Y. Han, H. Huang, S. Xu, X. Liang, W. Zhou and J. Guo, *Int. J. Hydrogen Energy*, 2022, **47**, 10616–10627.
22 T. Wu, C. Dong, D. Sun and F. Huang, *Nanoscale*, 2021, **13**, 1581–1595.
23 A. H. Al-Naggar, N. M. Shinde, J.-S. Kim and R. S. Mane, *Coord. Chem. Rev.*, 2023, **474**, 214864.
24 K. Fominykh, P. Chernev, I. Zaharieva, J. Sicklinger, G. Stefanic, M. Döblinger, A. Müller, A. Pokharel, S. Böcklein, C. Scheu, T. Bein and D. Fattakhova-Rohlfing, *ACS Nano*, 2015, **9**, 5180–5188.
25 Y. Xie, B. Zhao, K. Tang, W. Qin, C. Tan, J. Yao, Y. Li, L. Jiang, X. Wang and Y. Sun, *Chem. Eng. J.*, 2021, **409**, 128156.
26 K.-H. Kim, K.-H. Kim, W. Choi, Y.-M. Kim, S.-H. Hong and Y.-H. Choi, *Nanoscale*, 2022, **14**, 8281–8290.
27 J. Duan, K. Guo, H. Li, J. Li, Y. Peng, H. Ma and C. Xu, *Appl. Surf. Sci.*, 2023, **615**, 156361.
28 T. I. Singh, A. Maibam, D. C. Cha, S. Yoo, R. Babarao, S. U. Lee and S. Lee, *Adv. Sci.*, 2022, **9**, 2201311.
29 Y. Cong, S. Huang, Y. Mei and T.-T. Li, *Chem.–Eur. J.*, 2021, **27**, 15866–15888.
30 H. Li, C. Cai, Q. Wang, S. Chen, J. Fu, B. Liu, Q. Hu, K. Hu, H. Li, J. Hu, Q. Liu, S. Chen and M. Liu, *Chem. Eng. J.*, 2022, **435**, 134860.
31 C. Yang, X. Xi, Z. Yu, H. Cao, J. Li, S. Lin, Z. Ma and L. Zhao, *ACS Appl. Mater. Interfaces*, 2018, **10**, 5492–5497.
32 Y. Zhang, H. Khanbareh, S. Dunn, C. R. Bowen, H. Gong, N. P. H. Duy and P. T. T. Phuong, *Adv. Sci.*, 2022, **9**, 2105248.
33 S. L. D. Nicole, Y. Li, W. Xie, G. Wang and J.-M. Lee, *Small*, 2023, **19**, 2206844.
34 Y. Zhang, P. Guo, S. Li, J. Sun, W. Wang, B. Song, X. Yang, X. Wang, Z. Jiang, G. Wu and P. Xu, *J. Mater. Chem. A*, 2022, **10**, 1760–1767.
35 J. Xu, P. Gu, D. J. S. Birch and Y. Chen, *Adv. Funct. Mater.*, 2018, **28**, 1801573.
36 M. Wang, Z. Wang and Z. Guo, *Int. J. Hydrogen Energy*, 2010, **35**, 3198–3205.
37 J. Wang, M. Yan, K. Zhao, X. Liao, P. Wang, X. Pan, W. Yang and L. Mai, *Adv. Mater.*, 2017, **29**, 1604464.
38 J. Yao, W. Huang, W. Fang, M. Kuang, N. Jia, H. Ren, D. Liu, C. Lv, C. Liu, J. Xu and Q. Yan, *Small Methods*, 2020, **4**, 2000494.
39 S. R. Ragsdale, K. M. Grant and H. S. White, *J. Am. Chem. Soc.*, 1998, **120**, 13461–13468.
40 B. Seo and S. H. Joo, *Nat. Energy*, 2018, **3**, 451–452.
41 J. M. D. Coey, R. Aogaki, F. Byrne and P. Stamenov, *Proc. Natl. Acad. Sci. U. S. A.*, 2009, **106**, 8811–8817.
42 A. L. Buchachenko and V. L. Berdinsky, *Chem. Rev.*, 2002, **102**, 603–612.
43 X. Jiang, Y. Chen, X. Zhang, F. You, J. Yao, H. Yang and B. Y. Xia, *ChemSusChem*, 2022, **15**, e202201551.
44 O. Devos, O. Aaboubi, J.-P. Chopart, A. Olivier, C. Gabrielli and B. Tribollet, *J. Phys. Chem. A*, 2000, **104**, 1544–1548.
45 Y. Jiang, K. Yang, M. Li, D. Xu and Z. Ma, *Mater. Chem. Front.*, 2024, **8**, 528–552.
46 V. Gatard, J. Deseure and M. Chatenet, *Curr. Opin. Electrochem.*, 2020, **23**, 96–105.

47 J. Yao, W. Huang, W. Fang, M. Kuang, N. Jia, H. Ren, D. Liu, C. Lv, C. Liu, J. Xu and Q. Yan, *Small Methods*, 2020, **4**, 2000494.
48 K. Wang, Q. Yang, H. Zhang, M. Zhang, H. Jiang, C. Zheng and J. Li, *J. Mater. Chem. A*, 2023, **11**, 7802–7832.
49 S. Luo, K. Elouarzaki and Z. J. Xu, *Angew. Chem. Int. Ed.*, 2022, **61**, e202203564.
50 X. Liu, M. Gong, S. Deng, T. Zhao, J. Zhang and D. Wang, *J. Mater. Chem. A*, 2020, **8**, 10130–10149.
51 Y. Li, Y. Sun, Y. Qin, W. Zhang, L. Wang, M. Luo, H. Yang and S. Guo, *Adv. Energy Mater.*, 2020, **10**, 1903120.
52 L. Zhang, P. Kuang and J. Yu, in *Graphene Oxide–Metal Oxide and Other Graphene Oxide-Based Composites in Photocatalysis and Electrocatalysis*, ed. J. Yu, L. Zhang and P. Kuang, Elsevier, 2022, pp. 1–30.
53 Y. Jiao, Y. Zheng, M. Jaroniec and S. Z. Qiao, *Chem. Soc. Rev.*, 2015, **44**, 2060–2086.
54 T. Reier, M. Oezaslan and P. Strasser, *ACS Catal.*, 2012, **2**, 1765–1772.
55 C. Li and J.-B. Baek, *ACS Omega*, 2020, **5**, 31–40.
56 P. Kuang, M. Sayed, J. Fan, B. Cheng and J. Yu, *Adv. Energy Mater.*, 2020, **10**, 1903802.
57 C. G. Morales-Guio, L.-A. Stern and X. Hu, *Chem. Soc. Rev.*, 2014, **43**, 6555–6569.
58 V. Vij, S. Sultan, A. M. Harzandi, A. Meena, J. N. Tiwari, W.-G. Lee, T. Yoon and K. S. Kim, *ACS Catal.*, 2017, **7**, 7196–7225.
59 N. Eliaz and E. Gileadi, *Physical Electrochemistry: Fundamentals, Techniques, and Applications*, John Wiley & Sons, 2019.
60 J. Zhu, L. Hu, P. Zhao, L. Y. S. Lee and K.-Y. Wong, *Chem. Rev.*, 2020, **120**, 851–918.
61 Y. Wang, W. Qiu, E. Song, F. Gu, Z. Zheng, X. Zhao, Y. Zhao, J. Liu and W. Zhang, *Natl. Sci. Rev.*, 2018, **5**, 327–341.
62 T. F. Jaramillo, K. P. Jørgensen, J. Bonde, J. H. Nielsen, S. Horch and I. Chorkendorff, *Science*, 2007, **317**, 100–102.
63 Z. W. Seh, J. Kibsgaard, C. F. Dickens, I. Chorkendorff, J. K. Nørskov and T. F. Jaramillo, *Science*, 2017, **355**, eaad4998.
64 A. B. Laursen, A. S. Varela, F. Dionigi, H. Fanchiu, C. Miller, O. L. Trinhammer, J. Rossmeisl and S. Dahl, *J. Chem. Educ.*, 2012, **89**, 1595–1599.
65 F. Zeng, C. Mebrahtu, L. Liao, A. K. Beine and R. Palkovits, *J. Energy Chem.*, 2022, **69**, 301–329.
66 K. Zhang and R. Zou, *Small*, 2021, **17**, 2100129.
67 I. C. Man, H.-Y. Su, F. Calle-Vallejo, H. A. Hansen, J. I. Martínez, N. G. Inoglu, J. Kitchin, T. F. Jaramillo, J. K. Nørskov and J. Rossmeisl, *ChemCatChem*, 2011, **3**, 1159–1165.
68 N.-T. Suen, S.-F. Hung, Q. Quan, N. Zhang, Y.-J. Xu and H. M. Chen, *Chem. Soc. Rev.*, 2017, **46**, 337–365.
69 E. Antolini, *ACS Catal.*, 2014, **4**, 1426–1440.
70 S. Cherevko, S. Geiger, O. Kasian, N. Kulyk, J.-P. Grote, A. Savan, B. R. Shrestha, S. Merzlikin, B. Breitbach, A. Ludwig and K. J. J. Mayrhofer, *Catal. Today*, 2016, **262**, 170–180.
71 R. A. Rincón, E. Ventosa, F. Tietz, J. Masa, S. Seisel, V. Kuznetsov and W. Schuhmann, *ChemPhysChem*, 2014, **15**, 2810–2816.
72 P. Roy Chowdhury, H. Medhi, K. G. Bhattacharyya and C. Mustansar Hussain, *Coord. Chem. Rev.*, 2023, **483**, 215083.
73 R. Chen, S.-F. Hung, D. Zhou, J. Gao, C. Yang, H. Tao, H. B. Yang, L. Zhang, L. Zhang, Q. Xiong, H. M. Chen and B. Liu, *Adv. Mater.*, 2019, **31**, 1903909.
74 H. Yin and Z. Tang, *Chem. Soc. Rev.*, 2016, **45**, 4873–4891.
75 N. Zion, A. Friedman, N. Levy and L. Elbaz, *Adv. Mater.*, 2018, **30**, 1800406.
76 W. Zhang, J. Chang and Y. Yang, *SusMat*, 2023, **3**, 2–20.
77 H.-L. Chou, B.-J. Hwang and C.-L. Sun, in *New and Future Developments in Catalysis*, ed. S. L. Suib, Elsevier, Amsterdam, 2013, pp. 217–270.
78 Y. Wang, J. Li and Z. Wei, *J. Mater. Chem. A*, 2018, **6**, 8194–8209.
79 S. D. Bhoyate, J. Kim, F. M. de Souza, J. Lin, E. Lee, A. Kumar and R. K. Gupta, *Coord. Chem. Rev.*, 2023, **474**, 214854.
80 D. B. Kumar, W. Nie, Z. Jiang, J. Lee and T. Maiyalagan, *J. Alloys Compd.*, 2023, **960**, 170828.
81 H. He, S. Liu, Y. Liu, L. Zhou, H. Wen, R. Shen, H. Zhang, X. Guo, J. Jiang and B. Li, *Green Chem.*, 2023, **25**, 9501–9542.
82 X. Zhang, S.-X. Guo, K. A. Gandionco, A. M. Bond and J. Zhang, *Mater. Today Adv.*, 2020, **7**, 100074.
83 Y. Hori, in *Modern Aspects of Electrochemistry*, ed. C. G. Vayenas, R. E. White and M. E. Gamboa-Aldeco, Springer, New York, NY, 2008, pp. 89–189.
84 J. Zhang, C. Guo, S. Fang, X. Zhao, L. Li, H. Jiang, Z. Liu, Z. Fan, W. Xu, J. Xiao and M. Zhong, *Nat. Commun.*, 2023, **14**, 1298.
85 I. M. Badawy, A. M. Ismail, G. E. Khedr, M. M. Taha and N. K. Allam, *Sci. Rep.*, 2022, **12**, 13456.
86 S. Banerjee, C. S. Gerke and V. S. Thoi, *Acc. Chem. Res.*, 2022, **55**, 504–515.
87 Z. Zhao and G. Lu, *Adv. Energy Mater.*, 2023, **13**, 2203138.
88 Q. Zhang, P. Li, D. Zhou, Z. Chang, Y. Kuang and X. Sun, *Small*, 2017, **13**, 1701648.
89 S. H. Ahn, I. Choi, H.-Y. Park, S. J. Hwang, S. J. Yoo, E. Cho, H.-J. Kim, D. Henkensmeier, S. W. Nam, S.-K. Kim and J. H. Jang, *Chem. Commun.*, 2013, **49**, 9323–9325.
90 Z. Lu, Y. Li, X. Lei, J. Liu and X. Sun, *Mater. Horiz.*, 2015, **2**, 294–298.
91 H. Huang, W. Huang, Z. Yang, J. Huang, J. Lin, W. Liu and Y. Liu, *J. Mater. Chem. A*, 2017, **5**, 1558–1566.
92 S. A. M. Mehryan, A. Tahmasebi, M. Izadi and M. Ghalambaz, *Int. J. Heat Mass Transfer*, 2020, **149**, 119184.
93 O. Lioubashevski, E. Katz and I. Willner, *J. Phys. Chem. B*, 2004, **108**, 5778–5784.
94 K. A. Sree Raj and C. S. Rout, *J. Mater. Chem. A*, 2023, **11**, 5495–5519.
95 R. E. D. L. Rue and C. W. Tobias, *J. Electrochem. Soc.*, 1959, **106**, 827.
96 H. Vogt, *Electrochim. Acta*, 1981, **26**, 1311–1317.
97 X. Fan, J. Xiao, W. Wang, Y. Zhang, S. Zhang and B. Tang, *Polymers*, 2018, **10**, 585.

98 C. L. Dennis and R. Ivkov, *Int. J. Hyperther.*, 2013, **29**, 715–729.
99 I. A. Leenson, *J. Chem. Educ.*, 1999, **76**, 1459.
100 Y. Duan, N. Dubouis, J. Huang, D. A. Dalla Corte, V. Pimenta, Z. J. Xu and A. Grimaud, *ACS Catal.*, 2020, **10**, 4160–4170.
101 J. Masa, C. Andronescu, H. Antoni, I. Sinev, S. Seisel, K. Elumeeva, S. Barwe, S. Marti-Sanchez, J. Arbiol, B. Roldan Cuenya, M. Muhler and W. Schuhmann, *ChemElectroChem*, 2019, **6**, 235–240.
102 T. P. Heins, N. Harms, L.-S. Schramm and U. Schröder, *Energy Technol.*, 2016, **4**, 1509–1513.
103 B. Pierozynski and T. Mikolajczyk, *Electrocatalysis*, 2015, **6**, 51–59.
104 M. Kallumadil, M. Tada, T. Nakagawa, M. Abe, P. Southern and Q. A. Pankhurst, *J. Magn. Magn. Mater.*, 2009, **321**, 3650–3651.
105 B. Kozissnik, A. C. Bohorquez, J. Dobson and C. Rinaldi, *Int. J. Hyperther.*, 2013, **29**, 706–714.
106 R. E. Rosensweig, *J. Magn. Magn. Mater.*, 2002, **252**, 370–374.
107 A. E. Deatsch and B. A. Evans, *J. Magn. Magn. Mater.*, 2014, **354**, 163–172.
108 J. Mohapatra, M. Xing and J. P. Liu, *Materials*, 2019, **12**, 3208.
109 L. Gloag, M. Mehdipour, D. Chen, R. D. Tilley and J. J. Gooding, *Adv. Mater.*, 2019, **31**, 1904385.
110 Q. A. Pankhurst, J. Connolly, S. K. Jones and J. Dobson, *J. Phys. D: Appl. Phys.*, 2003, **36**, R167.
111 N. Hasebe, *Int. J. Eng. Sci.*, 2011, **49**, 1019–1031.
112 J. Dodoo and A. A. Stokes, *Phys. Fluids*, 2020, **32**, 061703.
113 E. W. Lee, *Rep. Prog. Phys.*, 1955, **18**, 184.
114 A. J. Bard and L. R. Faulkner, *Electrochem. Commun.*, 2001, **2**, 580–632.
115 P. Dunne and J. M. D. Coey, *J. Phys. Chem. C*, 2019, **123**, 24181–24192.
116 K. Ray, S. P. Ananthavel, D. H. Waldeck and R. Naaman, *Science*, 1999, **283**, 814–816.
117 P. Haldar, S. Biswas, V. Sharma and A. Chandra, *J. Electrochem. Soc.*, 2018, **165**, A3230.
118 M. N. Baibich, J. M. Broto, A. Fert, F. N. Van Dau, F. Petroff, P. Etienne, G. Creuzet, A. Friederich and J. Chazelas, *Phys. Rev. Lett.*, 1988, **61**, 2472–2475.
119 W. Mtangi, V. Kiran, C. Fontanesi and R. Naaman, *J. Phys. Chem. Lett.*, 2015, **6**, 4916–4922.
120 W. Zhang, K. Banerjee-Ghosh, F. Tassinari and R. Naaman, *ACS Energy Lett.*, 2018, **3**, 2308–2313.
121 P. C. Mondal, W. Mtangi and C. Fontanesi, *Small Methods*, 2018, **2**, 1700313.
122 X. Ren, T. Wu, Y. Sun, Y. Li, G. Xian, X. Liu, C. Shen, J. Gracia, H.-J. Gao, H. Yang and Z. J. Xu, *Nat. Commun.*, 2021, **12**, 2608.
123 J. Li, J. Ma, Z. Ma, E. Zhao, K. Du, J. Guo and T. Ling, *Adv. Energy Sustainability Res.*, 2021, **2**, 2100034.
124 R. Sharpe, T. Lim, Y. Jiao, J. W. Niemantsverdriet and J. Gracia, *ChemCatChem*, 2016, **8**, 3762–3768.
125 T. Iida, H. Matsushima and Y. Fukunaka, *J. Electrochem. Soc.*, 2007, **154**, E112.
126 L. M. A. Monzon and J. M. D. Coey, *Electrochem. Commun.*, 2014, **42**, 42–45.
127 K. Tschulik, R. Sueptitz, M. Uhlemann, L. Schultz and A. Gebert, *Electrochim. Acta*, 2011, **56**, 5174–5177.
128 P. Dunne and J. M. D. Coey, *Phys. Rev. B: Condens. Matter Mater. Phys.*, 2012, **85**, 224411.
129 M. Wang, Z. Wang, Z. Guo and Z. Li, *Int. J. Hydrogen Energy*, 2011, **36**, 3305–3312.
130 R. S. Mulliken, *J. Chem. Phys.*, 1939, **7**, 20–34.
131 A. Ali, D. Najaf, A. Nazir, A. Haider, M. Iqbal, N. Alwadai, A. Kausar and A. Ahmad, *ACS Omega*, 2023, **8**, 9539–9546.
132 L. Yang, L. Jin, K. Wang, H. Xu, G. He and H. Chen, *Colloids Surf., A*, 2023, **672**, 131720.
133 C. S. Saraj, S. C. Singh, A. Shukla, W. Yu, M. U. Fayyaz and C. Guo, *ChemElectroChem*, 2021, **8**, 209–217.
134 X. Yu, J. Yu, Y. Fautrelle, A. Gagnoud, Z. Ren, X. Lu and X. Li, *J. Mater. Chem. A*, 2019, **7**, 19733–19744.
135 S. Hirt, F. Yuan, Y. Mozharivskyj and H. Hillebrecht, *Inorg. Chem.*, 2016, **55**, 9677–9684.
136 E. Warburg, *Annalen der Physik*, 1881, **249**, 141–164.
137 V. K. Pecharsky, K. A. Gschneidner, A. O. Pecharsky and A. M. Tishin, *Phys. Rev. B: Condens. Matter Mater. Phys.*, 2001, **64**, 144406.
138 P. Lekkla, P. Jantaratana and T. Chotibhawaris, *Metals*, 2022, **12**, 2137.
139 G. Xiong, Y. Chen, Z. Zhou, F. Liu, X. Liu, L. Yang, Q. Liu, Y. Sang, H. Liu, X. Zhang, J. Jia and W. Zhou, *Adv. Funct. Mater.*, 2021, **31**, 2009580.
140 B. Lu, Q. Liu, C. Wang, Z. Masood, D. J. Morris, F. Nichols, R. Mercado, P. Zhang, Q. Ge, H. L. Xin and S. Chen, *Research*, 2022, 9756983.
141 Q. Liu, S. McNair, F. Nichols, B. Lu, B. Yu, D. Pan, J. Ko, A. Bhuller, F. Bridges and S. Chen, *Adv. Sens. Energy Mater.*, 2023, **2**, 100046.
142 Q. Liu, B. Lu, F. Nichols, J. Ko, R. Mercado, F. Bridges and S. Chen, *SusMat*, 2022, **2**, 335–346.
143 Z.-Y. Yu, C.-C. Lang, M.-R. Gao, Y. Chen, Q.-Q. Fu, Y. Duan and S.-H. Yu, *Energy Environ. Sci.*, 2018, **11**, 1890–1897.
144 G. Xiong, J. Jia, L. Zhao, X. Liu, X. Zhang, H. Liu and W. Zhou, *Sci. Bull.*, 2021, **66**, 386–406.
145 Q. Liu, F. Nichols, A. Bhuller, K. Singewald, H.-L. Kuo, J. Q. Lu, G. L. Millhauser, F. Bridges, Q. Ge and S. Chen, *Appl. Catal., B*, 2024, **342**, 123399.
146 N. K, K. Pramoda, K. S. Sharath Kumar, S. Radhakrishnan and C. Sekhar Rout, *Energy Adv.*, 2023, **2**, 1724–1734.
147 P. Shinde, C. S. Rout, D. Late, P. K. Tyagi and M. K. Singh, *Int. J. Hydrogen Energy*, 2021, **46**, 2617–2629.
148 A. Patra and C. S. Rout, *J. Energy Storage*, 2023, **5**, e411.
149 H. Sun, Z. Yan, F. Liu, W. Xu, F. Cheng and J. Chen, *Adv. Mater.*, 2020, **32**, 1806326.
150 X.-Y. Zhang, W.-L. Yu, J. Zhao, B. Dong, C.-G. Liu and Y.-M. Chai, *Appl. Mater. Today*, 2021, **22**, 100913.
151 A. Bund, S. Koehler, H. H. Kuehnlein and W. Plieth, *Electrochim. Acta*, 2003, **49**, 147–152.

152 Y. Zhang, B. Yuan, L. Li and C. Wang, *J. Electroanal. Chem.*, 2020, **865**, 114143.
153 M. Najminoori, A. Mohebbi, K. Afrooz and B. G. Arabi, *Chem. Eng. Sci.*, 2019, **199**, 1–19.
154 P. Żabiński, K. Mech and R. Kowalik, *Electrochim. Acta*, 2013, **104**, 542–548.
155 B. He, Y. Kuang, Z. Hou, M. Zhou and X. Chen, *J. Mater. Res.*, 2018, **33**, 213–224.
156 D. Likius, A. Rahman, C. Zivayi and V. Uahengo, *Catal. Lett.*, 2020, **150**, 1942–1956.
157 Y. Chen, J. Zhang, J. Sort, E. Pellicer and R. Guan, *Int. J. Hydrogen Energy*, 2024, **59**, 625–634.
158 S. Elsharkawy, D. Kutyła and P. Zabinski, *Coatings*, 2023, **13**, 1816.
159 Z. Wang, S. Yuan, H. Tian, T. Zang, J. Li, J. Liu, G. Li, J. Wang, T. Liu and Q. Wang, *Appl. Catal., B*, 2024, **343**, 123579.
160 W. Jiang, F. Zhu, Y. Chen, J. Li, W. Cheng and J. Liu, *J. Alloys Compd.*, 2023, **962**, 171120.
161 F. Zhu and X. Wen, *Appl. Surf. Sci.*, 2024, **649**, 159133.
162 Z. Li, Z. Lv, X. Liu, G. Wang, Y. Lin, G. Xie and L. Jiang, *Renew. Energy*, 2021, **165**, 612–618.
163 A. Sheelam and J. G. Bell, *Int. J. Hydrogen Energy*, 2024, **56**, 348–357.
164 C. Ma, W. Yu, M. Jiang, W. Cui and F. Xia, *Ceram. Int.*, 2018, **44**, 5163–5170.
165 W. Jiang, J. Li, C. Zhao, W. Cheng, J. Liu and Y. Chen, *Int. J. Hydrogen Energy*, 2024, **51**, 1486–1496.
166 W. Jiang, H. Li, Y. Chen, Y. Wu, J. Li, X. Wang, X. Huang and Y. Lao, *Int. J. Hydrogen Energy*, 2023, **48**, 4287–4299.
167 S. Chu and A. Majumdar, *Nature*, 2012, **488**, 294–303.
168 B. Zhang, J. Yao, J. Liu, T. Zhang, H. Wan and H. Wang, *EES Catal.*, 2023, **1**, 1017–1024.
169 Y. Deng, S. Xiao, Y. Zheng, X. Rong, M. Bai, Y. Tang, T. Ma, C. Cheng and C. Zhao, *Chem. Eng. J.*, 2023, **451**, 138514.
170 R. Hu, L. Jiao, H. Liang, Z. Feng, B. Gao, X.-F. Wang, X.-Z. Song, L.-Z. Liu and Z. Tan, *Small*, 2023, **19**, 2304132.
171 X. Mao, Z. Qin, S. Ge, C. Rong, B. Zhang and F. Xuan, *Mater. Horiz.*, 2023, **10**, 340–360.
172 Z.-Q. Hou, R.-W. Liu, X.-N. Feng, X.-L. Jia and K.-J. Huang, *Fuel*, 2024, **357**, 130054.
173 X. Xu, X. Liu, W. Zhong, G. Liu, L. Zhang and Y. Du, *Ceram. Int.*, 2023, **49**, 16836–16841.
174 W. Zhou, M. Chen, M. Guo, A. Hong, T. Yu, X. Luo, C. Yuan, W. Lei and S. Wang, *Nano Lett.*, 2020, **20**, 2923–2930.
175 J. Chen, Y. Ling, D. Qu, L. Huang, J. Li, P. Tang, A. He, X. Jin, Y. Zhou, M. Xu, J. Du, Z. Han and Q. Xu, *J. Alloys Compd.*, 2021, **877**, 160271.
176 G. Li, Q. Yang, K. Manna, Q. Mu, C. Fu, Y. Sun and C. Felser, *CCS Chem.*, 2021, **3**, 2259–2267.
177 L. Elias and A. Chitharanjan Hegde, *Electrocatalysis*, 2017, **8**, 375–382.
178 L. Zhu, P. Yang, Y. Huan, F. Zhou and Y. Zhang, *Adv. Energy Sustainability Res.*, 2021, **2**, 2100089.
179 F. Zeng, W.-B. Zhang and B.-Y. Tang, *Chinese Phys. B*, 2015, **24**, 097103.
180 W. Zeng, Z. Jiang, X. Gong, C. Hu, X. Luo, W. Lei and C. Yuan, *Small*, 2023, **19**, 2206155.
181 M. Su, W. Zhou, L. Liu, M. Chen, Z. Jiang, X. Luo, Y. Yang, T. Yu, W. Lei and C. Yuan, *Adv. Funct. Mater.*, 2022, **32**, 2111067.
182 Y. Yu, S.-Y. Huang, Y. Li, S. N. Steinmann, W. Yang and L. Cao, *Nano Lett.*, 2014, **14**, 553–558.
183 J. Huang, W. Zhou, X. Luo, Y. Ding, D. Peng, M. Chen, H. Zhou, C. Hu, C. Yuan and S. Wang, *Chem. Eng. J.*, 2023, **454**, 140279.
184 L. Cai, J. Huo, P. Zou, G. Li, J. Liu, W. Xu, M. Gao, S. Zhang and J.-Q. Wang, *ACS Appl. Mater. Interfaces*, 2022, **14**, 15243–15249.
185 M. M. Can, C. Bairam, S. Aksoy, D. S. Kuruca, S. Kaneko, Z. Aktaş and M. O. Öncül, *Coatings*, 2022, **12**, 481.
186 C. Niether, S. Faure, A. Bordet, J. Deseure, M. Chatenet, J. Carrey, B. Chaudret and A. Rouet, *Nat. Energy*, 2018, **3**, 476–483.
187 W. T. Hong, M. Risch, K. A. Stoerzinger, A. Grimaud, J. Suntivich and Y. Shao-Horn, *Energy Environ. Sci.*, 2015, **8**, 1404–1427.
188 J. Song, C. Wei, Z.-F. Huang, C. Liu, L. Zeng, X. Wang and Z. J. Xu, *Chem. Soc. Rev.*, 2020, **49**, 2196–2214.
189 P. Liu, B. Chen, C. Liang, W. Yao, Y. Cui, S. Hu, P. Zou, H. Zhang, H. J. Fan and C. Yang, *Adv. Mater.*, 2021, **33**, 2007377.
190 B. You, M. T. Tang, C. Tsai, F. Abild-Pedersen, X. Zheng and H. Li, *Adv. Mater.*, 2019, **31**, 1807001.
191 D. Liu, Y. Yan, H. Li, D. Liu, Y. Yang, T. Li, Y. Du, S. Yan, T. Yu, W. Zhou, P. Cui and Z. Zou, *Adv. Mater.*, 2023, **35**, 2203420.
192 J. Deng, H. Qiao, C. Li, Z. Huang, S. Luo and X. Qi, *Appl. Surf. Sci.*, 2023, **637**, 157899.
193 T. Wang, H. He, Z. Meng, S. Li, M. Xu, X. Liu, Y. Zhang, M. Liu and M. Feng, *ChemPhysChem*, 2023, **24**, e202200845.
194 P. K. Sharma, M. Pramanik, M. V. Limaye and S. B. Singh, *J. Phys. Chem. C*, 2023, **127**, 16259–16266.
195 Z. Sun, L. Lin, J. He, D. Ding, T. Wang, J. Li, M. Li, Y. Liu, Y. Li, M. Yuan, B. Huang, H. Li and G. Sun, *J. Am. Chem. Soc.*, 2022, **144**, 8204–8213.
196 X. Lyu, Y. Zhang, Z. Du, H. Chen, S. Li, A. I. Rykov, C. Cheng, W. Zhang, L. Chang, W. Kai, J. Wang, L. Zhang, Q. Wang, C. Huang and E. Kan, *Small*, 2022, **18**, 2204143.
197 Y. Li, L. Zhang, J. Peng, W. Zhang and K. Peng, *J. Power Sources*, 2019, **433**, 226704.
198 X. Qin, J. Teng, W. Guo, L. Wang, S. Xiao, Q. Xu, Y. Min and J. Fan, *Catal. Lett.*, 2023, **153**, 673–681.
199 M. Chen, W. Zhou, K. Ye, C. Yuan, M. Zhu, H. Yu, H. Yang, H. Huang, Y. Wu, J. Zhang, X. Zheng, J. Shen, X. Wang and S. Wang, *Small*, 2023, **19**, 2300122.
200 Y. Zhang, P. Guo, S. Li, J. Sun, W. Wang, B. Song, X. Yang, X. Wang, Z. Jiang, G. Wu and P. Xu, *J. Mater. Chem. A*, 2022, **10**, 1760–1767.
201 H. Liu, Y. Ren, K. Wang, X. Mu, S. Song, J. Guo, X. Yang and Z. Lu, *Metals*, 2022, **12**, 800.

202 D. Peng, C. Hu, X. Luo, J. Huang, Y. Ding, W. Zhou, H. Zhou, Y. Yang, T. Yu, W. Lei and C. Yuan, *Small*, 2023, **19**, 2205665.
203 Y. Ding, W. Zhou, X. Luo, J. Huang, D. Peng, M. Chen, H. Zhou, C. Hu and C. Yuan, *Appl. Phys. Lett.*, 2022, **121**, 093901.
204 H. Chen, H. Zheng, T. Yang, S. Yue, P. Gao, X. Liu and H. Xiao, *Int. J. Hydrogen Energy*, 2022, **47**, 18675–18687.
205 H. Zheng, Y. Wang, P. Zhang, F. Ma, P. Gao, W. Guo, H. Qin, X. Liu and H. Xiao, *Chem. Eng. J.*, 2021, **426**, 130785.
206 X. Gong, Z. Jiang, W. Zeng, C. Hu, X. Luo, W. Lei and C. Yuan, *Nano Lett.*, 2022, **22**, 9411–9417.
207 D. R. Weinberg, C. J. Gagliardi, J. F. Hull, C. F. Murphy, C. A. Kent, B. C. Westlake, A. Paul, D. H. Ess, D. G. McCafferty and T. J. Meyer, *Chem. Rev.*, 2012, **112**, 4016–4093.
208 I. Siewert, *Chem.–Eur. J.*, 2015, **21**, 15078–15091.
209 R. M. Bullock, J. G. Chen, L. Gagliardi, P. J. Chirik, O. K. Farha, C. H. Hendon, C. W. Jones, J. A. Keith, J. Klosin, S. D. Minteer, R. H. Morris, A. T. Radosevich, T. B. Rauchfuss, N. A. Strotman, A. Vojvodic, T. R. Ward, J. Y. Yang and Y. Surendranath, *Science*, 2020, **369**, eabc3183.
210 S. Sahu and D. P. Goldberg, *J. Am. Chem. Soc.*, 2016, **138**, 11410–11428.
211 E. J. Askins, M. R. Zoric, M. Li, Z. Luo, K. Amine and K. D. Glusac, *Nat. Commun.*, 2021, **12**, 3288.
212 G. Chen, Y. Sun, R. R. Chen, C. Biz, A. C. Fisher, M. P. Sherburne, J. W. Ager III, J. Gracia and Z. J. Xu, *J. Phys. Energy*, 2021, **3**, 031004.
213 W. Kiciński, M. Artyfikiewicz, K. Miecznikowski, M. Donten, S. Dyjak, M. Gratzke, J. Nawała and A. M. Nowicka, *J. Alloys Compd.*, 2023, **935**, 168051.
214 L. T. Tufa, K.-J. Jeong, V. T. Tran and J. Lee, *ACS Appl. Mater. Interfaces*, 2020, **12**, 6598–6606.
215 G. Brisard, N. Bertrand, P. N. Ross and N. M. Marković, *J. Electroanal. Chem.*, 2000, **480**, 219–224.
216 W. Kiciński, J. P. Sęk, E. Matysiak-Brynda, K. Miecznikowski, M. Donten, B. Budner and A. M. Nowicka, *Appl. Catal., B*, 2019, **258**, 117955.
217 J. Yan, Y. Wang, Y. Zhang, S. Xia, J. Yu and B. Ding, *Adv. Mater.*, 2021, **33**, 2007525.
218 Z. Zeng, T. Zhang, Y. Liu, W. Zhang, Z. Yin, Z. Ji and J. Wei, *ChemSusChem*, 2018, **11**, 580–588.
219 Y. Yang, G. Han, M. Xie, G. V. D. O. Silva, G.-X. Miao, Y. Huang and J. Fu, *Small Methods*, 2024, 2301594.
220 B. Silvi and A. Savin, *Nature*, 1994, **371**, 683–686.
221 C. W. Lee, N. H. Cho, S. W. Im, M. S. Jee, Y. J. Hwang, B. K. Min and K. T. Nam, *J. Mater. Chem. A*, 2018, **6**, 14043–14057.
222 P. J. Hore and H. Mouritsen, *Annu. Rev. Biophys.*, 2016, **45**, 299–344.
223 H. Pan, X. Jiang, X. Wang, Q. Wang, M. Wang and Y. Shen, *J. Phys. Chem. Lett.*, 2020, **11**, 48–53.
224 P. Wang, Y. Qu, X. Meng, J. Tu, W. Zheng, L. Hu and Q. Chen, *Magnetochemistry*, 2023, **9**, 65.
225 R. Gao, M. S. Kodaimati, K. M. Handy, S. E. Root and G. M. Whitesides, *J. Phys. Chem. C*, 2022, **126**, 18159–18169.
226 M. Zhu, Y. Wang, Y. Wu, J. Liu, J. Zhang, H. Huang, X. Zheng, J. Shen, R. Zhao, W. Zhou and S. Wang, *Energy Environ. Mater.*, 2023, **6**, e12403.

